RESEARCH

2008-10

Pavement Evaluation Using Ground Penetrating Radar

Technical Report Documentation Page

1. Report No.	2.	3. Recipients Accession No.
MN/RC 2008-10		

4. Title and Subtitle	5. Report Date
Pavement Evaluation using Ground Penetrating Radar	March 2008
	6.

7. Author(s)	8. Performing Organization Report No.
Yuejian Cao, Bojan B. Guzina , Joseph F. Labuz	

9. Performing Organization Name and Address	10. Project/Task/Work Unit No.
Department of Civil Engineering University of Minnesota 500 Pillsbury Dr. SE Minneapolis, Minnesota 55455	11. Contract (C) or Grant (G) No. (c) 81655 (wo) 131

12. Sponsoring Organization Name and Address	13. Type of Report and Period Covered
Minnesota Department of Transportation 395 John Ireland Boulevard Mail Stop 330 St. Paul, Minnesota 55155	Final Report 14. Sponsoring Agency Code

15. Supplementary Notes
http://www.lrrb.org/PDF/200810.pdf

16. Abstract (Limit: 200 words)

The objective of this project was to develop an efficient and accurate algorithm for the back analysis of pavement conditions measured by ground penetrating radar (GPR). In particular, more reliable information about the thickness of the asphalt concrete (AC) layer and the dielectric constants of the AC and base layers were obtained from the electromagnetic field measurements performed on roads using GPR.

A brief introduction to the existing methodology for interpreting GPR images is reviewed, and the theory associated with electromagnetic wave propagation in layered structures is described. Utilizing the full waveform solution, algorithms for back analysis of pavement conditions were developed based on the artificial neural network approach and the frequency response function concept. Software called "GopherGPR" uses the GPR signal from one antenna to interpret the characteristics of the AC layer with no assumptions on material properties. Thus, the new technique has the capability of providing information not previously available.

17. Document Analysis/Descriptors	18. Availability Statement
GPR thickness dielectric constant evaluation	No restrictions. Document available from: National Technical Information Services, Springfield, Virginia 22161

19. Security Class (this report)	20. Security Class (this page)	21. No. of Pages	22. Price
Unclassified	Unclassified	102	

PAVEMENT EVALUATION USING GROUND PENETRATING RADAR

Final Report

Prepared by
Yuejian Cao, Bojan Guzina, and Joseph Labuz
Department of Civil Engineering
University of Minnesota

March 2008

Prepared for
Minnesota Department of Transportation
Office of Materials and Road Research
1400 Gervais Avenue
Maplewood, MN 55109

Acknowledgement

Partial support was provided by the Minnesota Department of Transportation. Special thanks are extended to the Technical Advisory Panel, especially Dr. Shongtao Dai and Mr. Matthew Lebens, for sharing their expertise and knowledge of ground penetrating radar. Geophysical Survey Systems supplied some necessary information on data acquisition. This report represents the results of research conducted by the authors and does not necessarily represent the views or policies of the Minnesota Department of Transportation and/or the Center for Transportation Studies.

Contents

List of Tables

List of Figures

Executive Summary

The objective of this project was to develop an efficient and accurate algorithm for the back analysis of pavement conditions measured by ground penetrating radar (GPR). In particular, more reliable information about the thickness of the asphalt concrete (AC) layer and the dielectric constants of the AC and base layers were obtained from the electromagnetic field measurements performed on roads using GPR.

A brief introduction to the existing methodology for interpreting GPR images is reviewed, and the theory associated with electromagnetic wave propagation in layered structures is described. Utilizing the full waveform solution, algorithms for back analysis of pavement conditions were developed based on the artificial neural network approach and the frequency response function concept. Software called "GopherGPR" uses the GPR signal from one antenna to interpret the characteristics of the AC layer with no assumptions on material properties. Thus, the new technique has the capability of providing information not previously available.

Chapter 1

Introduction

Among the rapidly growing number of field techniques and devices employed to evaluate the near-surface and subsurface conditions of transportation facilities, the ground penetrating radar (GPR) is a technique of mounting popularity in pavement engineering owing to its superior rate (i.e. speed) of field coverage. The majority of GPR applications resolves around the estimation of layer thickness using the travel-time technique, where the layer thickness is presented by the time marker in the received signal as shown in Fig.1.1. Because

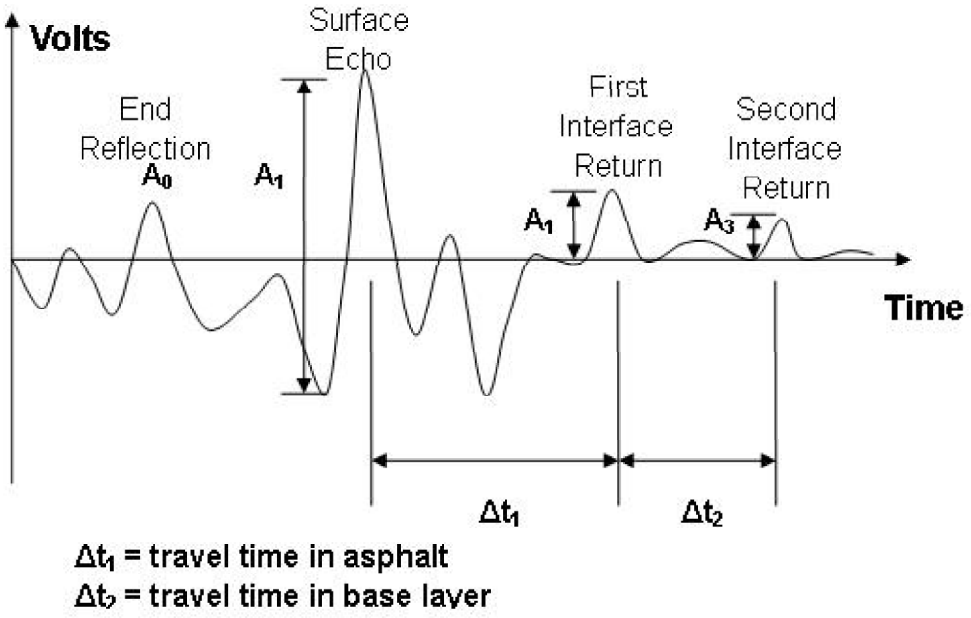

Figure 1.1: GPR waveform in time history

the pulse travels back and forth inside the layer, the thicknesses are computed as

$$h_{\text{Asphalt}} = v_A \, \frac{\Delta t_1}{2}, \quad h_{\text{Base}} = v_B \, \frac{\Delta t_2}{2}. \tag{1.1}$$

where the electromagnetic wave velocities v_A (in the asphalt layer) and v_B (in the base layer) are related to the dielectric constants ε_A and ε_B in each layer by,

$$v_A = \frac{c}{\sqrt{\varepsilon_A}}, \quad v_B = \frac{c}{\sqrt{\varepsilon_B}} \tag{1.2}$$

where c as the speed of light in vacuum.

In the travel-time technique, the dielectric constant (ε) and travel time (Δt) are the only information pertinent in determining the layer thickness, which is easy to implement. There are, however, quite a few instances of having difficulties to obtain these parameters. For example, it is possible that the in-situ dielectric constant values are unknown when doing the survey. If the value of dielectric constant is taken from empirical knowledge, it will most likely degrade the accuracy of the estimated layer thickness. In addition, each peak in the temporal GPR record represents a pulse reflected back from the layer interface. During the field survey, the peak may be overwhelmed by the ambient noise, thus multiplying the difficulty of identifying the travel time between interfaces. As a consequence of the above two sources of error, layer thickness computed in equation (1.1) cannot represent the true layer structure. In estimation of the layer thickness, the state of art of GPR travel-time technique has an error around $\pm 7.5\%$ compared to coring.

The objective of this project was to demonstrate the capabilities and limitations of ground penetrating radar (GPR) for use in local road applications. The effectiveness of a GPR survey is a function of site conditions, the equipment used, and experience of personnel interpreting the results. In addition, not all site conditions are appropriate for GPR applications. GPR is a nondestructive field test that can provide a continuous profile of existing road conditions. GPR utilizes high-speed data collection at speeds up to 50 mph, thus requiring less traffic control and resulting in greater safety. GPR has the potential to be used for a variety of pavement applications, including measuring the thickness of asphalt pavement, base and sub-grade; assisting in the analysis of rutting mechanisms; calculating and verifying material properties; locating subsurface objects; detecting stripping and/or layer separation; detecting subsurface moisture; and determining depth to near-surface bedrock and peat deposits.

In order to improve the performance of GPR survey, a new technique stems from the full electromagnetic waveform analysis layered system has been developed. The detail of the EM model is reported in Chapter 4. The success of this layered EM wave model lies in its ability to reproduce the entire GPR scan (i.e., the waveform) including information about time and amplitude. These waveforms, which contain the information about the layer thickness and dielectric constant, are individually different. In other words, the waveform is labeled by its pattern called the frequency response function (FRF). With the aid of an artificial neural network (ANN) algorithm, it is further allowed to identify the connections between the pattern and the parameters of the waveform, as will be illustrated in Chapter 5. The neural network has to be trained to establish a meaningful representation of the profile and the GPR data. Once the neural network has been trained, the corresponding layer properties can be obtained by inputting the FRF of the GPR response to the network. The implementation procedure is reported in Chapter 6.

Chapter 2

Background Information

The examples of GPR application include the determination of layer thickness, voids detection and moisture content measurement. The main adventures toward the interpretation of GPR measurements, as is usually done in the context of GPR surveys, is the conventional travel-time analysis. This method is easy from the practical standpoint and has been widely used but the limitation is also obvious, as will be discussed more in this chapter. To compare, the full electromagnetic waveform analysis, as another promising approach, will be briefly introduced as well.

2.1 GPR applications

Layer thickness

Since the introduction of the GPR to pavement engineering, its most successful application is to determine the pavement layer thickness. By "picking" the first peak of the reflected electromagnetic wave, the thickness is determined by the layer dielectric constant ε and travel time t in nanoseconds.

$$h[\text{in.}] = \frac{11.8 \times \text{t}}{\sqrt{\varepsilon}} \tag{2.1}$$

It is worth noting that the recorded travel time should be divided by two to represent a round trip, up and down. The dielectric constant, however, depends on the in-situ conditions. Obtaining cores for calibration could lead to a reduced error in estimation of layer thickness. However, it is apparently only applicable to a few spots due to the variation of the dielectric along the road.

In practice, one may use the amplitudes of the reflected pulses to estimate the in-situ dielectric constant. Given that the dielectric constant in air is equal to 1, the subsurface layer dielectric constant can be calculated from

$$\sqrt{\varepsilon_1} = \frac{A_m + A_0}{A_m - A_0} \tag{2.2}$$

where A_0 and A_m are the reflected amplitude from the top of surface layer and the metal plate, respectively. The dielectric constant of the subsequent layer is calculated from

$$\sqrt{\varepsilon_1} = \sqrt{\varepsilon_1}\frac{1-\left(\frac{A_0}{A_m}\right)^2+\frac{A_1}{A_m}}{1-\left(\frac{A_0}{A_m}\right)^2-\frac{A_1}{A_m}} \tag{2.3}$$

where A_1 is the reflected amplitude from the top of subsequent layer. Moreover, a similar formula can be recursively obtained for the nth layer (Al-Qadi, 2004).

$$\sqrt{\varepsilon_n} = \sqrt{\varepsilon_{n-1}}\frac{1-\left(\frac{A_0}{A_m}\right)^2+\sum_{i=1}^{n-2}\gamma_i\frac{A_i}{A_m}+\frac{A_{n-1}}{A_m}}{1-\left(\frac{A_0}{A_m}\right)^2+\sum_{i=1}^{n-2}\gamma_i\frac{A_i}{A_m}-\frac{A_{n-1}}{A_m}} \tag{2.4}$$

where A_i is the reflected amplitude from the top of ith layer, and γ_i is the reflection coefficient between the ith and $i+1$th layers, i.e.

$$\gamma_i = \frac{\sqrt{\varepsilon_i}-\sqrt{\varepsilon_{i+1}}}{\sqrt{\varepsilon_i}+\sqrt{\varepsilon_{i+1}}}. \tag{2.5}$$

Since this technique relies greatly on the surface reflection, and because of the different compositions and ages of the layers in older pavements, the computed dielectric constant may not be accurate. The error of thickness based on this dielectric constant estimation is around ± 5 to $\pm 7.5\%$ for asphalt layer thickness, and $\pm 9.5\%$ for base layer thickness (David, 2006). However, it was found in study that the dielectric constant decreases linearly with aging but remains within the typical limits (Al-Qadi, 2004).

Another approach to estimate the dielectric constant is based on the common depth point technique. Two sets of antenna were used simultaneously to estimate the average layer dielectric constant based on the collection of the response over the same location. The error of thickness based on this dielectric constant estimation is around 6.8% compared to coring (Lahouar, 2002).

Water content

Since water has much higher value of dielectric constant than that of asphalt, investigations have been done to track the relationship between the moisture content and dielectric constant. Topp et al. (1980) used a third-order polynomial to describe the relation between the effective dielectric constant and the volumetric water content (VWC), where

$$\varepsilon_{eff} = 3.03 + 9.3\text{VWC} + 146.0\text{VWC}^2 - 76.7\text{VWC}^3. \tag{2.6}$$

Conversely, the measurement of ε_{eff} can be used to determine VWC by a third polynomial equation.

$$\text{VWC} = -5.3 \times 10^{-2} + 2.92 \times 10^{-2}\varepsilon_{\text{eff}} - 5.5 \times 10^{-4}\varepsilon_{\text{eff}}^2 + 4.3 \times 10^{-6}\varepsilon_{\text{eff}}^3 \tag{2.7}$$

More specific models can be found from the mixture theory, where the effective dielectric constant of a pavement layer is a function of the dielectric constants of its constituents. The simplest mixture theory is the complex refractive index model, as described in Maser and Scullion (1992). If asphalt layer is assumed to composed of air voids, aggregate, asphalt binder, and water, its bulk (i.e. effective) dielectric constant is given by

$$\sqrt{\varepsilon_{eff}} = V_{air}\sqrt{\varepsilon_{air}} + V_{agg}\sqrt{\varepsilon_{agg}} + V_{binder}\sqrt{\varepsilon_{binder}} + V_{water}\sqrt{\varepsilon_{water}}. \tag{2.8}$$

Another simple model suggested by Herkelrath et al. (1991) uses the following equation

$$\text{VWC} = a\sqrt{\varepsilon_{eff}} + b, \tag{2.9}$$

where $a > 0$.

These models suggest a monotonically increasing relationship between the effective dielectric constant and moisture content of the mixture. It was found, however, that surface water on the pavement hardly affects the GPR data, unless the pavement structure is full saturated (David, 2006).

Density

Another material parameter affecting the dielectric constant is the mass density. The dielectric constant increases with increasing value of the layer density. Therefore this relation can be utilized to detect stripping and air void content in pavement systems.

Stripping happens where the asphalt and aggregate bond fails, which leaves a weak layer. After continuously overlaying above such stripped layers that have lower density, surface crack often reappears within a short period of time. Since stripping indicates a layer with low density, a negative reflection will be generated from the interface between layers. The GPR was reported to be successful in detecting the location and extent of subsurface stripping at moderate or advanced stage (Scullion et al. 1996), although the presented approach is approximate and could potentially be improved via the full waveform analysis.

Measuring air voids content using its dielectric constant is based on the fact that void ratio affects the overall density of the layer. Suitable empirical correlations can be obtained to monitor the quality of new HMA surfacing (Saarenketo and Roimela, 1998).

2.2 GPR waveform analysis

Integral representation

The waveform analysis approach offers the potential of better accuracy but requires a deeper knowledge of electromagnetic wave propagation. Since the entire electromagnetic response is available for backcalculation, this approach certainly has access to more information, which permits a better interpretation. To find the solution in layered structure, the key is to use the so called method of moments (MOM), where the response of the pavement system "illuminated" by electromagnetic waves is expressed in terms of integral representations. There are in general two alternative formulations: the electric field integral equation (EFIE) (Yu,2006), defined as

$$\begin{aligned} \mathbf{E}(\mathbf{r}) &= \int_V \bar{G}_E(\mathbf{r},\mathbf{r}')\mathbf{J}(\mathbf{r}')d\mathbf{r}' \\ \mathbf{H}(\mathbf{r}) &= \int_V \bar{G}_H(\mathbf{r},\mathbf{r}')\mathbf{J}(\mathbf{r}')d\mathbf{r}' \end{aligned} \tag{2.10}$$

where $\bar{G}_H$ and $\bar{G}_E$ are dyadic Green's functions for the electric field of the medium. They are related to each other via

$$\bar{G}_H(\mathbf{r},\mathbf{r}') = -\frac{1}{i\omega\mu}\nabla\times\bar{G}_E(\mathbf{r},\mathbf{r}') \tag{2.11}$$

More precisely, the dyadic Green's function $\bar{G}_E$ is defined by the scalar Green's function $g(\mathbf{r}'-\mathbf{r})$ of the medium.

$$\bar{G}_E(\mathbf{r}',\mathbf{r}) = i\omega\mu\left[\bar{\mathbf{I}} + \frac{\nabla\nabla}{k^2}\right]g(\mathbf{r}-\mathbf{r}') \tag{2.12}$$

where for an unbounded medium

$$g(\mathbf{r}-\mathbf{r}') = \frac{e^{ik|\mathbf{r}-\mathbf{r}'|}}{4\pi|\mathbf{r}-\mathbf{r}'|}, \tag{2.13}$$

and the mixed potential integral equation (MPIE) (Yu,2006), defined as

$$\begin{aligned} \mathbf{E}(\mathbf{r}) &= -i\omega\mathbf{A}(\mathbf{r}) - \nabla\phi(\mathbf{r}) \qquad \mathbf{A}(\mathbf{r}) = \int_V \bar{G}_A(\mathbf{r},\mathbf{r}')\mathbf{J}(\mathbf{r}')d\mathbf{r}' \\ \mathbf{H}(\mathbf{r}) &= \frac{1}{\mu}\nabla\times\mathbf{A}(\mathbf{r}) \qquad\qquad \phi(\mathbf{r}) = \int_V G_V(\mathbf{r},\mathbf{r}')\rho(\mathbf{r}')d\mathbf{r}' \end{aligned} \tag{2.14}$$

where $\mathbf{A}(\mathbf{r})$ is the magnetic vector potential due to the current density $\mathbf{J}(\mathbf{r})$, $\phi(\mathbf{r})$ is the corresponding scalar potential related to $\mathbf{A}(\mathbf{r})$ through the Lorenz gauge condition, $\bar{G}_A$ is the dyadic green's function represents the magnetic vector potential due to current dipole, and G_V is the scalar green's function represents the scalar potential due to point charge.

$$\bar{G}_A = (\hat{x}G_A^{xx} + \hat{z}G_A^{zx})\hat{x} + (\hat{y}G_A^{yy} + \hat{z}G_A^{zy})\hat{y} + \hat{z}G_A^{zz}\hat{z} \tag{2.15}$$

where G_A^{ij} is the green's function in i direction due to current dipole in j direction, in matrix form

$$\bar{G}_A = \begin{bmatrix} G_A^{xx} & 0 & 0 \\ 0 & G_A^{yy} & 0 \\ G_A^{zx} & G_A^{zy} & G_A^{zz} \end{bmatrix} \tag{2.16}$$

The advantage of EFIE is that it makes it possible to solve problem of multiple buried dielectric and conducting objects. In addition, it allows one to compute the scattered filed and induced currents on the conducting surface. The downside of this method, however, is that $\bar{G}_E$ and $\bar{G}_H$ have higher-order singularities compared $\bar{G}_A$ and G_V in MPIE which have lower-order singularities and faster convergence. However, MPIE can handle only perfectly conducting objects and only gives the induced currents on the conducting surfaces (Cui, 1999). Moreover, since the scalar potential kernel G_V in MPIE has different form for horizontal and vertical current components, it is not easy to extend the solution to general nonplanar conductors (Michalski, 1997).

A combination of the above two methods is called the combined-field integral equation (CFIE), defined as

$$\text{CFIE } = \alpha\text{EFIE } + (1-\alpha)\text{MFIE} \tag{2.17}$$

The improvement can be seen as it generally results in better-conditioned matrix equation and no internal resonance. Unfortunately, this method is not applicable for solely open surface problems when compared to EFIE (Ergül, 2005).

Evaluation of the Green's function

In the context of the above formulations, the major problem is how to efficiently evaluate the Green's functions in the integrals of (2.10) and (2.14). Several methods have been investigated so far and will be illustrated below.

When the source and receiver are in the same layer and frequency belongs to some limited range, one way to evaluate the green's function is the complex image method (CIM). It basically expands the kernel via a series of complex exponentials as

$$\bar{G} \simeq \sum_{m=1}^{N} a_m e^{-b_m k_{z_i}}. \tag{2.18}$$

Then the Sommerfeld identity is applied to obtain the closed-form solution in the form of

$$G \simeq \sum_{m=1}^{N} a_m \frac{e^{-ik_i r_m}}{r_m} + \text{direct term} + \text{surface waves}. \tag{2.19}$$

The above expansion, however, becomes difficult to compute when the frequency is high or the medium is multilayered as it is the case in pavement systems.

To expedite the integral evaluation, one can revise the integral path to such as steepest decent path (SDP) and revised original path (ROP) (Cui,1999). Note that the SDP is efficient, but only valid in simple structures.

Recently, a new algorithm called fast interpolation and filtering algorithm (FIFA) (Yu, 2006) is introduced. It is fast algorithm since it introduces a window function to force a faster decay of the integrand. However, this very window function introduces an error which results in low accuracy when the source is close to receiver.

Compared to the above developments, a better way to evaluate the Green's function is based on the method of asymptotic decomposition (Pak & Guzina, 2002), where the Green's function in the transformed domain is decomposed into the asymptotic term and the residual term. The asymptotic term is evaluated in a closed-form via analytical functions while the residual term is evaluated numerically. The advantage of this decomposition is that since the integration path is from 0 to infinity, the singularity of the total kernel at infinity is captured by the asymptotic term as shown in Figure 2.1.

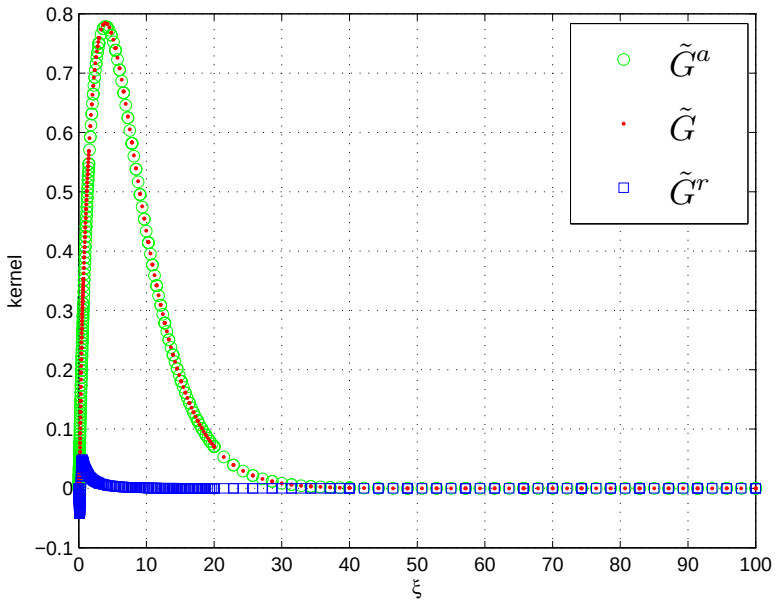

Figure 2.1: Asymptotic term $\tilde{G}^a$, residual term $\tilde{G}^r$ and total kernel $\tilde{G}$

By taking out the singularity whose integration is available via algebraic function, the

entire computation time is solely determined by the integration of the residual term. Hence the evaluation speed can be greatly improved as well as accuracy. More precisely, one has

$$\begin{aligned} G &= \int_0^\infty \tilde{G}^a \xi J_n(\xi\rho) d\xi + \int_0^\infty (\tilde{G} - \tilde{G}^a) \xi J_n(\xi\rho) d\xi \\ &\equiv G^a + \int_0^\infty \tilde{G}^r \xi J_n(\xi\rho) d\xi, \end{aligned} \tag{2.20}$$

where $\tilde{G}^r = \tilde{G} - \tilde{G}^a$ is the residual term, and $\tilde{G}^a$ is the asymptotic term whose integration is in closed-form as G^a.

2.3 Summary

In summary, the dielectric constant can be used as an indicator to monitor physical quantities and features such as moisture content, air voids and stripping. The estimation of dielectric constant is a primary factor affecting the accuracy of the layer thickness determination. Although the conventional (i.e. travel-time) GPR data interpretation shows the effectiveness for certain occasions, the new technique of full waveform analysis is more versatile owing to its full exploitation of the measurement.

Chapter 3

Correlation with Dielectric

In Chapter 2, it is pointed out that since the variation in the fractional volume of substances can significantly affect bulk dielectric constants, the change of dielectric constants is associated with the change of electrical properties, reflecting the change of the material or structure. To describe such a change, it is worth investigating the factors affecting the value of the dielectric constant.

Dielectric mixing models

There are two ways to determine the dielectric constant: (1) measured values and (2) mixing models. The latter one can provide an estimate of the dielectric constant for a bulk material based on specific parameters using (i) an empirical expression fulfilling the experimental data (Topp et al. 1980) or (ii) a semi-theoretical expression including volume fractions and dielectric constant of each constituent (Roth et al. 1990).

Topp et al. (1980) used a third order polynomial to describe the relation between effective dielectric constant and volumetric water content (VWC):

$$\varepsilon_{eff} = 3.03 + 9.3VWC + 146.0VWC^2 - 76.7VWC^3 \tag{3.1}$$

Conversely the measurement of ε_{eff} can be used to determine VWC by a third polynomial equation:

$$VWC = -5.3 \times 10^{-2} + 2.92 \times 10^{-2}\varepsilon_{eff} - 5.5 \times 10^{-4}\varepsilon_{eff}^2 + 4.3 \times 10^{-6}\varepsilon_{eff}^3 \tag{3.2}$$

More generally, the polynomial model is written as

$$VWC = A + B\ \varepsilon_{eff} + C\ \varepsilon_{eff}^2 + C\ \varepsilon_{eff}^3 \tag{3.3}$$

Another model suggested by Roth et al. (1990) uses the following equation:

$$\varepsilon_{eff} = \left[(1-\eta)\varepsilon_s^n + (\eta - VWC)\ \varepsilon_a^n + VWC\ \varepsilon_w^n\right]^{1/n} \tag{3.4}$$

where η is soil porosity, and subscripts a, s, w represent air, soil and water respectively, and n is a factor accounting for the orientation of the electrical field with respect to the geometry of the medium. Note that $n = 0.5$ is used for isotropic medium (Birchak, 1974), hence a simple physical interpretation of water content and ε was suggested by Herkelrath el. al. (1991):

$$VWC = a\sqrt{\varepsilon_{eff}} + b \tag{3.5}$$

Similarly, Al-Qadi et al. (2004) provided an expression to calculate the voids content in an asphalt sample by knowing parameters of dielectric constant and fractional volume of the aggregate and binder:

$$\sqrt{\varepsilon_{\mathrm{HMA}}} = V_{\mathrm{air}}\sqrt{\varepsilon_{\mathrm{air}}} + V_{\mathrm{agg}}\sqrt{\varepsilon_{\mathrm{agg}}} + V_{\mathrm{b}}\sqrt{\varepsilon_{\mathrm{b}}} + V_{\mathrm{W}}\sqrt{\varepsilon_{\mathrm{W}}} \tag{3.6}$$

where

$\varepsilon_{\mathrm{HMA}}$	=	dielectric constant of the hot mix asphalt layer
V_{air}	=	fractional volume of air
$\varepsilon_{\mathrm{air}}$	=	dielectric constant of the air, equal to 1
V_{agg}	=	fractional volume of aggregate
$\varepsilon_{\mathrm{agg}}$	=	dielectric constant of the aggregate
V_{b}	=	fractional volume of asphalt binder
ε_{b}	=	dielectric constant of the asphalt binder
V_{W}	=	fractional volume of water
ε_{W}	=	dielectric constant of the water, equal to 81.

A more simple expression based on (3.6) is one in which the dielectric constant only depends on air voids:

$$\sqrt{\varepsilon_{HMA}} = V_a\sqrt{\varepsilon_{air}} \tag{3.7}$$

Conversely, the dielectric constant is the only dependent variable of air voids:

$$V_a = c\sqrt{\varepsilon_{eff}} + d \tag{3.8}$$

3.1 Experimental procedure

Four sets of data were obtained from soil (fine-grained and coarse-grained soil samples), and from asphalt concrete (field samples and laboratory samples). All measurements of dielectric constant were taken by percometer.

Percometer

The percometer (Figure 3.1), which consists of a 6-cm-diameter probe attached to a small microprocessor, is an accurate and easy-to-use instrument. The measured value is the real part of the complex relative dielectric constant. When the surface of the probe is pressed against the material to be tested, the device emits a small electrical current. Dielectric

constant and conductivity values are calculated as the current moves through the material between electrodes on the probe.

Figure 3.1: Percometer

3.1.1 Data from fine/coarse-grained soil

Both fine-grained and coarse-grained soils were provided by Minnesota Department of Transportation (Mn/DOT). Four fine-grained soils were selected to represent the range of fine-grained subgrade soils found in Minnesota, with identification letters from A to D. Table 3.1 shows the maximum dry unit weight and optimum moisture contents. The soil samples were prepared and compacted into prismatic samples in a steel container. Cylindrical specimens (101.6 mm in diameter, 381 mm in length) were extracted from the steel container. The measurements of dielectric constant were taken from both prismatic and cylindrical samples (Swenson et al. 2006).

Six coarse-grained soil samples were selected to represent the range of granular materials that would be classified as selected granular or granular, with identification letters from E to J (Davich et al. 2004). As shown in Table 3.2, the fines content varies from 2% to 21.4%; however, the soil are mainly coarse-grained.

3.1.2 Data from MnDOT

Sample cores were taken along a pavement section. Each one was assigned a core id number and the variables used to describe the material are as follows.

Dielectric constant

Table 3.3 lists the dielectric constants of basic pavement related materials, which shows again that the dielectric constant of water can dominate the effective dielectric constant. In other words, it is a good assumption to consider the direct relation between volumetric water

Table 3.1: Fine-grained soil description

Name	Mn Road	Duluth	Red Wing	Red Lake Falls
	Soil A	Soil B	Soil C	Soil D
Average Std. Proctor Dry Unit Weight	106 lb/ft^3	90 lb/ft^3	112 lb/ft^3	103 lb/ft^3
Average Opt. Moisture Content	15%	27%	13%	18%
Average Liquid Limit (%)	28.2	84.6	N/A	38.1
Average Plastic Limt (%)	16.9	32.7	N/A	21.4
Average % Silt	45.7	19.0	81.4	65.4
Average % Clay	13.5	77.0	5.2	25.8
Average R-Value	16.5	10.9	53.8	21.3
Mn/DOT Textural Class.	L	C	S	SiCL
AASHTO Group	A-4, A-6	A-7-6	A-4	A-4, A-7-6
98% Proctor Dry Unit Weight				
100% Opt. Moisture Content	15%	27%	13%	18%
80% Opt. Moisture Content	12%	22%	10%	14%
60% Opt. Moisture Content	9%*	16%	8%	11%
103% Proctor Dry Unit Weight				
90% Opt. Moisture Content	13.5%	24%	12%	16%
75% Opt. Moisture Content	11%	19.5%	9.5%	13%
60% Opt. Moisture Content	9%	16%	8%	11%

Table 3.2: Coarse-grained soil description

Identification Letter	Description	Fines Content	Maximum Density	Optimum Moisture Content
	(AASHTO, ASTM)	%	kg/m^3	%
E	Well-graded sand with gravel (A-1-a, SW)	3.6	2158	7.9
F	Well-graded sand (A-1-b, SW)	4.3	1839	10.0
G	Fine sand with 10% fines (A-3, SP-SM or SP-SC)	10.3	1900	9.3
H	Fine sand with 21% fines (A-2, SM or SC)	21.4	1725	12.6
I	Fine sand (A-3, SP)	2	1791	9.5
J	Well-graded sand with 7% fines (A-1-b, SW-SM or SW-SC)	7.4	2014	8.8

content (see Equation (3.5)) or air voids content (see Equation (3.8)) and effective dielectric constant.

Table 3.3: Dielectric Constants

Material	Dielectric Constant
Air	1
Asphalt	3 to 6
Clay	5 to 40
Concrete	6 to 11
Dry Sand	3 to 5
Granite	4 to 6
Limestone	4 to 8
Saturated Sand	20 to 30
Water	81

Bulk specific gravity of mixture G_{mb}

One important parameter in designing concrete mixes is specific gravity (Sp. Gr.), defined as the mass of a material divided by the mass of an equal volume of distilled water. Four types of specific gravity are defined based on how voids in the compacted mixture are considered. Three of these are widely accepted and used in portland cement and asphalt concrete mix design: *dry weight, saturated surface dry,* and *apparent specific gravity.* These are defined as

$$\begin{aligned}
\text{Dry Sp. Gr.} &= \frac{\text{Dry weight}}{(\text{Total particle volume})\gamma_w} = \frac{W_s}{(V_s + V_i + V_p)\gamma_w} \\
\text{SSD Sp. Gr.} &= \frac{\text{SSD weight}}{(\text{Total particle volume})\gamma_w} = \frac{W_s + W_p}{(V_s + V_i + V_p)\gamma_w} \\
\text{App. Sp. Gr.} &= \frac{\text{Dry weight}}{(\text{Volume not accessible to water})\gamma_w} = \frac{W_s}{(V_s + V_i)\gamma_w}
\end{aligned} \tag{3.9}$$

where

W_s = weight of solids
V_s = volume of solids
V_i = volume of water impermeable voids
V_p = volume of water permeable voids
W_p = weight of water in the permeable voids in the SSD condition
γ_w = unit weight of water

Permeable and impermeable voids are illustrated in Figure 3.2. Only the permeable voids are able to hold water. The amount of water the mixture absorbed is important in the design of portland cement. Depending on how moisture exists in the voids, there are three kind of states: bone dry, air dry, and saturated surface dry (SSD). There is no specific level of mix absorption for a desired mixture, but mix absorption must be evaluated to determine the appropriate amount of water added to the mix.

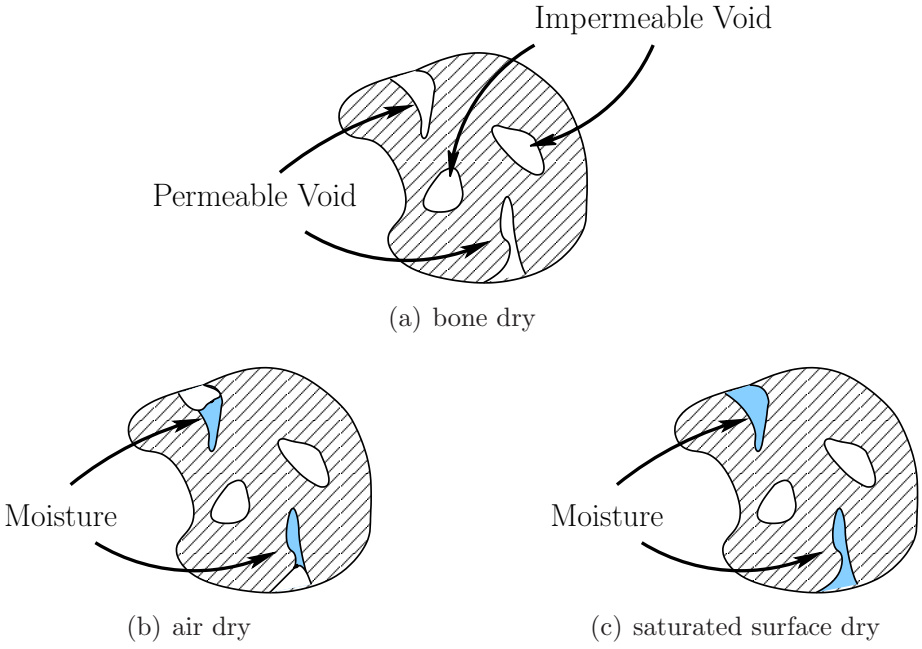

(a) bone dry

(b) air dry

(c) saturated surface dry

Figure 3.2: Voids and moisture absorption of mixtures

In this study, to simplify the problem, we assume that all voids are water permeable voids. In this way, air voids can be calculated by dry specific gravity.

Maximum specific gravity of mixture G_{mm}

In designing a paving mixture with a given aggregate, the maximum specific gravity, G_{mm}, of a given asphalt content is needed to calculate the percentage of air voids. While the maximum specific gravity can be determined for each asphalt content by ASTM D 2041 or AASHTO T 209, the precision of the test is best when the mixture is close to the design asphalt content. Also, it is preferable to measure the maximum specific gravity in duplicate or triplicate.

Percent air voids V_a

According to ASTM D 2041 or AASHTO T 209, the percent air voids in a pavement sample can be calculated using

$$V_a = 100 \times \frac{G_{mm} - G_{mb}}{G_{mm}}\% \tag{3.10}$$

where

V_a = air voids in compacted mixture, percent of total volume
G_{mm} = maximum specific gravity of paving mixture
G_{mb} = bulk specific gravity of compacted mixture

Since G_{mb} represents dry specific gravity, the calculated percent air voids is the total voids in the compacted mixture.

Volumetric water content VWC

Due to the permeable voids, the mixture is able to hold a certain amount of water. The capability to hold water is not simply linearly related to the voids content, but it depends on the versatility of the compound structure and the absorption state. In this study, the SSD state and no impermeable voids are assumed. The volumetric water content (VWC) is defined as

$$\text{VWC} = \frac{\text{SSD weight - Dry weight}}{\text{Dry weight}} \tag{3.11}$$

It can be also defined in terms of gravimetric water content (GWC):

$$\text{VWC} = \frac{\gamma_m}{\gamma_w}\ \text{GWC} \tag{3.12}$$

where γ_m, γ_w are the unit weight of mixture and water respectively, and GWC is defined as

$$\text{GWC} = \frac{\text{SSD weight - Dry weight}}{\text{SSD weight}} \tag{3.13}$$

3.1.3 Data from laboratory asphalt concrete sample

The sample cores were prepared by gyratory compaction as 150mm in diameter and 180mm thick cylinders. Both limestone and granite aggregate were used, as well as two different air voids contents, 4% and 7%.

The samples were first weighed before being submerged into water, and this weight was approximated to be the dry weight. After submersion into water for 15 minutes, the samples were removed and the surfaces were wiped dry; the samples were weighted again under the assumed saturated surface dry (SSD) condition. The effect of water on dielectric constant was illustrated by placing the samples in the air and weighing every consecutive hour for three hours, in which case the water content was gradually reduced.

3.2 Summary

The ultimate goal in these experiments is to find the correlation between dielectric constant and material properties such as water content and air voids content, using the described models by equations (3.3), (3.5) and (3.8). In addition, a linear expression is assumed for the purpose of comparison.

$$\text{VWC} = a\varepsilon_{eff} + b, \quad V_a = c\varepsilon_{eff} + d \tag{3.14}$$

3.2.1 Data from fine and coarse-grained soil

Fine-grained soil

The data set is shown in Appendix Table A-3 and Table A-4. As discussed before, the mixing models include linear (3.5) and polynomial (3.3) relations. Using (3.3), the polynomial trendline is plotted in Figure 3.3 together with linear trendline (see Equation (3.14)). As

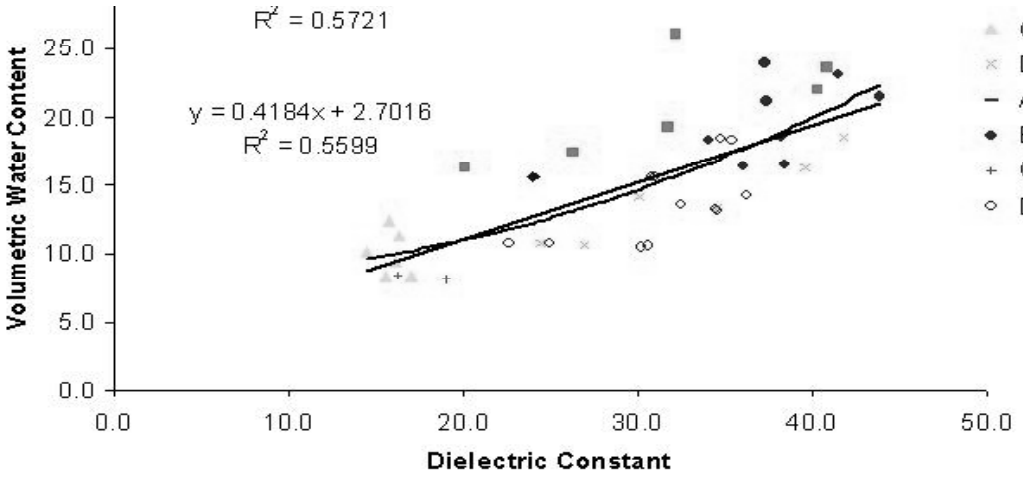

Figure 3.3: Fine-grained soil: dielectric constant vs VWC

shown in Figure 3.3, since the polynomial model only has a slightly higher R^2 compared to linear model, the linear model would be more convenient to predict VWC.

In Figure 3.4, the trendline of square root dielectric constant was plotted as expressed in equation (3.5). The value $R^2 = 0.5464$ is close to the previous models.

Therefore none of the models are working for these fine-grained soils. It is possible because of very small voids and a none-uniformly distributed water content.

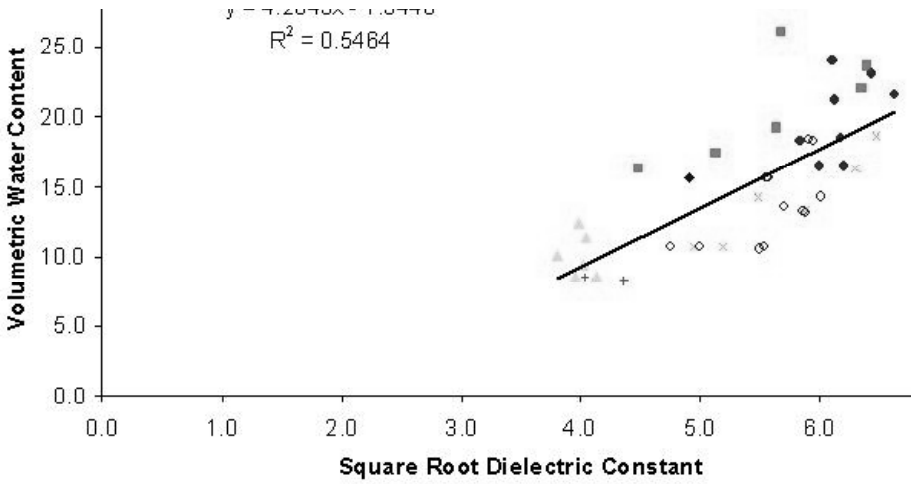

Figure 3.4: Fine-grained soil: square root dielectric constant vs VWC

Coarse-grained soil

The data set is shown in Appendix Table A-5. Since only gravimetric water content data were provided, it is necessary to convert GWC into VWC by (3.13). Both polynomial and linear trendlines were plotted in Figure 3.5.

Figure 3.5 illustrates that both linear and polynomial trendlines have similar R^2 values. For simplicity, the linear one may be easier to use.

Using (3.5), the trendline of square root dielectric constant with $R^2 = 0.8576$ is shown in Figure 3.6. Again, the R value is not much better than linear model.

3.2.2 Field data from MnDOT

According to the data in Appendix Table A-1, those missing maximum specific gravity and those with negative values are unusable. After eliminating that data, the relation between V_a/VWC and ε is readily obtained. According to equations (3.5) and (3.14), the trendlines between VWC and dielectric constant are plotted in Figure 3.7 and Figure 3.8.

As shown in Figure 3.7 and Figure 3.8, both trendlines have very small R^2, meaning that there is virtually no correlation between VWC and dielectric constant for these data.

In Figure 3.10 and Figure 3.9, air voids content and dielectric constant are plotted using (3.8) and (3.14).

As shown in Figure 3.10, the R^2 is very small, indicating that there is no correlation between the air voids content and dielectric constant, as well as the square root of dielectric constant. As can be seen, it is not possible to correlate dielectric constant and water content for this data.

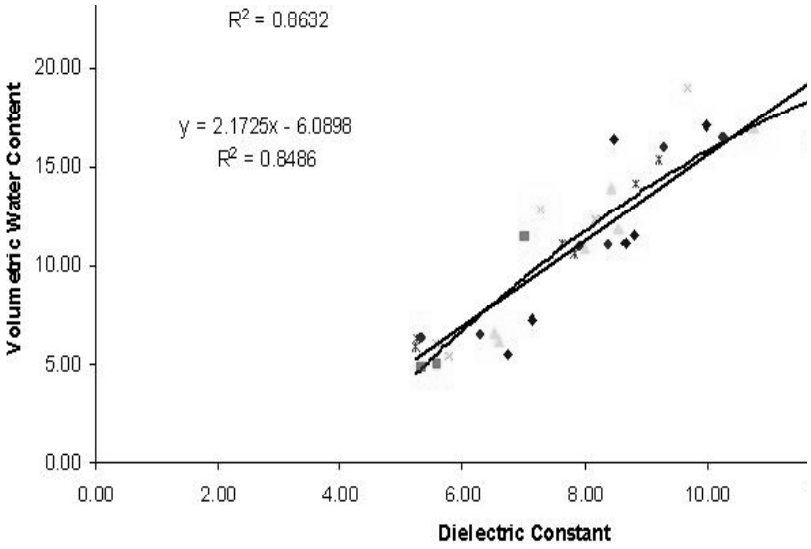

Figure 3.5: Coarse-grained: dielectric constant vs VWC

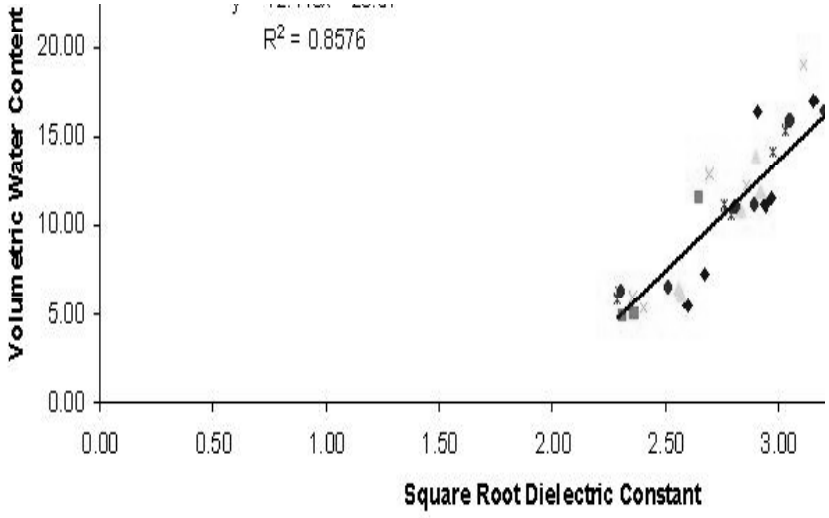

Figure 3.6: Coarse-grained: square root dielectric constant vs VWC

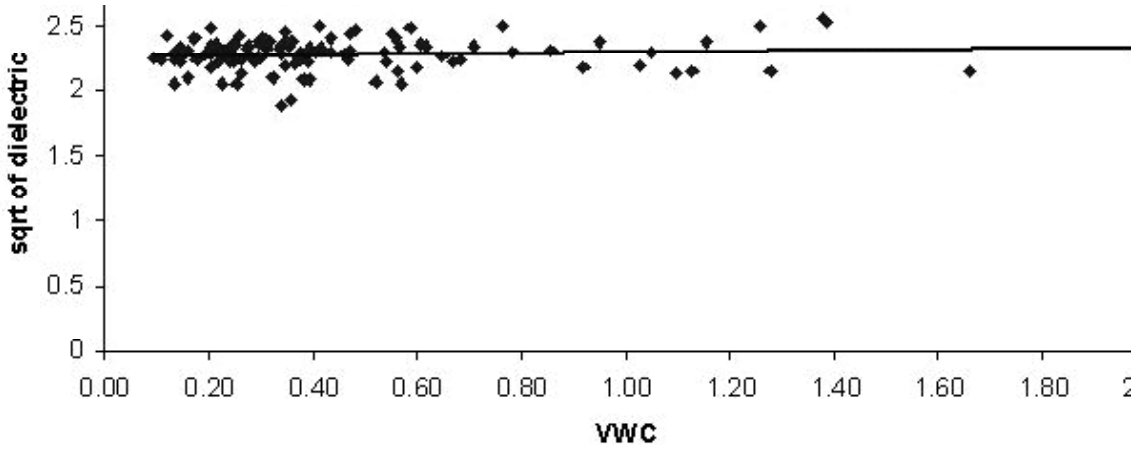

Figure 3.7: Field asphalt concrete: square root dielectric constant vs VWC

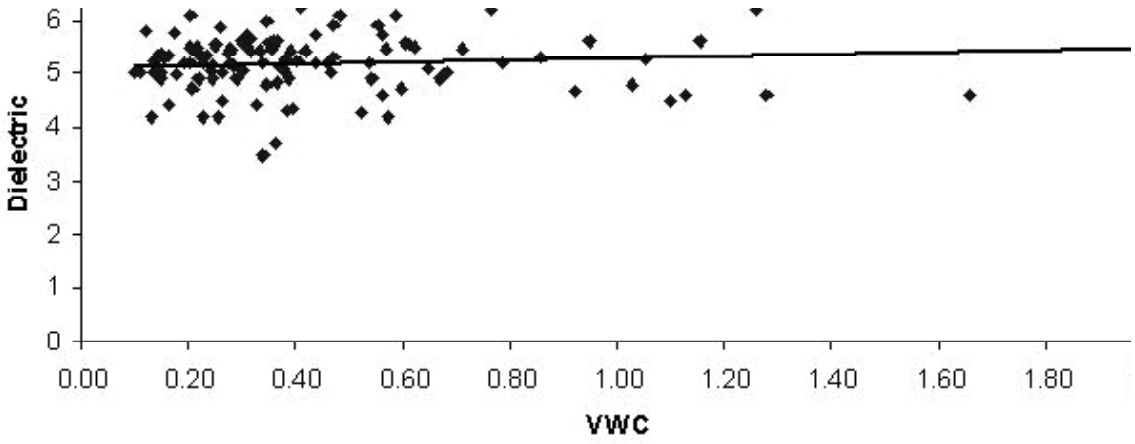

Figure 3.8: Field asphalt concrete: dielectric constant vs VWC

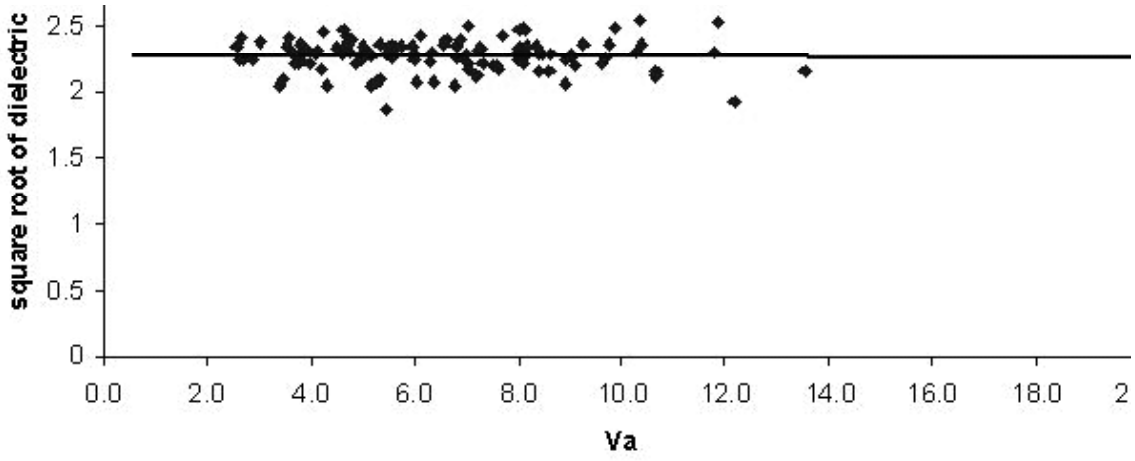

Figure 3.9: Field asphalt concrete: square root dielectric constant vs air voids

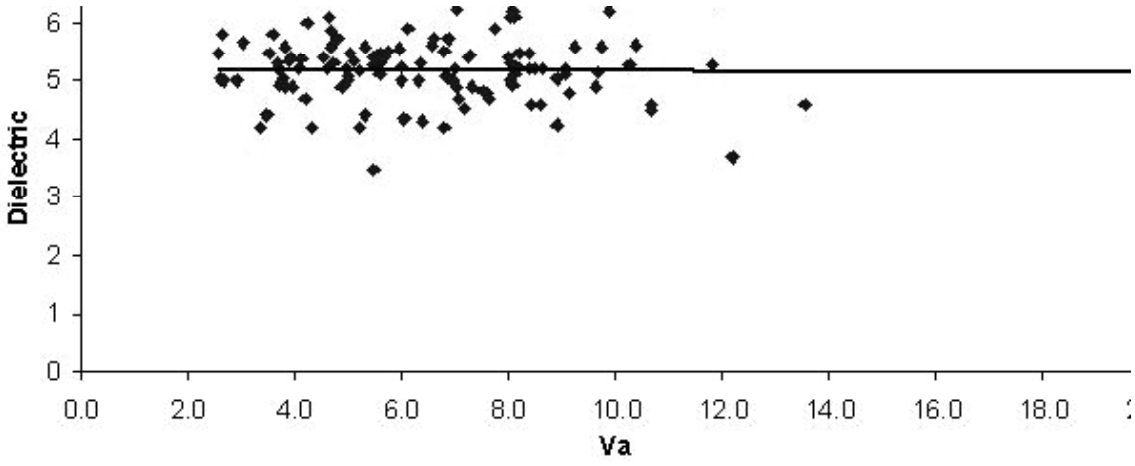

Figure 3.10: Field asphalt concrete: dielectric constant vs air voids

One possible reason for such apparent lack of correlation is the local (near-surface) variation of moisture in asphalt concrete specimens due to ambient humidity conditions. By its nature, such boundary layer could have significantly altered the percometer measurements due to high value of the dielectric constant in water relative to that in asphalt (See Table 3.3), while affecting the overall VWC only minimally. One of the recommendations of this study is to explore such possibility in future projects by either i) attempting to measure the dielectric of asphalt concrete more globally (i.e. using a device alternative to percometer that penetrates deeper into the material), or ii) performing dielectric measurements in an equilibrated moisture environment that would minimize the presence of the above-hypothesized boundary layer.

3.2.3 Data from laboratory asphalt concrete samples

The lab asphalt samples were prepared by gyratory compaction with two different kinds of air voids, 4% and 7% (Appendix Table A-2). Limited by the available data and by the moisture inhomogeneity of the bulk as examined earlier, only qualitative observations are provided.

- For the same sample, the value of dielectric constant of the dry state was lower than any other state (with different drying times).
- For the same sample, the longer the drying time, the smaller the value of the dielectric constant.
- The 4% air voids had, an average, a higher value of dielectric constant than that of 7% air voids at the dry state, and the trend was opposite at the saturated state.
- With the same air voids content, the limestone aggregate sample tended to have a higher effective value of dielectric constant than that of the granite aggregate.

Thus the value of the dielectric constant seems to be increase with the increase of water content. In particular, increasing drying times result in diminishing residual water contents, which in turn produce decreasing values of the dielectric constant. Since the value of dielectric constant in air is smaller than the limestone or granite aggregate (see Table 3.3), the 4% air voids sample would have a higher effective value than that of 7% air voids sample. Also because water has a much higher value of dielectric constant, the saturated 4% air voids sample would possess less water and a smaller effective value of dielectric constant as well. Therefore water content has a great potential to affect the dielectric constant.

Chapter 4

Electromagnetic Waveform Analysis in Layered System

As discussed in Chapter 2, the benefit of using full-waveform analysis is to exploit the GPR data as much as possible, which increases the opportunity to obtain better interpretation of layer properties. Because the full-waveform analysis for layered system is the foundation of this project, it deserves a single chapter for future reference even though the elaborate derivation is given in the Appendix B.

The electromagnetic field is described by the Maxwell's equations. The interrelationship between electric field ($\mathbf{E}$), magnetic field ($\mathbf{B}$), electric charge density(ϱ), and electric current density ($\mathbf{J}$) are formulated by a set of four equations, where, in vacuum, the Maxwell's equations are given as

$$\begin{aligned} \nabla \cdot \mathbf{E} &= \frac{\varrho}{\varepsilon_0} \qquad \nabla \cdot \mathbf{B} = 0 \\ \nabla \times \mathbf{E} &= -\frac{\partial \mathbf{B}}{\partial t} \quad \nabla \times \mathbf{B} = \mu_0 \mathbf{J} + \mu_0 \varepsilon_0 \frac{\partial \mathbf{E}}{\partial t} \end{aligned} \tag{4.1}$$

where $\varepsilon_0 = 8.85419 \times 10^{-12}$F/m as the permittivity in vacuum and $\mu_0 = 4\pi \times 10^{-7}$H/m as the permeability in vacuum. In terms of the speed of light c, one has that

$$c = \frac{1}{\sqrt{\mu_0 \varepsilon_0}}. \tag{4.2}$$

In linear medium, the free space dielectric constant ε_0 is replaced by the material electric permittivity ε, and the free space magnetic permeability μ_0 is replaced by the material magnetic permeability μ as well. Therefore, Maxwell's equations are available in any medium

to describe the field strength via

$$\begin{aligned} \nabla \cdot \mathbf{E} &= \frac{\varrho}{\varepsilon} & \nabla \cdot \mathbf{H} &= 0 \\ \nabla \times \mathbf{E} &= -\mu \frac{\partial \mathbf{H}}{\partial t} & \nabla \times \mathbf{H} &= \mathbf{J} + \varepsilon \frac{\partial \mathbf{E}}{\partial t} \end{aligned} \tag{4.3}$$

where $\mathbf{H} = \mathbf{B}/\mu$ is introduced as auxiliary magnetic field.

The solution of the Maxwell's equations for unbounded system is available in the literature. In layered system such as the ideal pavement system, however, the solution of (4.3) is left to be filled in this project. The schematic of a layered system is shown in Fig. 4.1, where

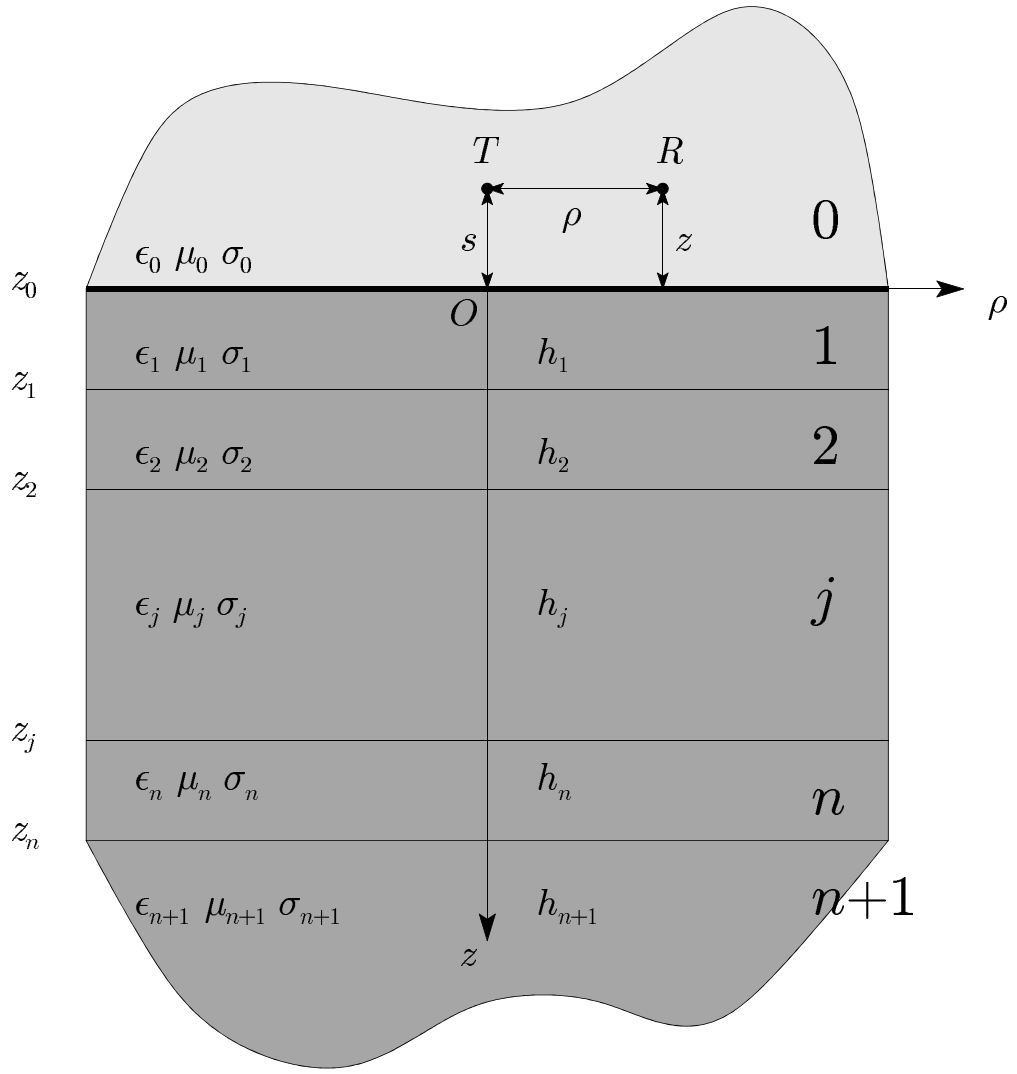

Figure 4.1: Schematic of layered structure

the source (transmitter) T and receiver R are putting in the 0th layer which is the upper

half space (air). The cylindrical coordinate is set on the ground with positive z-direction downward. The spacing information are shown in the figure: the horizontal separation ρ between T and R, the height s for source and the height z for receiver. This setup is applied in order to simulate the GPR configuration where both transmitter and receiver are placed in the box above the ground at the same elevation, i.e., $s = z$. There are total $n + 2$ layers labeled from 0 (upper half space) to $n + 1$ (lower half space). Each layer is characterized by its properties, namely the dielectric constant ε_j, permeability μ_j, conductivity σ_j, and the layer thickness $h_j = z_j - z_{j-1}$ $(j = 0, 1, \cdots, n + 1)$, where z_j is the depth at the bottom of the jth layer. Note that z_{-1} and z_{n+1} represent the artificial outside boundaries of the two half spaces, where the infinity layer thickness should be imposed on. For computational purpose, however, a large preset value is enough to indicate the infinity thickness.

Upon placing the source T in the lth layer, the EM wave would propagate through all the layers. The received EM field at receiver R is the wave field after the multiple reflections and transmissions on all the layer interfaces. The source and receiver are in general arbitrarily located in the layered system. In this project, however, the source T and receiver R happen to be at the same elevation in the top layer (air) due to the configuration of GPR system. The elaborate solution is shown in the Appendix B.

As shown in the Appendix B, the forward model is capable of fast evaluation of the EM field in layered system, which permits the reproduction of the field data from GPR survey. Furthermore, due to the fast evaluation, it is feasible to generate a data base in order to backcalculate the pavement parameters.

Chapter 5

Backcalculation Algorithm

Based on the forward model discussed in the Chapter 4, it is possible to produce the synthetic GPR measurements, i.e. the full electromagnetic waveform (GPR scan) with the time mark and amplitude of the pulse. These waveforms, which contain the information about the layer thickness and dielectric constant, are individually different. In order to assist the analysis in pavement management, those pavement properties should be backcalculated from the measured data. Unlike the traditional travel-time technique, the measurement should be interpreted in a *full-waveform* fashion which has the advantage of exploiting a lot more information from the available data. The focus of this chapter therefore is to introduce a full-waveform back-analysis numerical scheme, which is based on the artificial neural network (ANN) algorithm and frequency response function (FRF) concept.

5.1 Artificial neural network (ANN)

Introduction to ANN

Generally speaking, the artificial neural network (ANN) is introduced as a computational tool to simulate biological neural networks in neuroscience. In practice, it can be used as data modeling aid to simulate complex relationships (patterns) between the input and the output. The type of neural network used here is called feed-forward network, in which the information is transmitted in only one direction, from the input nodes to the output nodes, with no cycles or loops.

Computing unit

Each node, also called neuron, is a computing unit, which performs certain function. One example of an abstract node is shown in Fig. 5.1. The function g on the left side of the node is called the integration function, which generates excitation $g(x)$ from the prescribed input x. The function f on the right side of the node is called the activation function, which uses excitation $g(x)$ to generate the output $y = f(g(x))$. The g function, in general, is an addition

function, whereas the function f employed here can be either linear function or tan-sigmoid function (see Fig. 5.2).

The nonlinear tan-sigmoid activation function permits the network to nonlinearly map the input from $-\infty$ to $+\infty$, to an output from -1 to $+1$. From Fig. 5.2(b) one can see that the tan-sigmoid function becomes more like a step function by increasing the value c. Note that $c = 1$ is applied in this project. On the other hand, the linear activation function provides a convenient tool to map the input to a value outside the range between ± 1. As a result, a network combining these two kinds of nodes is capable of having arbitrary output values.

Network architecture

A feed-forward network can be constructed with either one or multiple layers. Multi-layer network can be constructed in the similar fashion as the one-layer network. Usually, there are two more layers constructed for input and output alone. As an example, a commonly used three-layer feed-forward neural network, which is the simplest, is shown in Fig. 5.3.

On the architecture level, the example network in Fig. 5.3 contains the input layer, the hidden layer and the output layer arranged in the sequential order. Each layer consists of a number of nodes. All the nodes except those in the input layer are computing units. Every node connects only to the nodes in other layers. No connections are allowed between nodes within one layer. In each layer, one bias node is connected to each node in the layer, except in the input layer. The bias is much like a weight, except that it has a constant input of 1.

The number of nodes determines the complexity of the model. In nature, more complicated relationship can be archived with more nodes inside the network. Usually, the number of nodes in the input layer equals to the number of inputs (I); the number of nodes in the output layer equals to the number of outputs (O). The number of nodes in the hidden layer (H) can be adjusted to satisfy the particular requirements.

By adding weight to each connection between two nodes, the network is engaged with more possibilities to model the relationship between the input and the output. The weight represents the connection strength of the input and the weighted total sum of the input; it

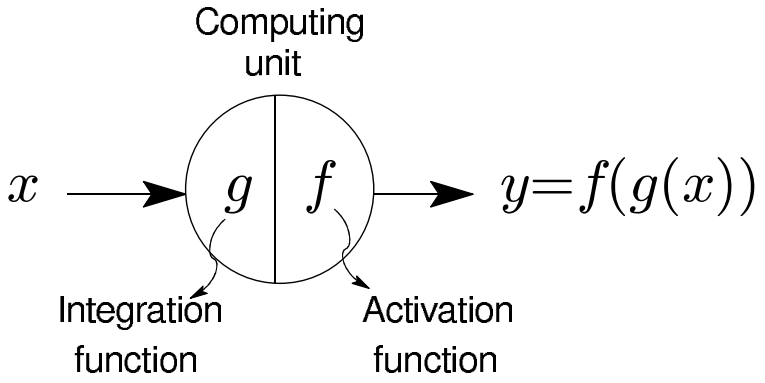

Figure 5.1: Node–computing unit

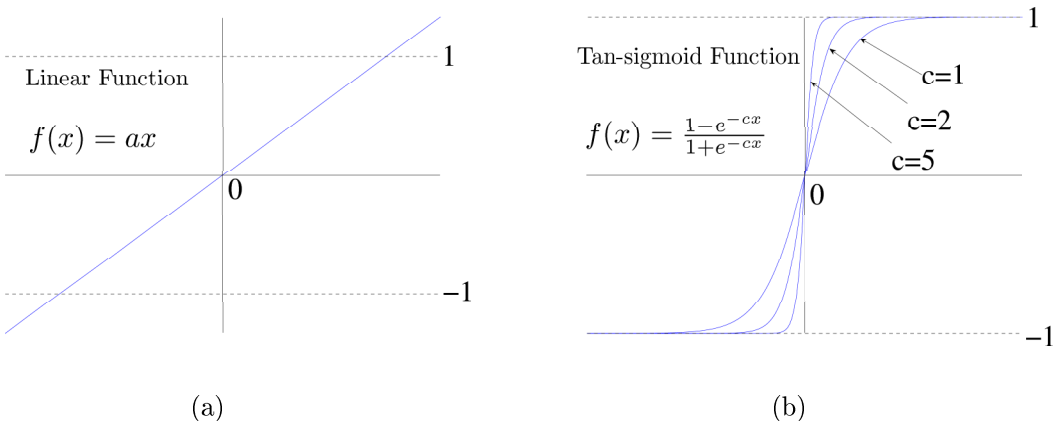

(a) (b)

Figure 5.2: (a) Linear activation function, (b) Tan-sigmoid activation function

is computed as total excitation by the addition function g_1 and g_2. The computed excitation is then evaluated using activation function f_1 and f_2. The function f_1 in the hidden layer is the tan-sigmoid activation function introduced in Fig. 5.2(b), whereas the function f_2 in the output layer is just the linear activation function in Fig. 5.2(a).

Network function

Mathematically, the network is composed of computing units. By performing single primitive functions, each node is capable of evaluating its input. Therefore the network, called the network function (Net$(\cdot)$), is a composite function and its output is a network function of the input. For example, the output vector $\mathbf{y}$ of a neural network with one hidden layer, shown in Fig. 5.3, may be written down in the form as

$$\mathbf{y} = \text{Net}(f_2(\mathbf{W}^2(f_1(\mathbf{W^1 x} + \mathbf{b^1})) + \mathbf{b^2}) \tag{5.1}$$

where $\mathbf{x}$ is the input vector, $\mathbf{W}$ is weight matrix and $\mathbf{b}$ is the bias. Moreover, in the hidden layer, the integration function g_1 in each node computes the weighted total sum, i.e., $g_1(\mathbf{x}) = \mathbf{W^1 x} + \mathbf{b^1}$, where $\mathbf{W}^1$ is the weight matrix between input layer and hidden layer, defined as:

$$\mathbf{W}^1 = \begin{bmatrix} w^1_{1,1} & w^1_{1,2} & \cdots & w^1_{1,I} \\ w^1_{2,1} & w^1_{2,2} & \cdots & w^1_{2,I} \\ \\ w^1_{H,1} & w^1_{H,2} & \cdots & w^1_{H,I} \end{bmatrix} \tag{5.2}$$

and $\mathbf{b}^1 = [b^1_1, \cdots, b^1_H]^T$ is the bias in the hidden layer. Hence, the output of the hidden layer is $f_1(g_1(\mathbf{x})) = f_1(\mathbf{W^1 x} + \mathbf{b^1})$, which is also the input for the next layer. If one defines the weight matrix $\mathbf{W^2}$ between hidden layer and output layer similar to (5.2), in addition to the bias $\mathbf{b^2}$ in the output layer, the total activation for output layer can be written as

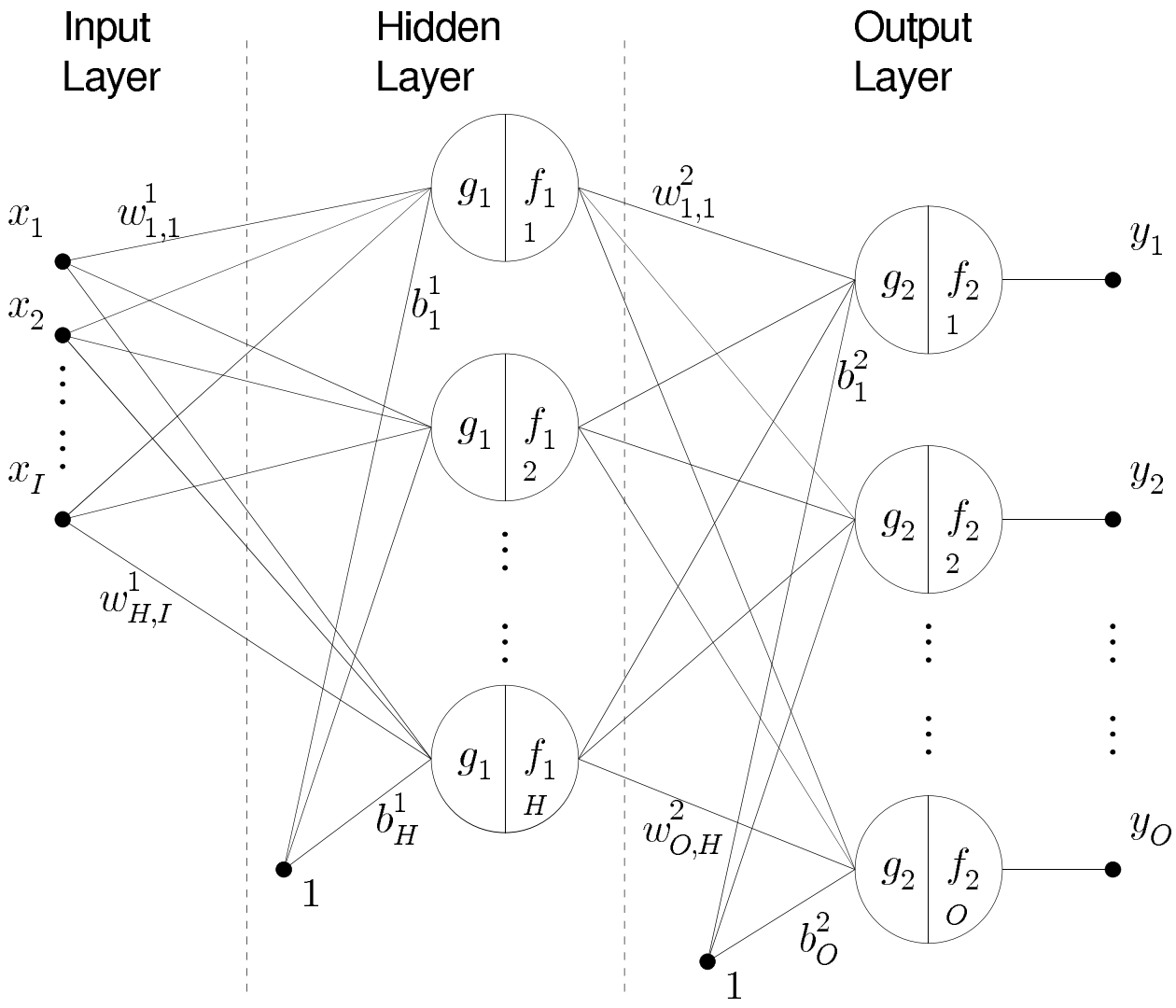

Figure 5.3: Three-layer feed-forward neural network

$\mathbf{W}^2(f_1(\mathbf{W^1x} + \mathbf{b^1})) + \mathbf{b^2}$. After all, the output for the overall network function is obtained as in (5.1) recursively.

Training the network

Neural network is good at performing a particular function only if it learns to do so. The network can be trained so that a particular input leads to a specific target output. Once the network is defined such that the number of nodes and its architecture are fixed as shown in Fig. 5.3, the relation between the input and output is purely determined by the connection between nodes, i.e., the weights and biases. Learning algorithm can be divided into supervised and unsupervised learning. In supervised training, which is used in this project, a set of input and desired target pairs are given. The input is sent to the network

to obtain the network response. By altering the weights associated with the connection, the optimum network function is obtained when the minimum error between the target output and the network response (output) is met (see Fig. 5.4). The network function represents the pattern inside the training data set. The procedure to find the optimum network function is called training. The set of input-target data pairs used to train the network is called the training data set.

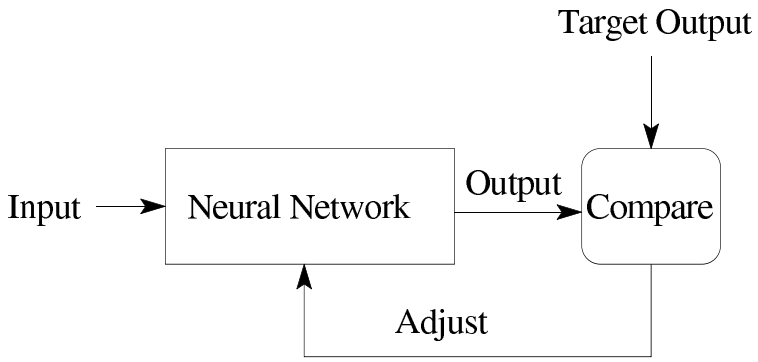

Figure 5.4: Principle of training neural network

Plasticity of network

The number of degrees of freedom (number of weights) available to the network determines whether or not the pattern inside the training set can be learned exactly. The plasticity of the network is determined by the number of degrees of freedom, which means the capability to approximate the pattern. Since the obtained pattern is useful only when it is valid to new data as well as to given data, the trained network has to be verified with new data. As a rule of thumb, too little plasticity leads to large error in both given and new data. Too much plasticity, however, results in less error in given data but also leads to large error in new data. In other words, more than enough plasticity hurts the generality of the network as well as networks with less than enough plasticity. This is shown as an example in Fig. 5.5.

In this example, a noisy sine function is studied by a neural network. The dotted line is the underling sine function, where the noisy sine signals are shown with a '+' sign. The noisy data are sent as training data set to a neural network that has too much plasticity (number of nodes more than enough). The solid line is output obtained from such a network, in which the network tried to fit every single noisy data. Apparently, the network has overfitted the training data, which it failed to generalize well.

In conclusion, the generalization ability depends on the network's plasticity, which in turn is a function of the number of hidden nodes. There is no rigorous rule to define what is the sufficient number of nodes for the network. In the ideal case, the number of degrees of freedom of a network (number of weights between nodes) should not be more than the number of training data sets, because otherwise the network is in danger of being overtrained.

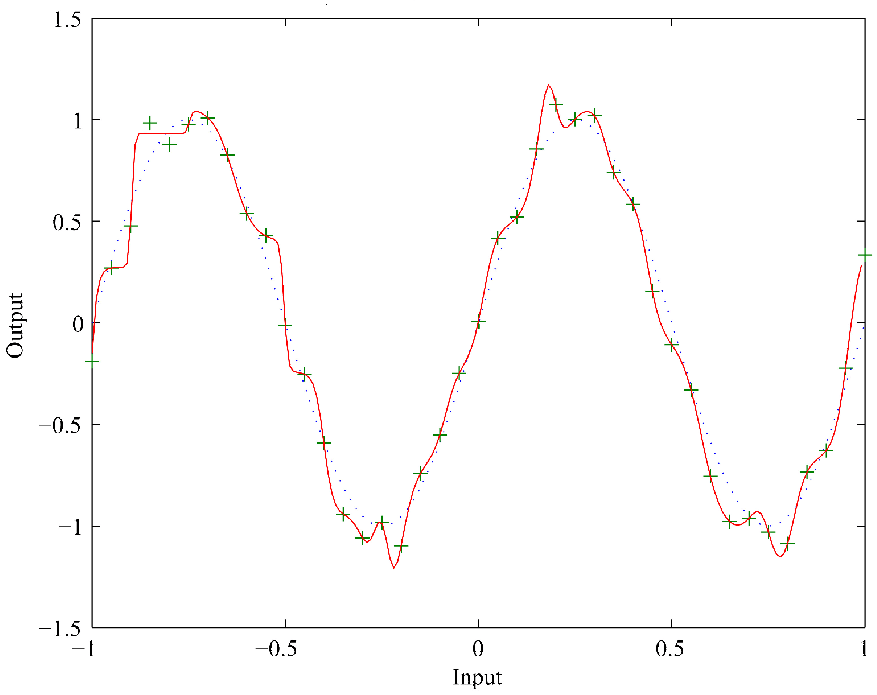

Figure 5.5: Generality of function approximation on a noisy sine function

5.2 Frequency response function (FRF)

Introduction to FRF

For a constant-parameter linear system, which is the case of the GPR system, its dynamic characteristics can be described by frequency response function (FRF). An important property of such a system is that only the amplitude and phase of an applied input can be modified by the system, but the frequency is preserved, which means there is no translation or "leakage" of power between frequencies. If the system output, denoted as $y(t)$, is due to an input $x(t)$, the FRF characterizing the system is defined as:

$$\mathrm{FRF}(f) = \frac{Y(f)}{X(f)} \tag{5.3}$$

where $X(f)$ and $Y(f)$ are the Fourier transforms of the temporal records $x(t)$ and $y(t)$, respectively defined as:

$$\begin{aligned} X(f) &= \int_0^\infty x(t)e^{-i2\pi ft}dt \\ Y(f) &= \int_0^\infty y(t)e^{-i2\pi ft}dt. \end{aligned} \tag{5.4}$$

It is noted that the lower integration limit is 0 since $x(t) = y(t) = 0$ when $t < 0$.

In the GPR system, because the full waveform is generated by the flowing current, the applied current $I(t)$ is the system input, where the GPR measurement $E(t)$ is the system output. After Fourier transformation to the frequency domain, the FRF of the GPR system can be defined as:

$$\mathrm{FRF}^{\mathrm{G}}(f) = \frac{E(f)}{I(f)} \tag{5.5}$$

Note that the FRF function is, in general, a complex value.

Estimation of FRF

In general, two ways are employed to calculate the FRF, (i) direct division in equation (5.3) and (ii) calculation of the relations between power spectra and cross-spectra.

(i) Since the collected measurements are discrete data point within finite time duration, assume that N points of data are evenly sampled at time interval Δt. The signal $x(t)$ and $y(t)$ at $t = n\Delta t$ $(n = 0, 1, 2, \cdots, N-1)$ are replaced by discrete form.

$$x_n = x(n\Delta t), \quad y_n = y(n\Delta t), \quad n = 0, 1, 2, \cdots, N-1 \tag{5.6}$$

In addition, the Fourier transform at N discrete frequency values f_k $(k = 0, 1, 2, \cdots, N-1)$ is computed, where

$$f_k = kf = \frac{k}{N\Delta t} \tag{5.7}$$

Note that, for computational purposes, the number of discrete frequency values is the same as the number of sampled data. Then the discrete Fourier transform is obtained via

$$X_k = \frac{X(f_k)}{\Delta t}, \quad Y_k = \frac{Y(f_k)}{\Delta t}, \quad k = 0, 1, 2, \cdots, N-1 \tag{5.8}$$

Thus, the discrete version of (5.4) are readily shown as

$$\begin{aligned} X_k &= \sum_{n=0}^{N-1} x_n \exp\left[\frac{-i2\pi kn}{N}\right] \\ Y_k &= \sum_{n=0}^{N-1} y_n \exp\left[\frac{-i2\pi kn}{N}\right] \end{aligned} \tag{5.9}$$

where $k = 0, 1, 2, \cdots, N-1$. Based on (5.3),(5.8) and (5.9), when $i = 1, 2, \cdots, M$ realizations of GPR tests are available, the FRF is calculated by

$$\text{FRF}(f_k) = \frac{1}{M} \sum_{i=1}^{M} \left(\frac{Y_k}{X_k}\right)_i. \tag{5.10}$$

(ii)As described in Bendat and Piersol (1971), for a pair of sampling records $x(t)$ and $y(t)$ from stationary random process $\{x(t)\}$ and $\{y(t)\}$, the FRF can be calculated as the ratios of the cross-spectral density S_{xy} to the power spectra density S_{xx}, via

$$\text{FRF}(f) = \frac{S_{xy}(f)}{S_{xx}(f)} \tag{5.11}$$

where the spectral density functions are defined as

$$S_{xy}(f) = \frac{1}{T} X^*(f) Y(f), \quad S_{xx}(f) = \frac{1}{T} X^*(f) X(f) \tag{5.12}$$

where $X(f)$ and $Y(f)$ are the Fourier transforms of $x(t)$ and $y(t)$.

At this point, an important function called the coherence function should be introduced as

$$\gamma_{xy}^2(f) = \frac{|S_{xy}(f)|^2}{S_{xx}(f) S_{yy}(f)}. \tag{5.13}$$

After replacing the spectral functions in (5.13) with (5.12), it follows that

$$\gamma_{xy}^2(f) = \frac{|X(f)Y(f)|^2/T^2}{|X(f)|^2 |Y(f)|^2/T^2} = 1 \tag{5.14}$$

This means, in ideal case of a constant-parameter linear system with no extraneous noise, the coherence function between $x(t)$ and $y(t)$ should be unity. Thus, the coherence function indicates how well these two signals are related. For example, if $x(t)$ and $y(t)$ are completely unrelated, the coherence function is zero. If the coherence function is between zero and one, possibilities are that (i) there is extraneous noise in the measurements in $x(t)$, $y(t)$ or both, (ii) the system is not linear as it is assumed, or (iii) there may be another input other than $x(t)$ which affects $y(t)$. Thus, the quality of the measurement should be calculated before

computing the FRF, where "bad" measurements should be discarded.

When multiple realizations ($i = 1, 2, \cdots M$) of the GPR tests are available, analogous to equation (5.7) and (5.8), the discrete form of (5.12) can be written as

$$\begin{aligned} S_{xy}(f_k) &= \frac{\Delta t}{MN} \sum_{i=1}^{M} (X_k^* Y_k)_i \\ S_{xx}(f_k) &= \frac{\Delta t}{MN} \sum_{i=1}^{M} (X_k^* X_k)_i \end{aligned} \tag{5.15}$$

where $N\Delta t = T$ is the total duration of records. The FRF characterizing the system is then computed as

$$\mathrm{FRF}(f_k) = \frac{S_{xy}(f_k)}{S_{xx}(f_k)}, \quad k = 0, 1, 2, \cdots, N-1 \tag{5.16}$$

and the coherence function is given as

$$\gamma_{xy}^2(f_k) = \frac{|S_{xy}(f_k)|^2}{S_{xx}(f_k) S_{yy}(f_k)}, \quad k = 0, 1, 2, \cdots, N-1 \tag{5.17}$$

FRF patterns

Note that the FRF is generally a complex-valued quantity. As an example, Fig. 5.6 shows the real and imaginary components of FRF, which are the functions of frequency. In a constant-parameter linear system, the shape of the FRF curve is determined by the system parameters that can in turn be identified by interpreting the pattern of FRF. As a note, due to noise contamination during (e.g. GPR) survey, only the FRF within the range around operating frequency is considered to have high S/N ratio. The outside range is noise-polluted or attenuated, therefore is no good for identification.

Due to a digitized (e.g. discrete) nature of experiment data, only discrete data points are involved. To identify the pattern, the simplest way is to analyze the FRF values over the frequency range of interest. In such scheme, however, it is not convenient to deal with individual frequencies which can be highly affected by the experimental noise. As an alternative, the FRF pattern is identified by calculating several segments' area under the curve. As an example illustrated in Fig. 5.6, within the frequency range of interest from f_1 to f_8, the FRF pattern is defined by a combination of seven evenly divided segments. Each segment is associated with two areas under the real and imaginary components of FRF. For instance, the fourth segment as shown in Fig. 5.6, is associated with two areas, Re_4^{area} and Im_4^{area}.

These segmental areas which constitute the FRF pattern are inserted as one set of inputs into the neural network. The neural network automatically interprets the input FRF pattern to the most similar target FRF pattern, if the set of the target parameters are the most similar set of the input parameters. In other words, the neural network is capable of identifying the similarities between the input patterns and the possible pavement parameters.

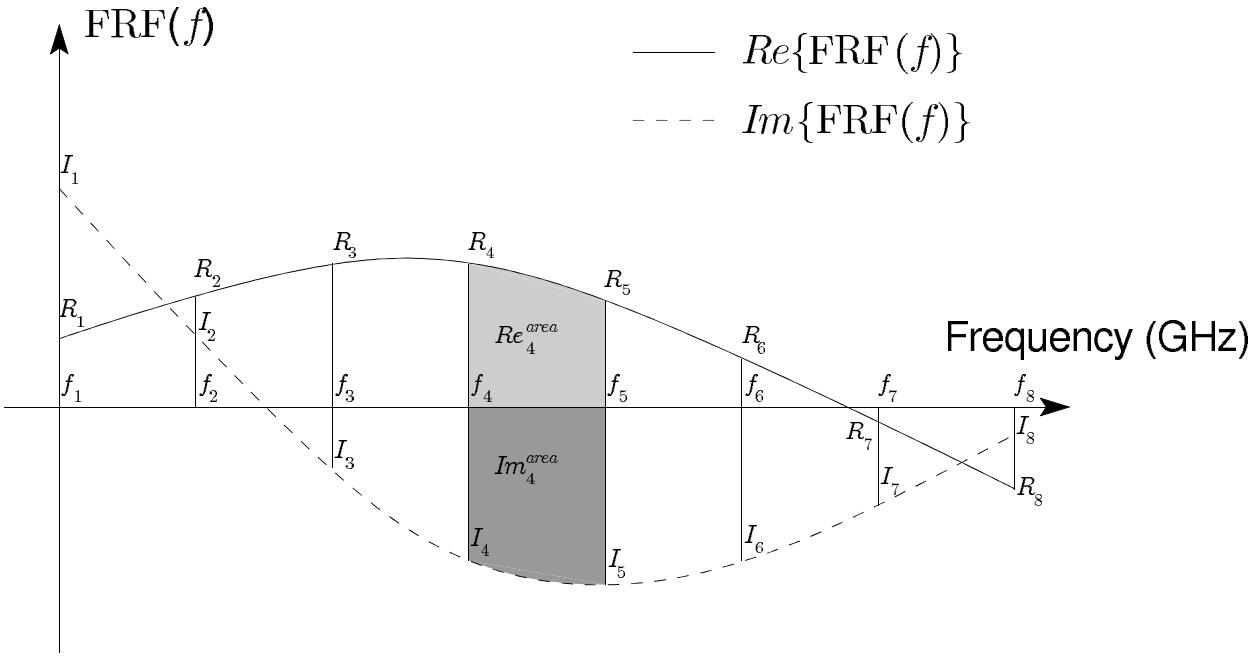

Figure 5.6: Areas under FRF

5.3 Numerical scheme

GPR system profile

The neural network has to be trained before used to interpret the pavement properties, and the training data is generated by the forward model introduced in Chapter 4. Assume that the GPR box is placed above the pavement with transmitter and receiver at the same elevation. As shown in Fig. 5.7, the spacing information (z, d_1, d_2, ρ) is available, namely the height z from the transmitter/receiver to the ground, and the spacings d_1, d_2 and ρ inside the box.

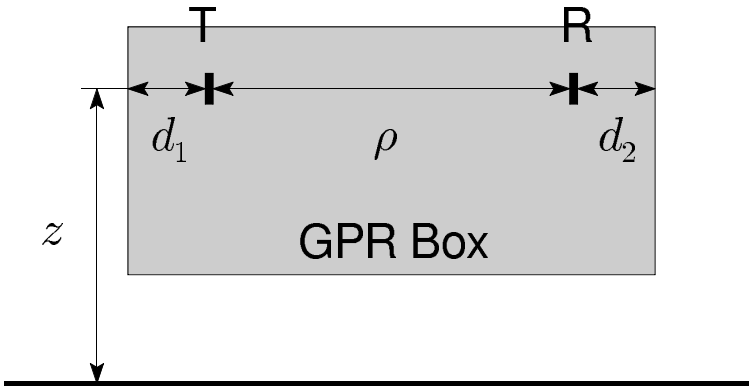

Figure 5.7: Spacings of GPR antenna box

For the two types of GPR antennas operated by Mn/DOT, namely 4105 (2GHz antenna) and 4108 (1GHz antenna), these spacing values are slightly different as listed in Table 5.1. In addition, the height z is fixed at 0.9144 m for both.

Table 5.1: GPR antenna box inside spacings

Type	d_1 [m]	ρ [m]	d_2 [m]
4105	0.0762	0.381	0.0762
4108	0.1016	0.335	0.1016

Due to the fact that the GPR signal is highly attenuated below the base layer, there is very weak reflection from the bottom of the base layer. Therefore, the pavement system is considered as a two-layer system: an asphalt surface layer and a base layer, where the base layer is assumed to be an infinite half space. A schematic of the assumed GPR-pavement system is shown in Fig. 5.8. Three unknown pavement properties as the targeted estimations are circled, namely the dielectric constants of asphalt layer ε_A and base layer ε_B, and the thickness of asphalt layer h_A. The possible range of the featured pavement properties is listed in Table 5.2, where $\varepsilon_0 = 8.8542e^{-12}$F/m is the dielectric constant in the air.

Table 5.2: Pavement properties with variable parameters

	Dielectric Constant [F/m]	Thickness [m]
Asphalt	$\varepsilon_A = 4\varepsilon_0 \sim 8\varepsilon_0$	$h_A = 0.0508 \sim 0.254$m
Base	$\varepsilon_B = 6\varepsilon_0 \sim 12\varepsilon_0$	$h_B = \infty$

Backcalculation procedures

As stated earlier, using a properly-selected training data set, the neural network can be tuned to determine the correlation between the input and output. This is accomplished with synthetic GPR data generated by a computer program, which implements the model of electromagnetic wave propagation in a three dimensional layered pavement structure.

To train the neural network, pavement properties covering the possible range in Table 5.2 will be inserted into the model, as well as the fixed parameters such as spacing z and ρ, air dielectric constant ε_0, and operation frequency f. Despite the temporal shape of the input source, i.e. current pulse, the FRF of the linear system is preserved. Further, the smallest component of any pulse antenna, i.e. the dipole source, is assumed in this study to generate the electromagnetic field.

For the purpose of training, the FRF components in terms of the 14 segmental areas (see Fig.5.6) are computed as discussed before. They are sent to the neural network as input,

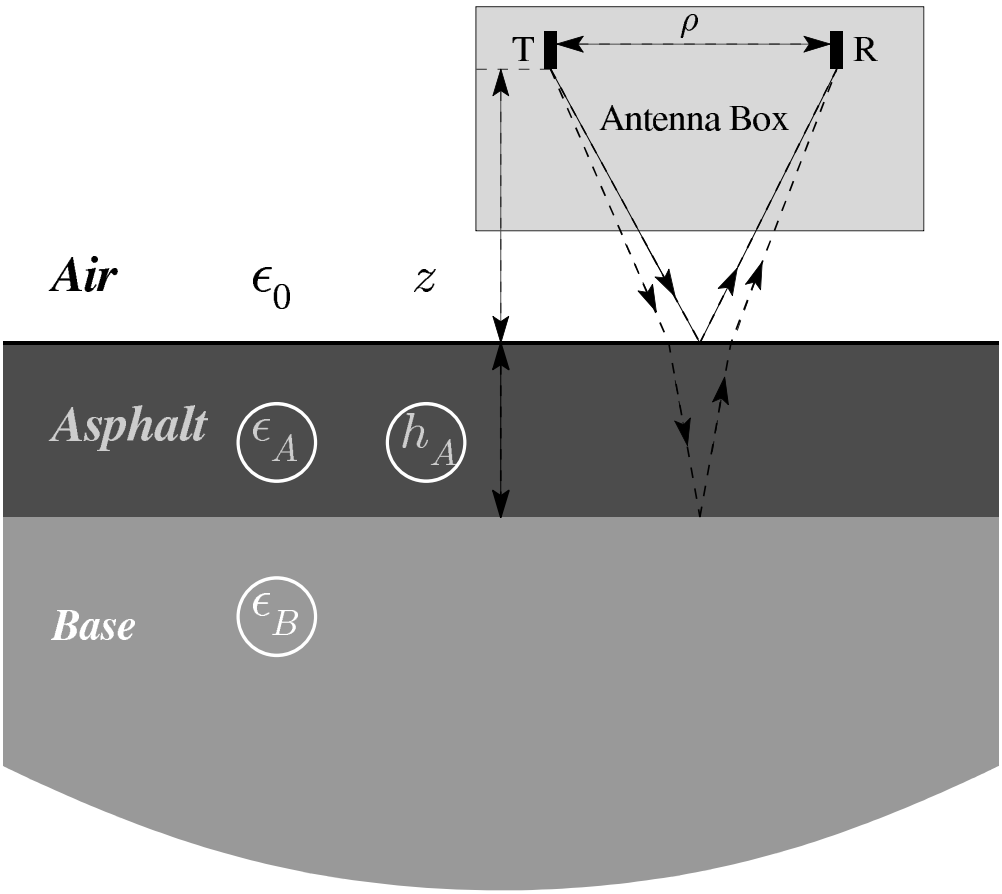

Figure 5.8: GPR implementation configuration

where the target output is the variable pavement properties implemented in the forward model. Note that the two categories of the training and the test data set should be generated separately, where the training data is used to train the neural network and test data is used to verify the trained network.

As a starting point, the network with one hidden layer (I-H-O) is designed, where the number of nodes, I and O, are equal to the number of inputs and outputs (e.g. $I = 14$, $O = 3$), respectively. The maximum number of nodes H_m in the hidden layer is empirically determined by

$$H_m = \text{floor}\left(\frac{N_{\text{eq}}/r - O}{I + O + 1}\right) \tag{5.18}$$

where N_{eq} is the number of independent training equations, i.e., the number of input-output data sets if there are no duplicates. The redundancy parameter r typically varies from 8 to 20 if N_{eq} is sufficiently large. This estimation of H_m is only for practical purposes. The networks with number of hidden nodes larger than H_m are in danger of being overfitted. However, it is good practice to vary H from H_m in order to obtain the optimum relationship between input and output.

To test the generalization ability of alternative (competing) networks with various architectures, neural networks with one output ($O = 1$) in the output layer are also examined. In this case, the network is a combination of three single output networks, where each network is trained separately for a different target.

Selection of parameters

As an illustration, the 1GHz antenna measurement is simulated by the forward model, where the frequency range of interest is taken as 0.8-1.2GHz. The parameters of pavement properties implemented in the forward model are listed below.

1.For the fixed parameters: $z = 0.8763$m, $\rho = 0.335$m, $\varepsilon_0 = 8.8542e^{-12}$F/m.

2.For the variational parameters, a total of N random selections for each parameter is specified, via

$$\begin{aligned} (\varepsilon_A)_i &= \left(4 + (8-4)\frac{\mathcal{R}+i}{N}\right)\varepsilon_0 \\ (\varepsilon_B)_i &= \left(6 + (12-6)\frac{\mathcal{R}+i}{N}\right)\varepsilon_0 \\ (h_A)_i &= 0.0508 + (0.254 - 0.0508)\frac{\mathcal{R}+i}{N} \end{aligned} \tag{5.19}$$

where $i = 0, 1, \cdots, N-1$ and $\mathcal{R}$ is random number from 0 to 1. For practice purposes, in order to randomly spread the parameters (ε_A, ε_B and h_A) over their own data spaces, it is important to generate $\mathcal{R}$ without duplication for every single entry. Therefore, the total combination of these three parameters is N^3, e.g., for $N = 25$, there are $N^3 = 15625$ training data sets.

Neural network results

It should be noted that all the neural networks in this study are implemented in Matlab Neural Network Toolbox (v5.1). This toolbox provides a simple routine to automatically build networks with desired layers, nodes, connection weights and biases. Then the neural network is trained with randomly selected input-output data pairs (x_{tr}, y_{tr}) according to (5.19), where output y_{tr} are the random parameters of $(\varepsilon_A)_i$, $(h_A)_i$ and $(\varepsilon_B)_i$ and input x_{tr} are the system FRFs computed by the forward model assuming y_{tr} and the remaining fixed parameters. New test data pairs (x_{ts}, y_{ts}) are generated separately. During the test stage, the network response a_{ts} is obtained due to the input x_{ts}. The linear regressions between a_{ts} and the target y_{ts} are performed, and the correlation coefficients (R-value) are calculated as well, where the higher R-value represents the better performance of the network.

In what follows, the neural network is designed to have 3 outputs simultaneously ($O = 3$), as shown in Fig. 5.9. As guided by equation (5.18), we select $N_{\text{eq}} = 15625$, $r = 17$, $I = 14$ and $O = 3$, the H_m is calculated as 51. Therefore, the first neural network is created by setting the number of hidden nodes at $H = 51$. Then additional networks with different

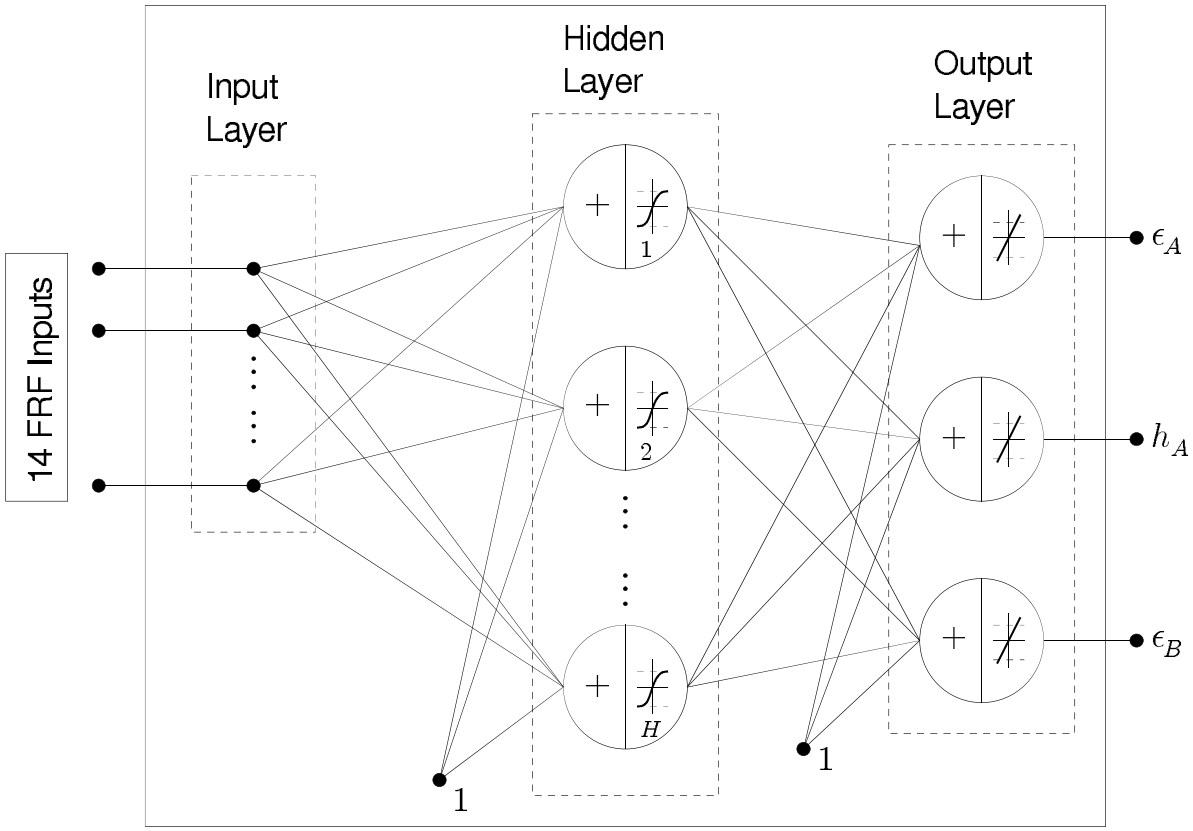

Figure 5.9: Network with three outputs

number of hidden nodes are created by decreasing H of 5 each time until $H = 11$, meaning there are only 11 nodes in the hidden layer. In this way, the number of hidden nodes with respect to optimum network function can be found by comparing the R-value. There are total of 1000 pairs of test data prepared. Each network are verified with the same test data, and the R-values of linear regressions are listed by the order of value H in Table 5.3.

Table 5.3: H vs R-values

H	$R(\varepsilon_A)$	$R(h_A)$	$R(\varepsilon_B)$
11	0.9996	0.7387	0.9988
16	0.9999	0.9146	0.9995
21	0.9999	0.9148	0.9995
26	0.9999	0.8781	0.9997
31	0.9999	0.9364	0.9996
36	0.9999	0.9210	0.9996
41	0.9999	0.9222	0.9996
46	0.9999	0.9161	0.9996
51	0.9999	0.9342	0.9996

From Table. 5.3, the maximum R-values for all three parameters (ε_A, h_A and ε_B) are 0.9999, 0.9364 and 0.9997, respectively, indicating the network is successful in predicting the pavement parameters, namely dielectric constant of asphalt and base layer (ε_A, ε_B) and the thickness of the asphalt layer (h_A). The highest R-value of h_A is 0.9364 when the number of hidden nodes H is 31, whereas $R(\varepsilon_A) = 0.9999$ and $R(\varepsilon_B) = 0.9996$. Therefore the optimum value of H is around 31, where the linear regressions results are plotted in Fig. 5.10.

Another possible spelling for the neural network is a combination of three different single-output networks, as shown in Fig. 5.11. One network is created for each pavement property sought. Because the single output network requires less degrees of freedom compared to multiple outputs network, the size of each network is expected to be smaller. Therefore, $N_{\text{eq}} = 15^3 = 3375$, $r = 8$ and $O = 1$ are selected this time, where $I = 14$ is kept the same as before. As guided by equation (5.18) again, $H_m = 27$ is calculated, which means that the maximum of 27 hidden nodes is needed in each network. Similarly, the network is created first with $H = 27$ hidden nodes. Then different networks are created by decreasing H by a value of 3 each time until $H = 9$. one thousand pairs of test data are generated to verify the trained network with respect to different H values, and the R-values are calculated as shown in Table 5.4.

From Table. 5.4, the maximum R-values for all three parameters, ε_A, h_A and ε_B are 1.0000, 0.9978 and 0.9998, respectively, which means the network is successful in predicting the pavement parameters of the dielectric constants of the asphalt and base layers (ε_A, ε_B) and the thickness of the asphalt layer (h_A). The highest R-value of h_A is 0.9978 when the number of hidden nodes H is 27, whereas $R(\varepsilon_A) = 1.0000$ and $R(\varepsilon_B) = 0.9998$. Therefore the optimum network is obtained when H is around 27, where the linear regression results

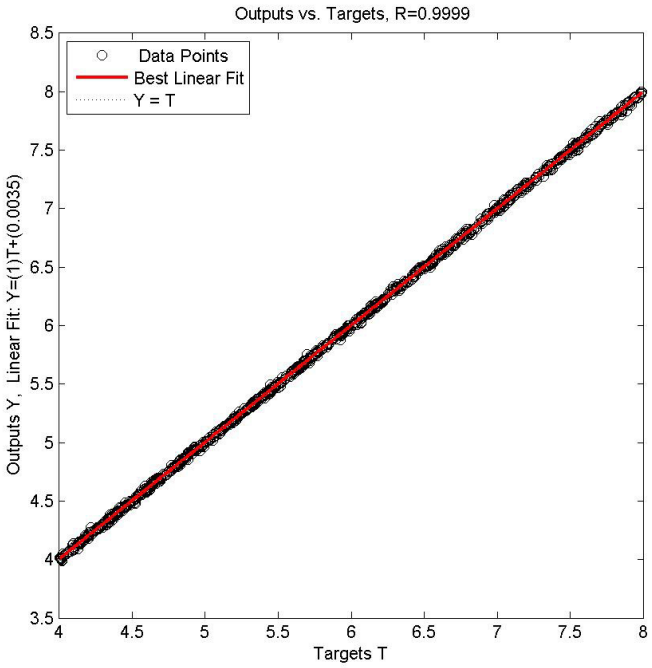

(a) $R = 0.9999$

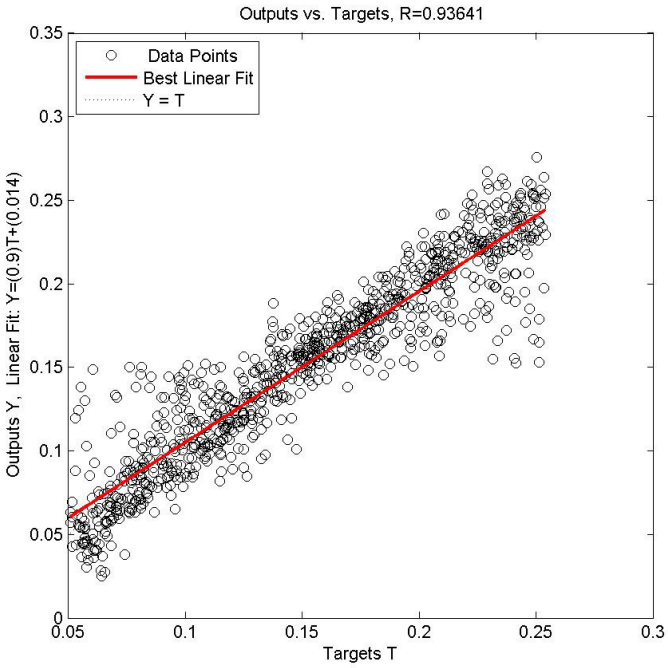

(b) $R = 0.9364$

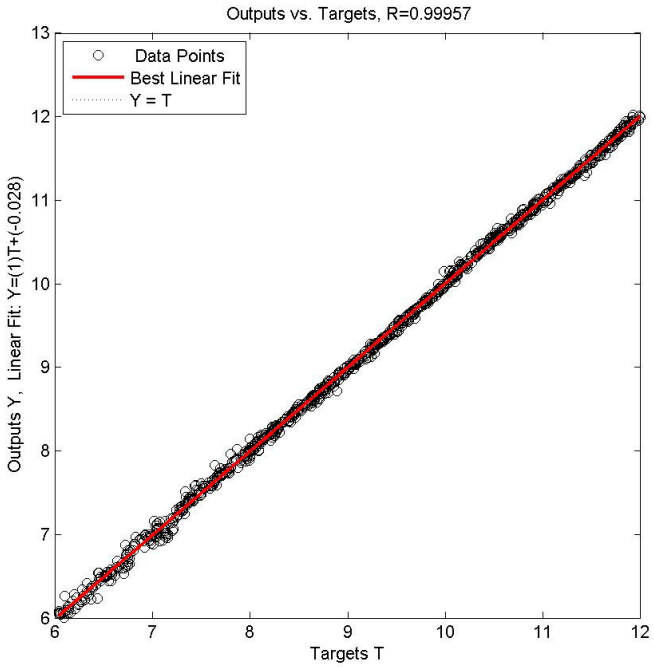

(c) $R = 0.9996$

Figure 5.10: Linear regressions for (a) ε_A, (b) h_A and (c) ε_B ($H = 31$)

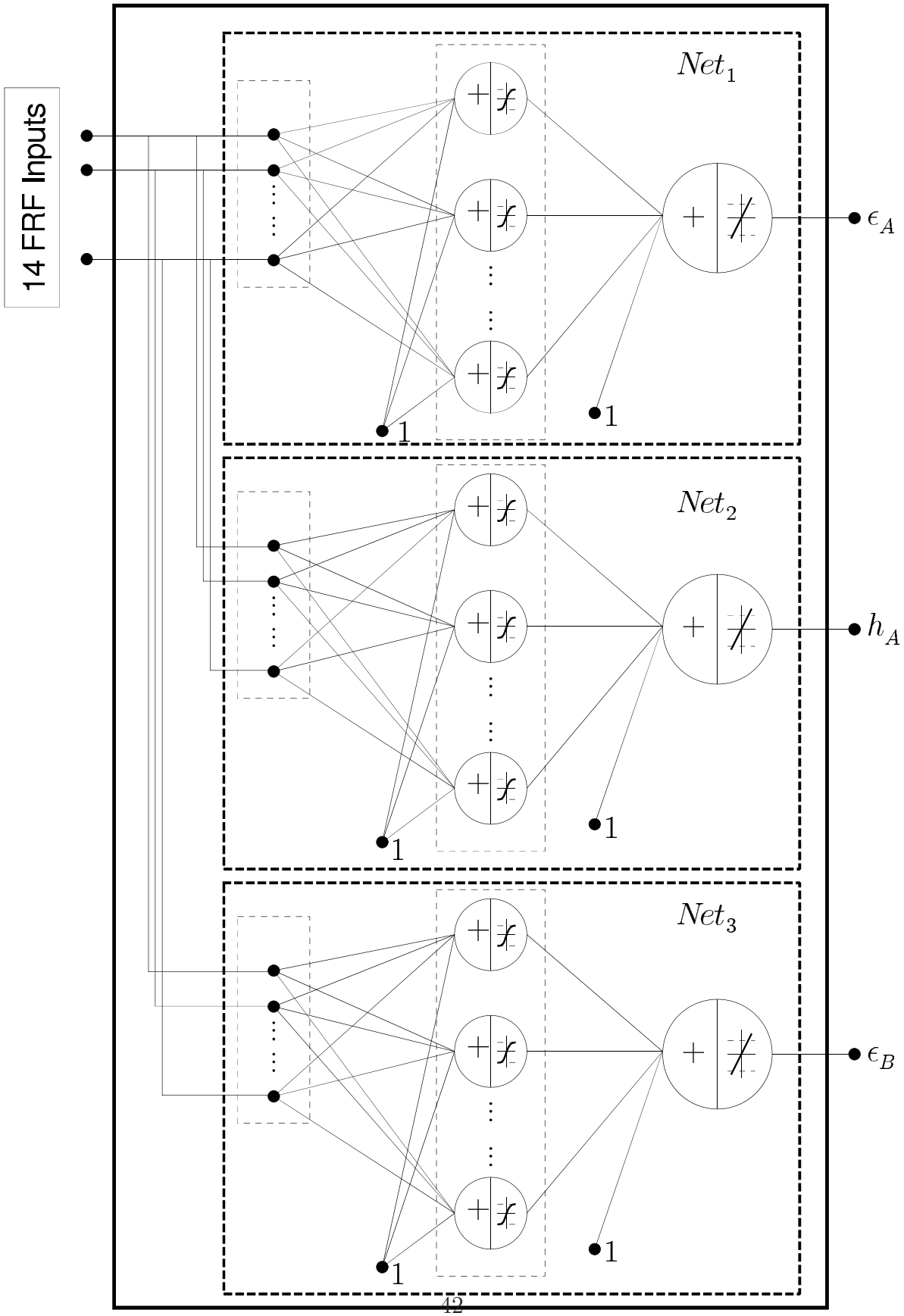

Figure 5.11: Network combined with three single output networks

Table 5.4: R-values vs H

H	$R(\varepsilon_A)$	$R(h_A)$	$R(\varepsilon_B)$
9	1.0000	0.9940	0.9988
12	1.0000	0.9935	0.9996
15	1.0000	0.9938	0.9997
18	1.0000	0.9965	0.9996
21	1.0000	0.9951	0.9998
24	1.0000	0.9973	0.9998
27	1.0000	0.9978	0.9998

of this strategy are plotted in Fig. 5.12.

Conclusion

The above develops two alternative architectures of the neural network, a multi-output network with highest $R(\varepsilon_A) = 0.9999$, $R(h_A) = 0.9364$ and $R(\varepsilon_B) = 0.9996$ vs single-output network with highest $R(\varepsilon_A) = 1.0000$, $R(h_A) = 0.9978$ and $R(\varepsilon_B) = 0.9998$, the performance of the latter one slightly surpasses the former one. When putting in the consideration that the larger size of the network requires larger memory storage and more computation time, it is recommended to use the combination of three single-output networks since this kind of network has smaller architecture than that of multi-output network. In addition, the preliminary results from neural network are obtained via noise free synthetic data which should be modified in accordance with the ambient noise during the GPR survey. In other words, the noise with certain level has to be injected for the training data in order to increase the network's flexibility, which obviously increases the required number of the hidden layer. As a result, the more noise injected, the larger the benefit of the combined network over the single network in terms of the memory storage and computation time.

5.4 Single vs multiple sublayers in asphalt

Simulation with two-layer structure

The presumed layered system only includes two layers, namely the asphalt layer and base layer (see Fig. 5.13(a)). Occasionally however, there are multiple "lifts" or individual layers making up the total asphalt thickness which means the first layer consists of more than only one layer (see Fig. 5.13(b)).

The question arises what will be the overall asphalt layer properties shown in Fig. 5.13(b) that can be captured by the backcalculation scheme for the configuration in Fig. 5.13(a)? Either the effective layer properties of all three overlays in asphalt or only the layer properties of the top overlay will be considered.

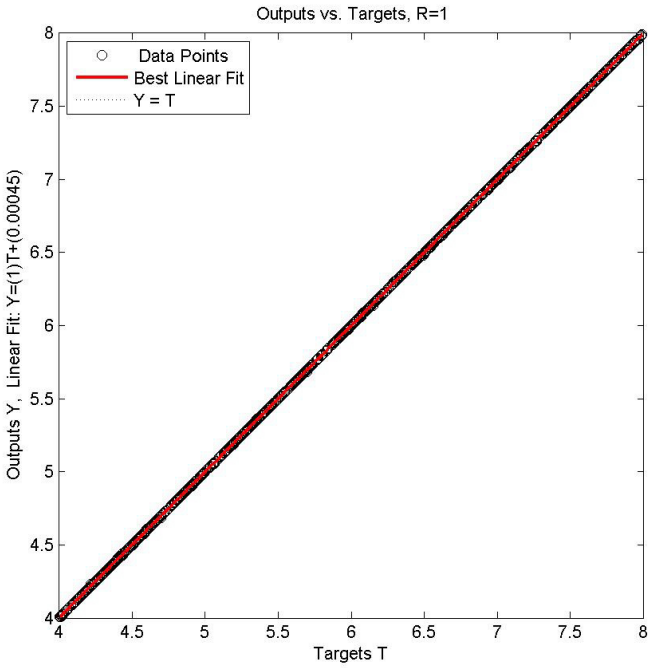

(a) $R = 1.0000$

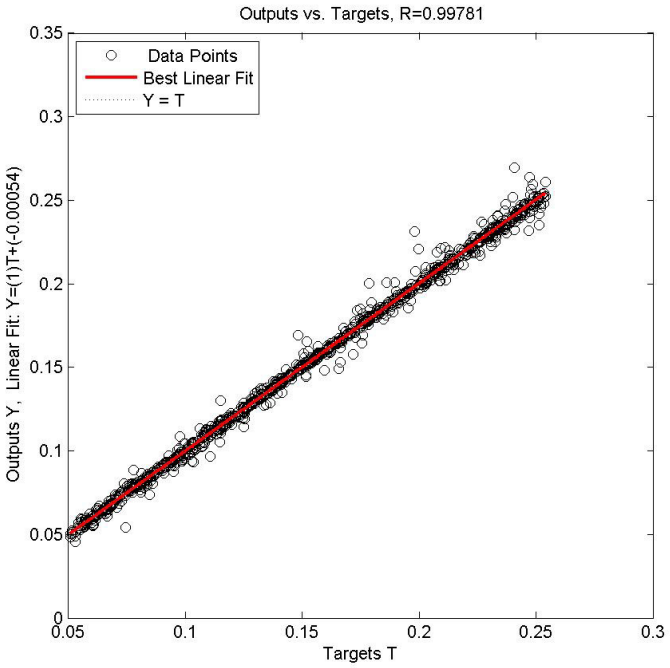

(b) $R = 0.9978$

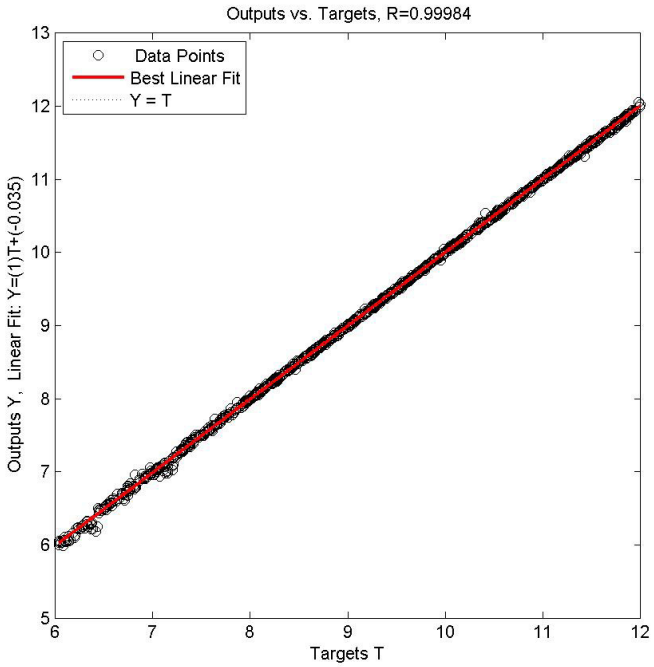

(c) $R = 0.9998$

Figure 5.12: Linear regressions for (a) ε_A, (b) h_A and (c) ε_B ($H = 27$)

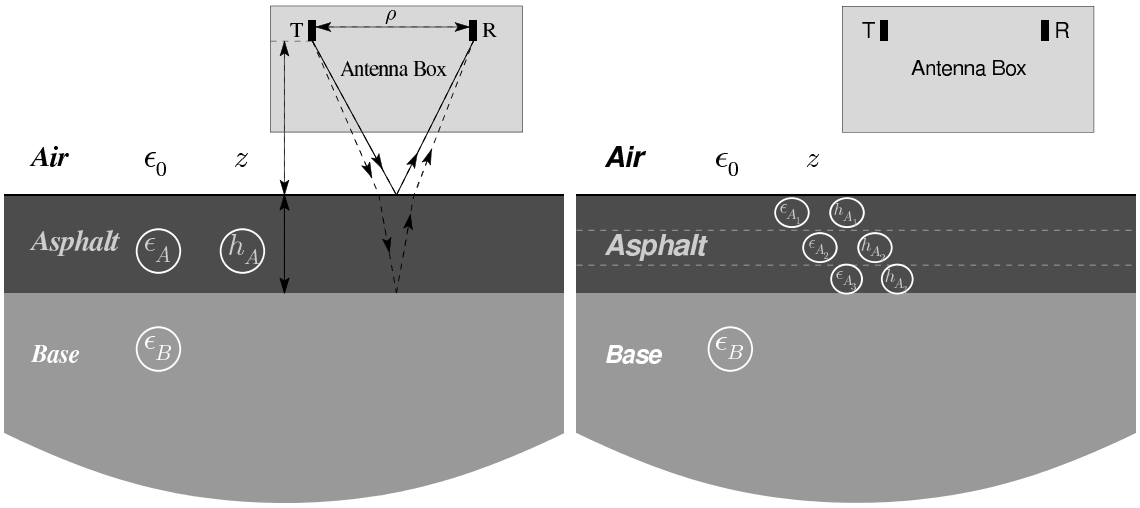

(a) Asphalt of a whole layer (b) Asphalt of three different layers

Figure 5.13: Whole layer vs different layers in asphalt

The selected dielectric properties of the three different overlays are listed in terms of the relative dielectric constant

$$\varepsilon_{A_1} = 6.1\varepsilon_0,\ \varepsilon_{A_2} = 5.2\varepsilon_0,\ \varepsilon_{A_3} = 4.5\varepsilon_0 \tag{5.20}$$

where $h_{A_1} = h_{A_2} = h_{A_3} = 0.8$ in. By applying the backcalculation scheme which assumes the existence of only one layer in asphalt (see Fig. 5.13(a)) to the configuration containing overlays shown in Fig. 5.13(b), the determined asphalt layer parameters are the following

$$\varepsilon_A = 6.27\varepsilon_0,\ h_A = 3.87\text{in}. \tag{5.21}$$

As a result, the effective asphalt dielectric constant ($6.27\varepsilon_0$) is close to the dielectric constant of the top overlay ($6.1\varepsilon_0$), whereas the computed total thickness is deviated from the real one. First of all, the top overlay would reflect a large portion of the total energy, which easily results in an overall determined dielectric constant close to that of the top overlay. On the other hand, after the pulse propagates through the surface layer, there is still energy reflected back from the interfaces of the other layers which is not considered in the backcalculation scheme for a three-layered system. Consequently, the total energy is disturbed, which leads to a layer thickness error as determined by the backcalculation scheme.

Besides the case of multiple thickness layers, the pavement usually contains thin layers which have different dielectric values than that of full-depth composite layer. To study the thin layer effect, the results of a two-overlay structure which has a thin layer over a normal layer inside the asphalt are presented here.

First we examine a three-layered structure which is presented here as a reference. The

pre-defined layer properties are the following:

$$\text{Case 1}: \quad \varepsilon = [1 - 8 - 12]\varepsilon_0, \ h = [\infty - 5.5 - \infty]\text{in}. \tag{5.22}$$

which means that layer one has a dielectric constant of ε_0 and the layer thickness is infinity since it is the upper half space (air); layer two has a dielectric constant of $8\varepsilon_0$ and layer thickness of 5.5 in. (asphalt layer); layer three has a dielectric constant of $12\varepsilon_0$ and the layer thickness is considered to be infinity since it is the lower half space (base layer).

By applying the backcalculation scheme, the determined effective asphalt layer properties are that

$$\text{Case 1}: \quad \varepsilon = [1 - 7.98 - 11.69]\varepsilon_0, \ h = [\infty - 5.27 - \infty]\text{in}. \tag{5.23}$$

which are very close to the true values as expected.

The second example has one more thin layer (h=0.5 in.) with smaller dielectric constant inserted on the top of the asphalt layer while the total layer thickness of the asphalt is kept the same, i.e.,

$$\text{Case 2}: \quad \varepsilon = [1 - 2 - 8 - 12]\varepsilon_0, \ h = [\infty - 0.5 - 5 - \infty]\text{in}. \tag{5.24}$$

In return, the determined layer properties are the following.

$$\text{Case 2}: \quad \varepsilon = [1 - 4.8 - 12.34]\varepsilon_0, \ h = [\infty - 3.32 - \infty]\text{in}. \tag{5.25}$$

As one can see, because of the thin layer which has lower dielectric constant value, the overall dielectric constant is reduced from the normal value towards the smaller value, whereas the dielectric value of base layer has little change. However, the determined total layer thickness of asphalt (3.32 in.) is deviated from the true value (5.5 in.).

In the third and fourth examples, the thin layer is still on the top of the asphalt layer but with higher dielectric constant values than that of the normal layer underneath, i.e.,

$$\begin{aligned} &\text{Case 3}: \quad \varepsilon = [1 - 8 - 2 - 12], \ h = [\infty - 0.5 - 9.5 - \infty]\text{in}. \\ &\text{Case 4}: \quad \varepsilon = [1 - 8 - 2 - 12], \ h = [\infty - 0.5 - 7 - \infty]\text{in}. \end{aligned} \tag{5.26}$$

As a return, the determined layer properties are that

$$\begin{aligned} &\text{Case 3}: \quad \varepsilon = [1 - 2.5 - 11.58], \ h = [\infty - 10.12 - \infty]\text{in}. \\ &\text{Case 4}: \quad \varepsilon = [1 - 2.1 - 15.25], \ h = [\infty - 5.36 - \infty]\text{in}. \end{aligned} \tag{5.27}$$

In both case 3 and case 4, the determined dielectric constants of asphalt ($2.5\varepsilon_0$ and $2.1\varepsilon_0$) are close to the values of the normal layer ($2\varepsilon_0$), whereas the determined dielectric value of base layer in case 3 ($11.58\varepsilon_0$) is close to the true value ($12\varepsilon_0$) and in case 4 ($15.25\varepsilon_0$) it is not. For the layer thickness, in case 3, the determined total thickness of asphalt is 10.12 in. which is very close to the true value (10 in.), whereas in case 4, the determined total thickness of asphalt (5.36 in.) is not close to the true value (7.5 in.).

In conclusion, because the thin layer is very small, smaller than the wavelength, the

electromagnetic wave will propagate through the whole layer without much change. However, the first reflection from the top of the thin layer will still has effect to some degree. Thus, the overall dielectric constant tend to be deviated from the value of normal layer towards the value of the thin layer. In certain occasions, the thin layer has almost none effect to the wave propagation, therefore, the determined layer thickness is close to the actual thickness as shown in case 3.

Simulation with three-layer structure

To address the problem with sublayers inside the asphalt, the more practical way is to redefine the layer structure for the forward model and neural network. Instead of assuming a two-layer pavement system (asphalt and base layer), a three-layer pavement system including two sublayers and one base layer should be employed as shown in Fig. 5.14, where the total number of parameters has increased to 5. Therefore new simulations of GPR data has to be generated, and new neural network has to be trained as well.

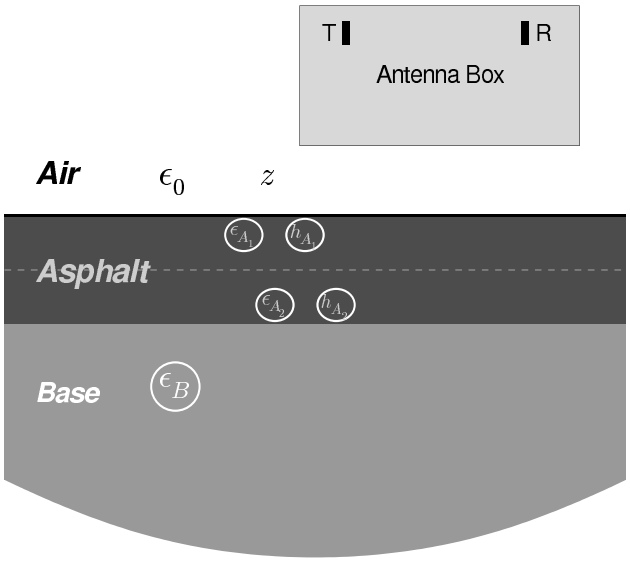

Figure 5.14: Two sublayers in asphalt

To reduce the time to generate training data for the neural network, two sublayers have been assumed with equal thickness, with different dielectric constants. In this newly defined system the number of unknown parameters is 4, namely the dielectric constant of the first/second sublayer in the asphalt ($\varepsilon_{a,1}$ and $\varepsilon_{a,2}$), the dielectric constant of the base layer (ε_b), and the thickness of the first sublayer ($h_{a,1}$). Even with this reduced configuration, with ten different values for each parameters the total number of the data sets is $10^4 = 10,000$. In addition, based on the experience of the backcalculation with neural network, the dielectric constant in the first sublayer always has the better R value than the other parameters. As a result, one may decrease the needed number of different values for $\varepsilon_{a,1}$ and increase that

for $h_{a,1}$. The modified scheme to generate the training data set has 5 values for $\varepsilon_{a,1}$, ε_b and 20 values for $\varepsilon_{a,2}$ and $h_{a,1}$, which results in a total number of 10,000 data sets.

In the training stage, different architectures of neural network including single network with 4 outputs and combination of 4 networks with 1 output of each one is applied, and various number of hidden nodes from 10-40 is applied as well. Based on a large number of simulations, it turns out that the combined neural network with $H = 30$ hidden nodes in each one has the best performance. The detailed results for each network are omitted here for simplicity.

To show the effectiveness of the new configuration, numbers of circumstances with different layer parameters has been verified. For instance, assume $\varepsilon = [1 - 4 - 8 - 10]\varepsilon_0$ and $h = [\infty - 1.5 - 1.5 - \infty]$ in., the determined parameters are $\varepsilon = [1 - 3.99 - 8.35 - 9.71]\varepsilon_0$ and $h = [\infty - 1.48 - 1.48 - \infty]$ in. A selected list of the results of test runs are shown in Table 5.5.

As shown, the error of the determined dielectric constant and thickness of the first sublayer is quite small, as low as 0.089%, whereas the errors of the determined dielectric constant of the second sublayer and base are acceptable for some instances. Also, it is observed that in the case where the two sublayers have equal (or close) dielectric constant of small value ($< 4\varepsilon_0$), the error of the determined $h_{a,1}$ is larger compare to the case where the two sublayers have different dielectric value. Fortunately, unless severe stripping happens, the circumstance with small dielectric value through out the whole asphalt layer is very limited. Therefore, one may determine the parameters of the structure with two sublayers and one base layer by the back-analysis scheme introduced in this chapter.

5.5 Summary

The backcalculation scheme is proposed and verified with synthetic data generated based on the EM model introduced in Chapter 4. The results show that the scheme works well for interpreting the parameters of pavement system. However, it should be noted that different layer structures require a different setup for the scheme. For example, if sublayers are assumed in the asphalt, at least the three-layer system instead of two-layer system has to be applied. Otherwise, it is beyond the capabilities of the backcalculation. Given enough time to generate data and train the network, this backcalculation scheme will work as long as the assumed structure fits the desired system. In addition, several notes about the neural network are listed below for future reference.

First, the neural networks developed in this study are all implemented using Matlab Neural Network Toolbox (v5.1). They may not be back-compatible with previous Matlab versions.

Second, the most effective architecture of neural network was found to be the three-layer feed-forward network. More than one hidden layer is not necessary unless there are limited computing resources, such as available memory. Because the nodal information has to be stored in a computer when computation is performed for a layer, large number of nodes in one layer directly results in large memory storage needs. Since the plasticity of network is

Table 5.5: Test runs of 3-layered system: 2 sublayers + base layer

Defined value	Determined value
$\varepsilon = [1 - 4 - 8 - 10]\varepsilon_0$ $h = [\infty - 1.5 - 1.5 - \infty]$ in.	$\varepsilon = [1 - 3.99 - 8.35 - 9.71]\varepsilon_0$ $h = [\infty - 1.48 - 1.48 - \infty]$ in.
$\varepsilon = [1 - 4 - 8 - 10]\varepsilon_0$ $h = [\infty - 2.5 - 2.5 - \infty]$ in.	$\varepsilon = [1 - 3.98 - 7.41 - 9.30]\varepsilon_0$ $h = [\infty - 2.36 - 2.36 - \infty]$ in.
$\varepsilon = [1 - 4 - 8 - 10]\varepsilon_0$ $h = [\infty - 3 - 3 - \infty]$ in.	$\varepsilon = [1 - 3.96 - 8.25 - 9.32]\varepsilon_0$ $h = [\infty - 2.9 - 2.9 - \infty]$ in.
$\varepsilon = [1 - 4 - 8 - 10]\varepsilon_0$ $h = [\infty - 4.5 - 4.5 - \infty]$ in.	$\varepsilon = [1 - 3.97 - 8.08 - 9.68]\varepsilon_0$ $h = [\infty - 4.54 - 4.54 - \infty]$ in.
$\varepsilon = [1 - 6 - 3 - 15]\varepsilon_0$ $h = [\infty - 1.1 - 1.1 - \infty]$ in.	$\varepsilon = [1 - 6.09 - 2.35 - 14.75]\varepsilon_0$ $h = [\infty - 0.97 - 0.97 - \infty]$ in.
$\varepsilon = [1 - 6.5 - 4.2 - 12]\varepsilon_0$ $h = [\infty - 1.8 - 1.8 - \infty]$ in.	$\varepsilon = [1 - 6.58 - 4.53 - 12.80]\varepsilon_0$ $h = [\infty - 1.67 - 1.67 - \infty]$ in.
$\varepsilon = [1 - 8.2 - 2.2 - 16]\varepsilon_0$ $h = [\infty - 2.5 - 2.5 - \infty]$ in.	$\varepsilon = [1 - 8.30 - 2.18 - 15.76]\varepsilon_0$ $h = [\infty - 2.68 - 2.68 - \infty]$ in.
$\varepsilon = [1 - 6.6 - 5.2 - 10]\varepsilon_0$ $h = [\infty - 3.8 - 3.8 - \infty]$ in.	$\varepsilon = [1 - 6.67 - 5.14 - 10.76]\varepsilon_0$ $h = [\infty - 3.84 - 3.84 - \infty]$ in.
$\varepsilon = [1 - 8.4 - 8.4 - 12]\varepsilon_0$ $h = [\infty - 1.1 - 1.1 - \infty]$ in.	$\varepsilon = [1 - 8.38 - 9.83 - 12.20]\varepsilon_0$ $h = [\infty - 1.24 - 1.24 - \infty]$ in.
$\varepsilon = [1 - 7.2 - 7.2 - 10]\varepsilon_0$ $h = [\infty - 1.5 - 1.5 - \infty]$ in.	$\varepsilon = [1 - 7.24 - 8.70 - 10.35]\varepsilon_0$ $h = [\infty - 1.70 - 1.70 - \infty]$ in.
$\varepsilon = [1 - 6.4 - 6.4 - 12]\varepsilon_0$ $h = [\infty - 1.1 - 1.1 - \infty]$ in.	$\varepsilon = [1 - 6.29 - 7.30 - 12.11]\varepsilon_0$ $h = [\infty - 1.45 - 1.45 - \infty]$ in.
$\varepsilon = [1 - 3.1 - 3.1 - 10]\varepsilon_0$ $h = [\infty - 1.2 - 1.2 - \infty]$ in.	$\varepsilon = [1 - 3.17 - 6.82 - 12.08]\varepsilon_0$ $h = [\infty - 1.79 - 1.79 - \infty]$ in.
$\varepsilon = [1 - 8.2 - 8.2 - 12]\varepsilon_0$ $h = [\infty - 4.5 - 4.5 - \infty]$ in.	$\varepsilon = [1 - 8.26 - 7.9 - 10.87]\varepsilon_0$ $h = [\infty - 4.62 - 4.62 - \infty]$ in.
$\varepsilon = [1 - 7.2 - 7.2 - 12]\varepsilon_0$ $h = [\infty - 2.2 - 2.2 - \infty]$ in.	$\varepsilon = [1 - 7.24 - 6.89 - 12.83]\varepsilon_0$ $h = [\infty - 1.95 - 1.95 - \infty]$ in.
$\varepsilon = [1 - 6.5 - 6.5 - 15]\varepsilon_0$ $h = [\infty - 3 - 3 - \infty]$ in.	$\varepsilon = [1 - 6.62 - 6.21 - 15.53]\varepsilon_0$ $h = [\infty - 2.61 - 2.61 - \infty]$ in.

Note: $\varepsilon = [\varepsilon_0 - \varepsilon_{a,1} - \varepsilon_{a,2} - \varepsilon_b]$ and $h = [\infty - h_{a,1} - h_{a,2} - \infty]$ in.

determined by the degrees of freedom (number of weights), therefore, one layer can be split into several layers whose combination have the same degrees of freedom. However, there is a trade-off between the available resource and computation time – a multi-layer network requires less memory but more time to archive the same goal of one-layer network.

Lastly, the size of neural network is generally based on the available training data sets. If the set is small, according to equation (5.18), the H_m is small as well. However, the network with H_m hidden nodes may not have enough plasticity to perform the required relations inside training data. Because of overfitting, however, having more hidden nodes than the recommended value H_m is also not desirable. Too much plasticity of network kills the network generalization ability as well. The redundancy parameter r from 10 to 20 in equation (5.18) is also altered depending on the number of training sets. For example, more redundancy would be expected when the number of sets is sufficiently large, then $r = 20$ is reasonable to use. If the number of training sets is barely sufficient, then smaller r should be used. Whether or not there is a sufficient number of sets depends on the type of pavement system and empirical knowledge.

Chapter 6

Implementation

In Chapter 5, a backcalculation scheme is proposed and verified with synthetic data generated based on the EM model introduced in Chapter 4. The results show that the scheme works well for interpreting the parameters of pavement system. However, the backcalculation scheme is useful only when it satisfies the field data from GPR survey as well. In fact, in dealing with the field data, there are several elements other than the algorithm which play important roles. Therefore, in order to guarantee the success of the interpretation of the layer properties, a standard procedure is provided in this Chapter.

6.1 FRF patterns

It is pointed out that in a constant-parameter linear system, the frequency response function (FRF) is preserved, which means the FRF is purely determined by the system parameters. Given the same parameters, the FRF of the EM model is the same as the FRF of the field data, even though the EM model may have slight differences with the actual source from the GPR antenna. Because of this important property, the EM model provides a very good representation of the field data.

Calculation of FRF

In the EM model, the electromagnetic field is generated by a dipole antenna, the smallest component of any GPR antenna. Therefore, the FRF from EM model can be computed by its response $\mathcal{E}(t)$ and the presumed dipole source $\mathcal{I}(t)$. In what follows, consider two kinds of GPR surveys, with/without metal plate on the surface, where the survey with metal plate is a calibration procedure for conventional travel-time technique. Therefore, two FRFs characterizing both surveys can be obtained separately via

$$\mathrm{FRF}_m(f) = \frac{\mathcal{E}_m(f)}{\mathcal{I}(f)}, \quad \mathrm{FRF}_p(f) = \frac{\mathcal{E}_p(f)}{\mathcal{I}(f)} \tag{6.1}$$

where $\mathcal{E}(f)$ and $\mathcal{I}(f)$ are the Fourier transform of $\mathcal{E}(t)$ and $\mathcal{I}(t)$. The subscript "m" and "p" represent the metal plate calibration system and the pavement system, respectively. It is worth noting that these two different systems have the same input source $\mathcal{I}$.

On the other hand, the FRFs can be calculated from the field data $E(t)$ and the current source $I(t)$ of GPR antenna as well, where the FRFs for the metal calibration system and the pavement system can be computed in a similar fashion via

$$\mathrm{FRF}_m(f) = \frac{E_m(f)}{I(f)}, \quad \mathrm{FRF}_p(f) = \frac{E_p(f)}{I(f)} \tag{6.2}$$

where $E(f)$ and $I(f)$ are the Fourier transforms of $E(t)$ and $I(t)$. Since the FRF is preserved, given the same parameters, the FRFs in (6.1) and (6.2) are the same.

The reason to compute these two kinds of FRFs is the following. Due to the design of the GPR equipment, not only the desired pulse is contained in the collected GPR record, but also the unwanted pulse from the feed point. Figure. 6.1 shows a GPR data scan collected from the pavement, where T_p is the positive peak of the reflection from the surface; T_d is the negative peak of the direct arrival; the unwanted pulse from the feed point is overlapped with the direct arrival, as shown before the broken line. Therefore, the true direct arrival is impossible

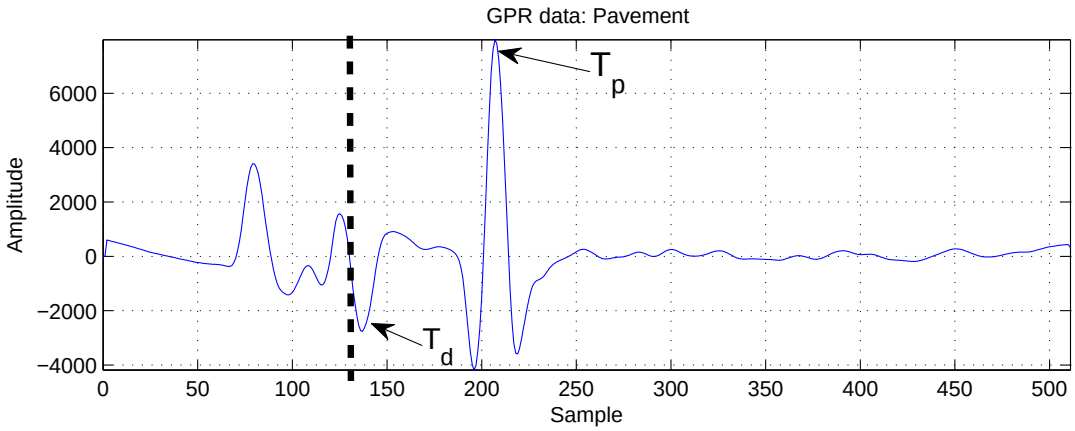

Figure 6.1: The overlap of the signal from the feed point

to recover from a single scan. However, the ideal full-waveform should contain both the direct arrival and the reflection(s) from the layer interface(s), which can be reconstructed from the synthetic data. It is meaningless to compare two full-waveforms where one has direct arrival and the other one does not.

As a compromise, one may consider the subtraction of two different waveforms in which the direct arrival is removed. Since none of the EM waves can pass through the metal plate, the metal calibration can be interpreted as a pavement survey with no layers underneath. Prompted by the fact that the GPR survey from the metal calibration and the pavement are obtained from an identical equipment setup, the unwanted pulse as well as the ambient noise should be largely eliminated upon subtracting from each other. Therefore, the remainder

represents the difference between a layered pavement and a pavement without layers. With the aid of (6.2), one can show that

$$\mathrm{FRF}_p(f) - \mathrm{FRF}_m(f) = \frac{E_p(f) - E_m(f)}{I(f)} = \frac{\Delta E(f)}{I(f)}. \tag{6.3}$$

In this way, it provides a valuable comparison between the survey and synthetic data, and greatly reduces the effect of the noise as well.

6.2 Assumptions

With the aid of Eq. (6.3), it is easy to compute the residual FRFs for synthetic data, but not for the survey data. Although the $\Delta E(f)$ on the right side of Eq. (6.3) can be computed from the Fourier transform of the residual waveform from the survey data, the current I for the GPR antenna is unknown. Only a coarse estimation of I can be made at this point by assuming different kinds of pulse functions such as Gaussian pulse, raised cosine and Mexican-hat shape. By simulating the waveforms created by those pulses, one can compare the reflections between the simulation and GPR survey. The data from metal calibration is chosen here because i) the reflection is stronger for better comparison, and ii) it is a known condition which can be simulated by the EM model. Then, the reflection pulse which is closely matched in terms of the amplitude and shape indicates that its source pulse is the most similar one to the real current source.

As a result, the matched source pulse is the Mexican-hat shape pulse as shown in Fig. 6.2, and it will be applied in the following procedures. It should be noted that there is no guarantee about the presumed source which may lower the accuracy of the interpretation.

Besides the assumption for the current source, it is found that the height of the effective time-zero of the antenna cannot be determined by the given spacing information of the GPR box. In the manual of the model 4108 antenna, the calculation for the reflection from surface is given as

$$(T_p - T_d + T_c)V = 2\sqrt{h^2 + x^2} \tag{6.4}$$

where T_p and T_d are shown in Fig. 6.1 and

- T_c = time constant that corrects for the difference in the arrival time of the positive peak of the direct-coupling and the true time-zero (This value was back-calculated using the same equation and a series of measurements over a metal plate obtained at known heights);
- T_p = time corresponding to positive peak of pavement surface reflection arrival;
- T_d = time corresponding to negative peak of direct-coupling arrival;
- V = propagation velocity of radar waves in free space;
- h = antenna height above pavement or metal plate;

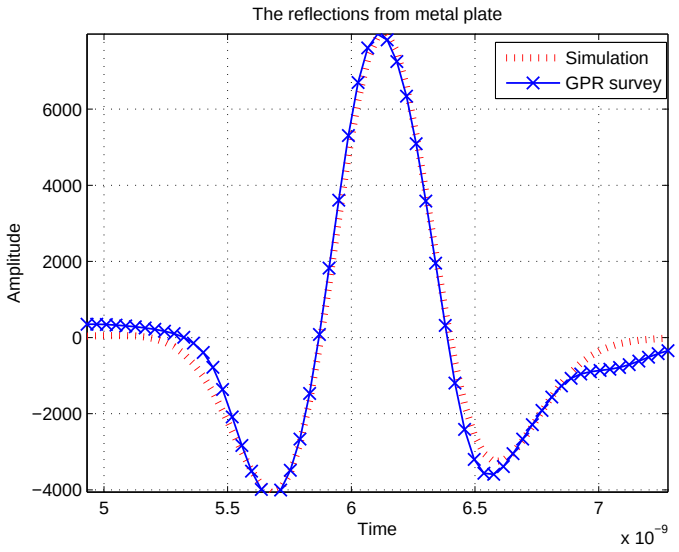

Figure 6.2: Comparison of reflection between simulation and GPR survey

- $x = 1/2$ bistatic separation between transmitting and receiving antennas (for model 4108, $2x = 13.189$ in.).

The question comes up at this point is whether the T_c can be determined by the given parameters, i.e., h and x, or vice versa. Unfortunately, the value of T_c is also unrevealed by the manufacturer. From the setup, the GPR box is generally lifted up at $18 \sim 20$ in. above the ground. In addition, the vertical spacing inside the GPR box is 15.5 in., resulting in a $h = 33.5 \sim 35.5$ in. A simple verification can be done based on the GPR survey as shown in Fig. 6.3 where $T_p = 8.1$ ns and $T_d = 5.36$ ns. If one assumes that the T_c is determined by

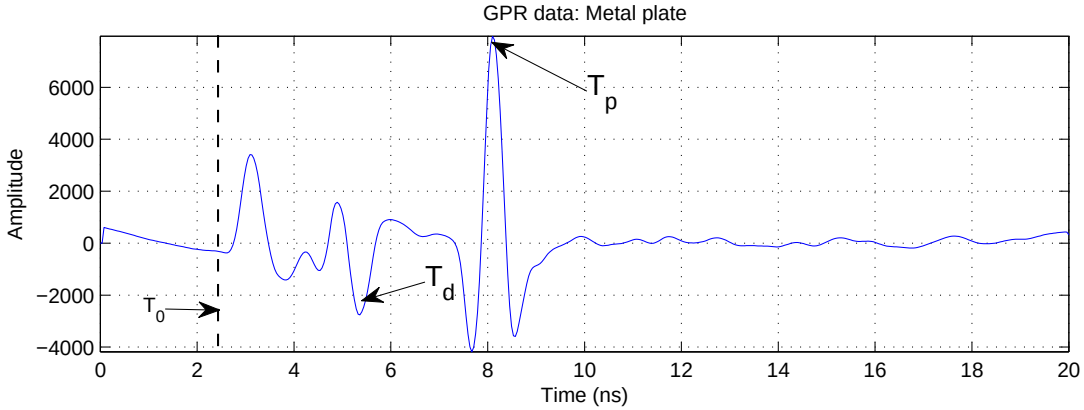

Figure 6.3: GPR survey of metal plate

h and x, when $h = 33.5$ in. and $2x = 13.189$ in., the T_c ends up to be 3.04 ns, which means

the effective time-zero is at $t = 2.32$ ns (T_0 in Fig. 6.3). It seems not possible since T_0 is even before the unwanted pulse from the feed point.

On the other hand, one can assume that the constant T_c determines h and x. With the aid of T_c, it permits the real-time calculation of the GPR antenna height above the ground during the survey. However, it requires a series of experiments based on Eq. (6.4) to determine the constant T_c. In addition, because the type of the current source also affects the value of T_c, the difficulty to determine T_c is increased due to the uncertainty of the source. To overcome this issue, one may skip T_c to directly determine the height of effective time-zero by comparing the data between the simulation and survey as before.

6.3 Implementation procedures

As stated earlier, the FRF pattern characterizing a linear system is determined by the system parameters. A back-analysis scheme based on artificial neural network (ANN) is employed to interpret the parameters of pavement properties from the FRF patterns. By means of (6.3), the neural network is trained with the residual FRF calculated from the EM model. Afterward, the $\Delta E(f)/I(f)$ calculated from the survey data is interpreted by the trained network to produce the pavement properties, by using the asphalt layer dielectric constant ε_A, the asphalt layer thickness h_A and the base layer dielectric constant ε_B.

Collection of field data

The SIR20 is the unit operated by Mn/DOT to collect GPR data. The settings for the parameters are shown in Fig. 6.4(a). As shown, the recommended configuration type for highway scan is "HIGHWAY". Upon choosing this scan type, the pre-set values of samples/scan = 512, scan/sec = 153. The other values can be input depending on the situation such as the DieConstant, scan/ft, and ft/mark. It should be denoted that the default range value of the window is 20 ns for highway configuration. The values of samples/scan and range determine the time interval between the data points. For example, a 512 samples/scan with a range of 20 ns, the samples are collected at rate of 20ns/511 = 0.03911 ns/sample.

Before collecting data, the provided IIR filters have to be turned off in order to obtain the true amplitude of the radar response. In addition, there has to be only one gain point (see Fig. 6.4(b)), i.e., uniform gain throughout the scan. The uniformity of gain value is important in terms of comparing the amplitude with different sections of the scans. Otherwise, it is meaningless to compare normal waveform with distorted one.

Because the height of the source is a fixed parameter during the backcalculation, the effective height of the GPR antenna has to equal the assumed height for simulation. It is not possible to calculate the effective height in real-time at the time being. The only way to locate the effective height is to manually match the simulation with the metal calibration. Due to the fluctuation when moving, however, the pavement survey is valid only when the GPR antenna is lifted up to the same elevation of the calibration height.

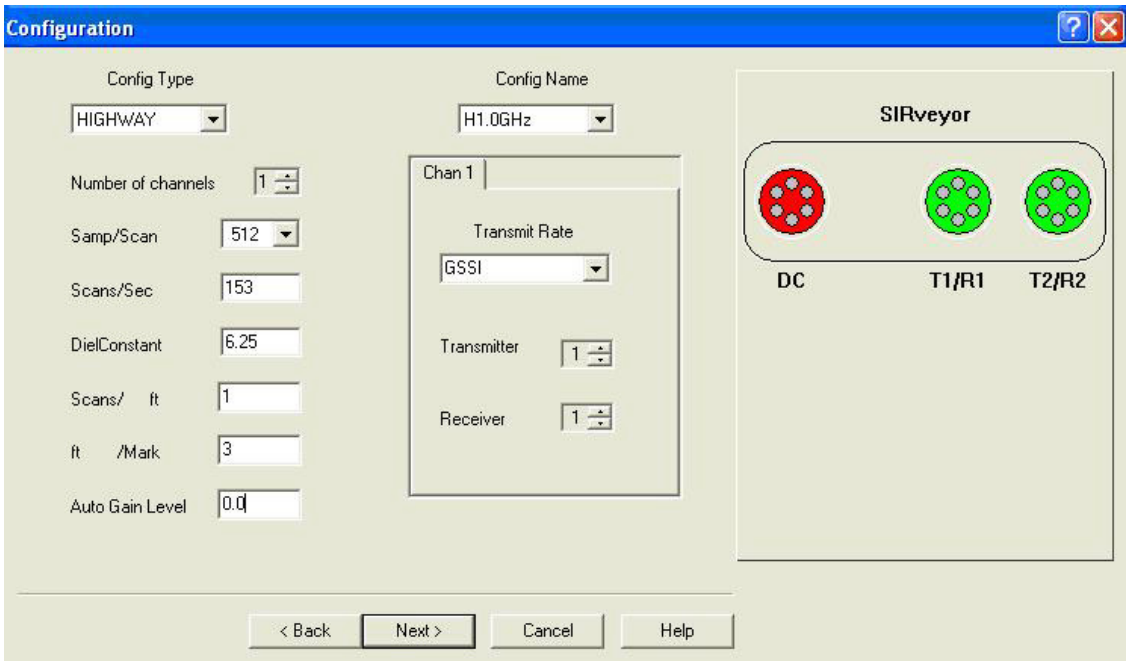

(a) Config Type: Highway, Samples/Scan=512, Auto Gain Level=0

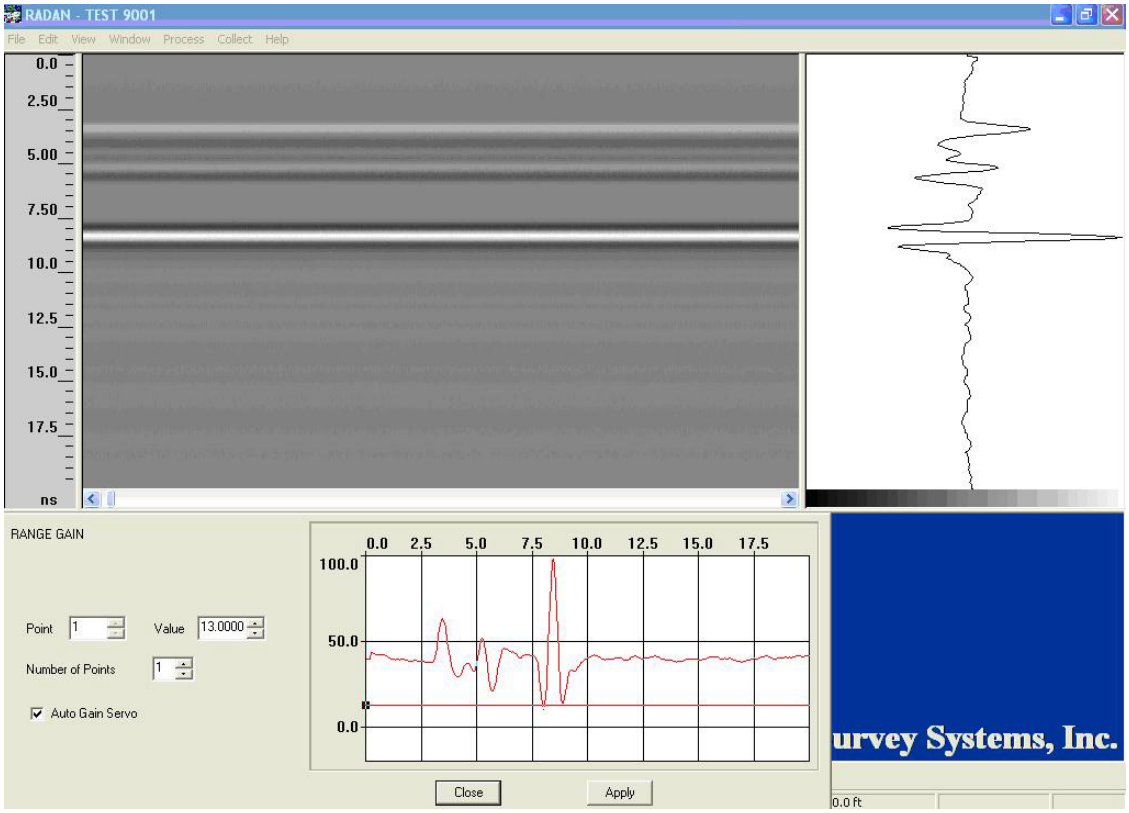

(b) Number of Points=1, Auto Gain Servo(on)

Figure 6.4: Two steps to setup project

To facilitate the implementation of this method, a graphic user interface is designed for convenient operation, called "GopherGPR" as shown in Fig. 6.5.

With the aid of this panel, it allows quickly process of the GPR data from the road survey. The manual for the software is provided in the Appendix C.

6.4 Summary

Based on the limitations of the existing system, there are some modifications of the implementation procedure proposed in this chapter compared to the backcalculation scheme in Chapter 5.

Since the direct arrival is immersed into the response from the feed point, it is impossible to recover the ideal scan from the regular GPR survey. Therefore, the idea to subtract the metal calibration from the regular GPR survey is accommodated here, which provides a valuable comparison between the survey data and simulation and reduces the signal/noise ratio as well.

Since some inside information about the existing system is unavailable, two major assumptions have to be pointed out during the proposed implementation procedure that 1) the Mexican-hat pulse is applied as the excitation source for GPR antenna, and 2) the effective height of the GPR survey is obtained via manually comparison between the metal calibrations from the survey and simulation. Due to the limited time of this project, it is not possible to verify these two assumptions with all situations.

Last but not least, given new valid effective height, the network has to be re-trained since the height is a fixed parameter in training the neural network.

In terms of the interpreted parameters, the accuracy of all the values are dependent upon the accuracy of the effective height. In addition, the value of the base layer dielectric constant would be less reliable than the other two, i.e., the thickness and dielectric constant of the asphalt layer. The reason may be explained by the following:

- The top layer dielectric constant is subjected to the correct value of the height of the source. One may imagine two surface reflections with same amplitude. The one with smaller antenna height means less dissipation of energy, resulting in a smaller interpreted value of the top layer dielectric constant. Vise versa, the larger height would be interpreted as a larger value of the dielectric constant in the top layer.

- It is obvious that the thickness measurement depends on the layer velocity and time mark in the scan at the top and bottom of the layer, where the layer velocity is a function of the layer dielectric constant. Due to the previous reason, the dielectric constant is affected by the accuracy of the source height, as well as the layer velocity, the layer thickness is subjected to the correct value of the height.

- For the base layer, the situation is worse because the errors from the misinterpretation of the parameters in the layer above will be added to the total error in this layer.

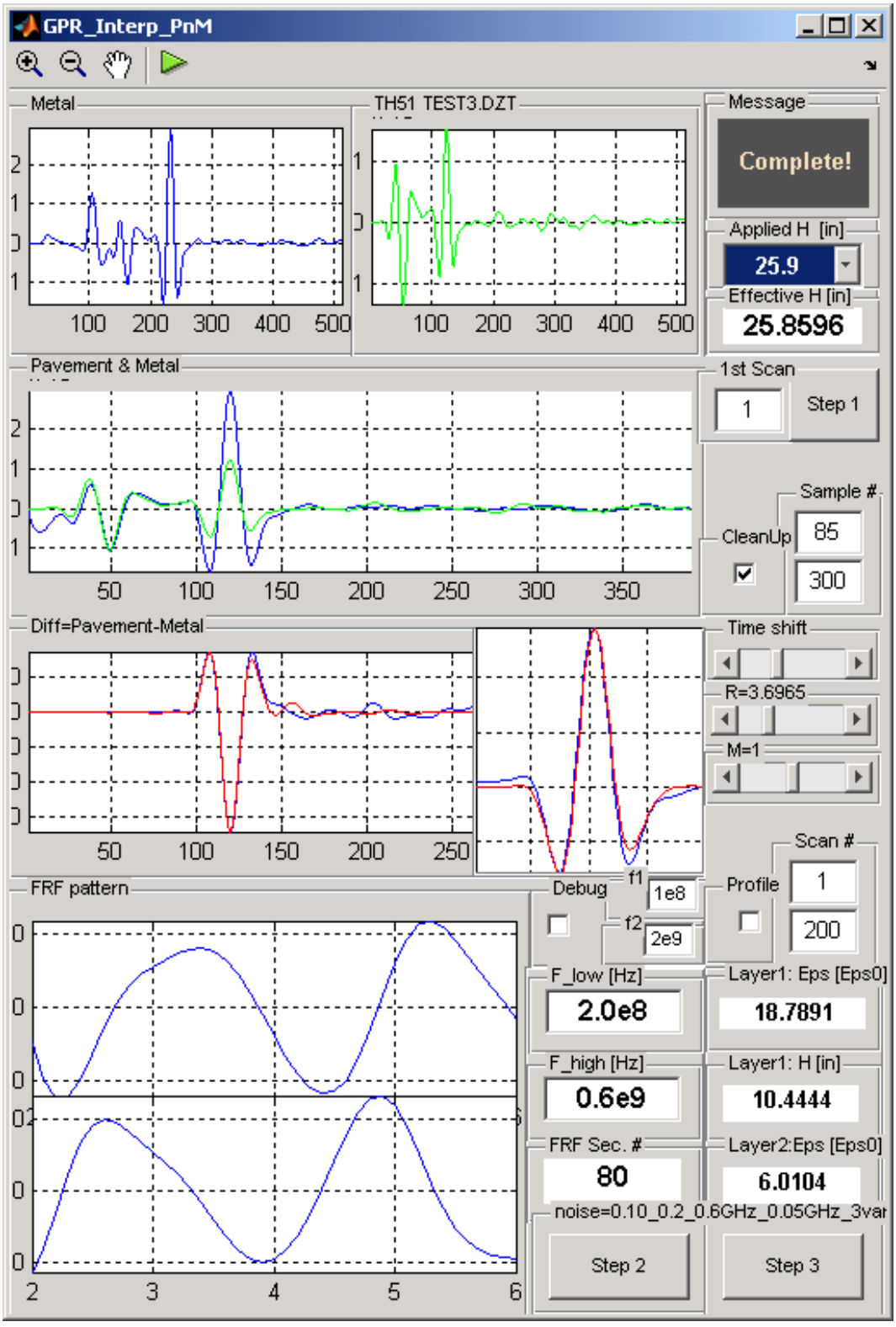

Figure 6.5: GopherGPR panel

However, all these can be improved as long as the effective height can be obtained as accurate as possible.

Chapter 7

Summary

The GPR methodology is similar to shallow seismic reflection surveys in the sense that both techniques use energy reflected from (subsurface) material interfaces. Employing this analogy, the existing GPR data analysis can be enhanced by drawing from the extensive body of literature and experience in shallow seismic reflection. This research aims to generalize and improve upon the related development. In particular, a new algorithm based on electromagnetic wave propagation in layered (as opposed to single, AC-layer) pavement system has been developed, which could be used as a realistic basis for the interpretation of GPR measurement taken on a pavement profile.

Drawing from the invaluable solutions of the EM model in layered system, more accurate interpretation of GPR images in terms of dielectric constant and thickness in different layers can be obtained via the backcalculation scheme based on artificial neural network (ANN) and frequency response function (FRF). The proposed backcalculation scheme is verified with synthetic data where the results show that the scheme works well in interpreting the parameters of pavement system. However, it should be noted that different layer structures require different setup for the scheme. Otherwise, it is out of the capability of what the backcalculation can do.

In addition, it is found that the accuracy of the interpreted pavement parameters are greatly affected by the effective height of the source, which can only be determined by manually comparing the survey scan and simulation at the time being. In this project, the effective height of the illustration sample has been determined and only applicable to the sample metal calibration. Given a new metal calibration, the effective height needs to be manually determined again.

In the end, the research results would help districts and local governments to perform continuous evaluation of the pavement thickness and density quickly and more accurately. In turn, this benefit will inherently increase construction efficiency and the reduce cost of pavement construction and maintenance.

References

[1] C. L. Barnes and J.-F. Trottier, "Ground penetrating radar as a network level management tool for concrete bridge deck repairs," *Canadian Society for Civil Engineering*, p. 236, 2000.

[2] I. L. Al-Qadi and S. Lahouar, "Detection of asphalt binder aging in flexible pavement by ground penetrating radar," *Materials Evaluation*, vol. 63, no. 9, pp. 921–5, September, 2004.

[3] A. Giannopoulos, P. Macintyre, S. Rodgers, and M. C. Forde, "GPR detection of voids in post-tensioned concrete bridge beams," *Proceedings of SPIE - The International Society for Optical Engineering*, vol. 4758, pp. 376–81, 2002.

[4] J. A. Huisman, S. S. Hubbard, J. D. Redman, and A. P. Annan, "Measuring soil water content with ground penetrating radar: A review," *Vadose Zone Journal*, vol. 2, pp. 476–91, 2003.

[5] T. W. Kennedy, F. L. Roberts, and K. W. Lee, "Evaluation of moisture effects on asphalt concrete mixtures," *Transportation Research Record*, pp. 134–43, 1983.

[6] C. Lenngren, J. Bergstrom, and B. Ersson, "Using ground penetrating radar for assessing highway pavement thickness," in *Subsurface Sensing Technologies and Applications II*, vol. 4129. San Diego, CA, USA: Society of Photo-Optical Instrumentation Engineers, Bellingham, WA, USA, Jul 31-Aug 3 2000 2000, pp. 474–83.

[7] I. A. Lunt, S. S. Hubbard, and Y. Rubin, "Soil moisture content estimation using ground-penetrating radar reflection data," *Journal of Hydrology*, vol. 307, no. 1-4, pp. 254–69, Jun., 2005.

[8] A. Martinez and A. P. Byrnes, "Modeling dielectric-constant values of geologic materials: An aid to ground-penetrating radar data collection and interpretation," *Bulletin of the Kansas Geological Survey 247(1), 16*, 2001.

[9] J. McRobert and G. Foley, "Impacts of waterlogging and salinity on road assets: A western australian case study," ARRB Transport Research Ltd., Australia, Tech. Rep., 1999.

[10] R. M. Morey, *Ground penetrating radar for evaluating subsurface conditions for transportation facilities*. Washington, D.C. : National Academy Press, 1998, vol. 255.

[11] T. Saarenketo and T. Scullion, "Road evaluation with ground penetrating radar," *Journal of Applied Geophysics*, vol. 43, no. 2-4, pp. 119–138, 2000.

[12] T. Scullion and T. Saarenketo, "Integrating ground penetrating radar and falling weight deflectometer technologies in pavement evaluation," *ASTM Special Technical Publication*, vol. 1375, pp. 23–37, 1999.

[13] A. H. Sihvola, "Self-consistency aspects of dielectric mixing theories," *IEEE Transactions on Geoscience and Remote Sensing*, vol. 27, no. 4, pp. 403–15, July 1989.

[14] G. C. Topp, J. L. Davis, and A. P. Annan, "Electromagnetic determination of soil water content: measurements in coaxial transmission lines," *Water Resources Research*, vol. 16, no. 3, pp. 574–82, June 1980.

[15] J. Birchak, C. Gardner, J. Hipp, and J. Victor, "High dielectric constant microwave probes for sensing soil moisture," *Proceedings of the IEEE*, vol. 62, no. 1, pp. 93 – 8, Jan. 1974.

[16] W. F. Brown, *Dielectrics, in Encyclopedia of Physics*. New York: Springer-Verlag, 1956, vol. 17, pp. 1–154.

[17] J. L. Davis and A. P. Annan, "Ground-penetrating radar for high-resolution mapping of soil and rock stratigraphy," *Geophysical Prospecting*, vol. 37, no. n, pp. 531–51, July 1989.

[18] K. Roth, R. Schulin, H. Fluhler, and W. Attinger, "Calibration of time domain reflectometry for water content measurement using a composite dielectric approach," *Water Resources Research*, vol. 26, no. 10, pp. 2267–73, Oct. 1990.

[19] E. J. Jaselskis, J. Grigas, and A. Brilingas, "Dielectric properties of asphalt pavement," *Journal of Materials in Civil Engineering*, vol. 15, no. 5, pp. 427–34, September/October, 2003.

[20] J. Swenson, B. Guzina, J. Labuz, and A. Drescher, "Moisture effects on pvd and dcp measurement," Minnesota Department of Transportation, Research Services Section, Minneapolis, MN, Tech. Rep., June 2006.

[21] P. Davich, J. F. Labuz, B. Guzina, and A. Drescher, "Small strain and resilient modulus testing of granular soils," Minnesota Department of Transportation, Research Services Section, Minneapolis, MN, Tech. Rep., Aug 2004.

[22] H. Adei, "Neural networks in civil engineering: 1989-2000," *Computer-Aided Civil and Infrastructure Engineering*, vol. 16, no. 2, pp. 126–42, Mar. 2001.

[23] T. Akhlaghi, "Application of artificial neural networks in non-destructive testing of layered structures using the surface wave method," *Insight: Non-Destructive Testing and Condition Monitoring*, vol. 49, no. 8, pp. 465–70, Aug. 2007.

[24] W. Cai and T. Yu, "Fast calculations of dyadic green's functions for electromagnetic scattering in a multilayered medium," *Journal of Computational Physics*, vol. 165, no. 1, pp. 1–21, Nov. 2000.

[25] T. J. Cui and W. C. Chew, "Fast evaluation of sommerfeld integrals for em scattering and radiation by three-dimensional buried objects," *IEEE Transactions on Geoscience and Remote Sensing*, vol. 37, no. 2, pp. 887–900, 1999.

[26] Z. Ergül and L. Gürel, "Hybrid cfie-efie solution of composite geometries with coexisting open and closed surfaces," *2005 IEEE Antennas and Propagation Society International Symposium*, vol. 4B, pp. 289–92, 2005.

[27] K. R. Maser and T. Scullion, "Automated pavement subsurface profiling using radar: Case studies of four experimental field sites," *Transportation Research Record*, no. 1344, pp. 148–54, 1992.

[28] K. A. Michalski and J. R. Mosig, "Multilayered media green's functions in integral equation formulations," *IEEE Transactions on Antennas and Propagation*, vol. 45, no. 3, pp. 508–519, March 1997.

[29] L. Tsang, C.-J. Ong, C.-C. Huang, and V. Jandhyala, "Evaluation of the green's function for the mixed potential integral equation (mpie) method in the time domain for layered media," *EEE Transactions on Antennas and Propagation*, vol. 51, no. 7, pp. 1559–1571, 2003.

[30] D. A. Willett, K. C. Mahboub, and B. Rister, "Accuracy of ground-penetrating radar for pavement-layer thickness analysis," *Journal of Transportation Engineering*, vol. 132, no. 1, pp. 96–103, January, 2006.

[31] T. Yu and W. Cai, "Fifa - fast interpolation and filtering algorithm for calculating dyadic green's function in the electromagnetic scattering of multi-layered structures," *Communications in computational physics*, vol. 1, no. 2, pp. 229–260, April, 2006.

[32] R. Y. S. Pak and B. B. Guzina, "Three-dimensional green's functions for a multilayered half-space in displacement potentials," *Journal of Engineering Mechanics*, vol. 128, no. 4, pp. 449–61, April, 2002.

[33] T. Saarenketo and T. Scullion, "Ground penetrating radar applications on roads and highways," *Research Rep.*, no. 1923-2F, pp. Texas Transportation Institute, College Station, Tex., 1994.

[34] E. Rmeili and T. Scullion, "Detecting stripping in asphalt concrete layers using ground penetrating radar," *Transportation Research Record*, Jan. 1997.

[35] S. Lahouar, I. L. Al-Qadi, A. Loulizi, M. T. Clark, and D. T. Lee, "Approach to determining in situ dielectric constant of pavements: Development and implementation at interstate 81 in virginia," *Transportation Research Record*, no. 1806, pp. 81–7, 2002.

[36] D. Edward and P. Billington, "Gpr surveys to help determine condition of a concrete bridge deck," *Geophysics Conference*, 2003.

[37] I. L. Al-Qadi and S. Lahouar, "Detection of asphalt binder aging in flexible pavement by ground penetrating radar," *Materials Evaluation*, vol. 63, no. 9, pp. 921–5, September, 2005.

[38] I. Flood and N. Kartam, "Neural networks in civil engineering. i: Principles and understanding," *Journal of Computing in Civil Engineering*, vol. 8, no. 2, pp. 131–48, Apr. 1994.

[39] B. A. Goktepe, E. Agar, and L. A. Hilmi, "Role of learning algorithm in neural network-based backcalculation of flexible pavements," *Journal of Computing in Civil Engineering*, vol. 20, no. 5, pp. 370–373, 2006.

[40] N. Rakesh, A. K. Jain, M. A. Reddy, and K. S. Reddy, "Artificial neural networks - genetic algorithm based model for backcalculation of pavement layer moduli," *International Journal of Pavement Engineering*, vol. 7, no. 3, pp. 221–30, Jan. 2006.

[41] M. Saltan and S. Terzi, "Backcalculation of pavement layer parameters using artificial neural networks," *Indian Journal of Engineering and Materials Sciences*, vol. 11, no. 1, pp. 38–42, Feb. 2004.

[42] M. Saltan, M. Tigemir, and M. Karasahin, "Artificial neural network application for flexible pavement thickness modeling," *Turkish Journal of Engineering and Environmental Sciences*, vol. 26, no. 3, pp. 243–8, 2002.

[43] R. Rojas, *Neural Networks A Systematic Introduction.* Berlin ; New York, Springer-Verlag, 1996.

[44] *MATLAB User Manual for Neural Network Toolbox V5.1 (R2007b).* The MathWorks, Sep. 2007.

[45] T. Westover and B. Guzina, *Engineering framework for the self-consistent analysis of FWD data.* Washington, D.C. : Transportation Research Board, 2007, vol. 2005/2007.

[46] H. Ceylan, A. Guclu, E. Tutumluer, and M. R. Thompson, "Backcalculation of full-depth asphalt pavement layer moduli considering nonlinear stress-dependent subgrade behavior," *International Journal of Pavement Engineering*, vol. 6, no. 3, pp. 171–182, Sep. 2005.

[47] S. Caorsi and G. Cevini, "Neural networks trained by scattered electromagnetic data for gpr applications," *Proceedings of the 2nd International Workshop on Advanced Ground Penetrating Radar (IEEE Cat. No.03EX680), Delft, Netherlands*, pp. 228–33, 2003.

[48] D. Cao, "Delination of subgrade soils from falling weight deflectometer measurements," *M.S. Thesis, University of Minnesota, Minneapolis, MN*, Nov. 2001.

[49] J. Bendat and A. Piersol, *Random Data: Analysis and Measurement Procedures*. New York, NY: Wiley-Interscience, 1971.

[50] J. B. Marion and M. A. Heald, *Classical Electromagnetic Radiation*. Academic Press, New York and London, 1980.

Appendix A
Data Set of Field Sample

Table A-1: Data from the MnDOT

Lab ID	Air Dry	Dry	SSD	Imm.	VWC	G_{mb}	G_{mm}	$\%G_{mm}$	ε
1503	1019.1	1017.6	1020.1	598	0.25	2.411	2.51	96.0	4.9
1504	1090.1	1017.6	1020.1	598	0.25	2.411	2.51	96.0	4.9
1505	956.2	954.9	957.4	553	0.26	2.361	2.512	94.0	5
1506	779.2	777.7	780.4	446.4	0.35	2.328	2.52	92.4	4.8
1507	979.4	976.5	980.2	572.6	0.38	2.396	2.511	95.4	5.2
1508	977.3	976	978	563.4	0.20	2.354	2.457	95.8	4.7
1509	847.8	841.2	848.4	481.7	0.86	2.294	2.494	92.0	5.3
1510	947.2	944.6	947.8	540.6	0.34	2.320	2.494	93.0	5.2
1511	885.1	884.1	886.1	507.6	0.23	2.336	2.494	93.7	5.3
1512	1752	1743.2	1754	1014.7	0.62	2.358	2.497	94.4	5.5
1513	903.7	896.2	905.4	510	1.03	2.267	2.494	90.9	4.8
1523	1608.5	1607	1609.6	935.1	0.16	2.383	2.468	96.5	4.4
1524	1002.9	1002.1	1003.6	584.5	0.15	2.391	2.482	96.3	5.3
1525	574.2	573.4	574.8	332	0.24	2.362	2.482	95.1	4.9
1526	890.1	887.5	890.9	511.1	0.38	2.337	2.496	93.6	4.3
1527	678.8	676.8	679.1	392.3	0.34	2.360	2.496	94.5	3.5
1528	646.2	645.1	647.2	374.2	0.33	2.363	2.496	94.7	4.4
1529	703.9	701	705	403.7	0.57	2.327	2.496	93.2	4.2
1530	1141.9	1139.7	1142.6	657.3	0.25	2.348	2.477	94.8	4.2
1531	1164.9	1162.2	1166.6	672.8	0.38	2.354	2.477	95.0	5
1532	1196.4	1195	1197.7	698.4	0.23	2.393	2.477	96.6	4.2
1533	1097.9	1096.2	1098.6	638.6	0.22	2.383	2.477	96.2	4.9
1534	1116.3	1114.7	1117.8	648.7	0.28	2.376	2.477	95.9	5.2
1535	1133.9	1131.3	1135.7	646.6	0.39	2.313	2.488	93.0	4.9
1536	635.6	629.3	636.4	356.6	1.13	2.249	2.518	89.3	4.6
1537	941.1	933	942.6	543.8	1.03	2.340			5.4
1538	993	926.1	935	533	0.96	2.304			5.1
1539	1073.6	1064	1075.6	613.1	1.09	2.301			4.9
1540	739.3	736.9	739.9	409.7	0.41	2.232			4.7
1541	906	901	907.3	507.5	0.70	2.254			4.8
1542	743.1	738.6	746.6	403.4	1.08	2.152			4.7
1543	658.1	654.9	660.3	362.6	0.82	2.200			4.3
1544	1475.5	1473.6	1476.6	857.8	0.20	2.381	2.472	96.3	5.2
1545	1150.1	1149	1151.2	668.5	0.19	2.380	2.472	96.3	5.2

Table. A-1 Data from MnDOT (cont.)

Lab ID	Air Dry	Dry	SSD	Imm.	VWC	G_{mb}	G_{mm}	$\%G_{mm}$	ε
1546	1123.1	1122.2	1123.7	657.3	0.13	2.406	2.472	97.3	5
1547	766.2	762.4	767.6	437.6	0.68	2.310	2.512	92.0	5
1548	744.5	741.4	746.2	425	0.65	2.308	2.512	91.9	5.1
1549	825.9	825.7	826.8	481.4	0.13	2.391	2.498	95.7	4.2
1550	858	854.3	859.1	485.7	0.56	2.288	2.498	91.6	4.6
1551	854	850.9	856	489.5	0.60	2.322	2.498	92.9	4.7
1552	882.3	876.2	887.4	503.6	1.28	2.283	2.498	91.4	4.6
1553	1212.3	1201.7	1214.1	684	1.03	2.267	2.267	100.0	5.6
1554	1412.7	1400.5	1415	799.1	1.04	2.274			5.3
1557	970.2	969.4	970.9	573.1	0.15	2.437	2.558	95.3	5.3
1558	1213.2	1208.8	1214.5	711.2	0.47	2.402	2.558	93.9	5.9
1559	1013.2	1007	1014.7	586.4	0.76	2.351	2.558	91.9	6.2
1560	1115	1102.8	1116.7	638.2	1.26	2.305	2.558	90.1	6.2
1561	722.5	714.5	724.4	408.1	1.39	2.259	2.563	88.1	6.4
1562	1183.7	973.3	986.7	561	1.38	2.286	2.563	89.2	5.7
1563	976.5	972.4	978.1	565.6	0.59	2.357	2.563	92.0	6.1
1564	989.2	978.8	992.3	566.3	1.38	2.298	2.563	89.6	6.5
1565	867.8	866.7	869.3	492	0.30	2.297	2.522	91.1	5.05
1566	761.7	760.9	763	437.7	0.28	2.339	2.522	92.7	5.4
1567	854.3	852.7	855.9	484.2	0.38	2.294	2.522	91.0	5.09
1568	1021.5	1020.9	1022.4	596.6	0.15	2.398	2.492	96.2	5.03
1569	998.1	997.8	999.4	582.1	0.16	2.391	2.488	96.1	5.34
1570	1847.8	1840.8	1849.4	1056.1	0.47	2.320	2.494	93.0	5
1571	1598.1	1586.5	1603.9	893	1.10	2.232	2.498	89.3	4.5
1572	692.9	690.4	694.1	396.5	0.54	2.320	2.535	91.5	5.22
1573	934.1	928.2	937	531.3	0.95	2.288	2.535	90.3	5.6
1574	631.7	627.6	634.2	358.5	1.05	2.276	2.537	89.7	5.27
1575	687.7	681.2	692.5	381.9	1.66	2.193	2.537	86.4	4.6
1576	885.6	879.9	886.8	502	0.78	2.287	2.514	91.0	5.22
1577	793.5	790.4	794.9	452.5	0.57	2.308	2.514	91.8	5.48
1578	608.1	605.2	609.5	346.8	0.71	2.304	2.514	91.6	5.48
1579	915.5	914.1	918.3	523.9	0.46	2.318	2.53	91.6	5.21
1580	766.7	765.2	769.2	437.2	0.52	2.305	2.53	91.1	4.25
1581	770.9	769.7	772.9	442.2	0.42	2.327	2.53	92.0	5.41
1582	986.2	978.4	987.4	565.1	0.92	2.317	2.508	92.4	4.68
1583	1081.9	1069.3	1090.6	607.2	1.99	2.212	2.508	88.2	5.28
1584	932.8	931.4	933.7	533	0.25	2.324			5.2
1585	1042.6	1040.2	1044.4	592.1	0.40	2.300	2.504	91.8	5.23
1586	847.2	845.3	848.3	484.2	0.35	2.322	2.504	92.7	5.45
1587	803.9	801.7	805	460.6	0.41	2.328	2.504	93.0	6.24
1588	952.8	951.4	953.8	550.7	0.25	2.360	2.504	94.3	5.53
1589	822.8	821.9	823.9	477.7	0.24	2.374	2.504	94.8	5.18
1590	935.4	931.8	936.3	533.2	0.48	2.312	2.516	91.9	6.09
1591	879.6	877.6	880.8	514.9	0.36	2.398	2.516	95.3	5.6
1592	1119.2	1117.5	1120.1	652.1	0.23	2.388	2.516	94.9	5.36
1593	895.1	893.4	896.6	516.5	0.36	2.350	2.516	93.4	5.61
1625	1124.4	1120.9	1125.3	653.5	0.39	2.376	2.488	95.5	5.41
1626	1148.7	1144.2	1150.4	659	0.54	2.328	2.512	92.7	4.9
1627	722.8	721.8	724.4	396.4	0.36	2.201	2.506	87.8	3.7
1628	930.6	929.3	932	521.7	0.29	2.265	2.506	90.4	4.89
1629	821.2	820.4	823.4	469.4	0.37	2.318	2.506	92.5	4.83
1630	1205.7	1204.9	1207.5	690.6	0.22	2.331	2.501	93.2	5.51
1632	1001.1	1000	1003.7	561.4	0.37	2.261	2.503	90.3	5.13
1633	1061.5	1059	1065.4	599.2	0.60	2.272	2.503	90.8	5.57
1634	734.9	733.7	736.9	415.4	0.44	2.282	2.498	91.4	5.22
1635	606.8	605.9	608	353.1	0.35	2.377	2.482	95.8	6
1636	731.1	730.1	731.9	419.1	0.25	2.334	2.482	94.0	5.54
1637	734.7	732.8	736	419.9	0.44	2.318	2.482	93.4	5.73

Table. A-1 Data from MnDOT (cont.)

Lab ID	Air Dry	Dry	SSD	Imm.	VWC	G_{mb}	G_{mm}	$\%G_{mm}$	ε
1638	743.3	736.5	745	421.7	1.15	2.278	2.542	89.6	5.62
1639	1180.7	1178.4	1182.1	688.4	0.31	2.387	2.525	94.5	5.42
1640	1403.2	1399.2	1403.9	816.6	0.34	2.382	2.525	94.4	5.41
1641	1270.4	1267.8	1271.7	756.4	0.31	2.460	2.525	97.4	5.5
1642	1004.6	1001.3	1006	586	0.47	2.384	2.525	94.4	5.32
1643	1579.2	1575.4	1580.4	926.4	0.32	2.409	2.484	97.0	5.64
1644	814.4	813.8	815.2	475	0.17	2.392	2.481	96.4	5.78
1645	676.4	672.8	677.3	382.3	0.67	2.281	2.481	91.9	4.92
1646	1425.6	1424.2	1427.9	834.1	0.26	2.398	2.516	95.3	5.86
1647	1437.1	1431.1	1439	822.6	0.55	2.322	2.516	92.3	5.9
1648	1517.4	1515.6	1518.7	887.1	0.20	2.400	2.516	95.4	6.1
1649	979.8	977.2	980.9	570.1	0.38	2.379	2.516	94.5	5.26
1658	1209.5	1205.9	1210	699.1	0.34	2.360			4.6
1659	1532.2	1531.3	1533	888.8	0.11	2.377			5.35
1660	1238.4	1235.3	1239.1	711.7	0.31	2.342			5.6
1661	1244.4	1240.8	1245.6	710.5	0.39	2.319			5.8
1668	895.5	887.7	898	506.2	1.16	2.266			5.67
1669	751.7	743.2	753	428	1.32	2.287			4.62
1670	722.4	715.4	725.1	408.8	1.36	2.262			5.43
1671	553.7	545.5	556.8	309.8	2.07	2.209			4.14
1672	790	778.4	793.8	439.4	1.98	2.196			4.68
1673	878.9	874.7	880	504.1	0.61	2.327			5.06
1674	246.7	244.8	253.2	139.4	3.43	2.151			3.71
1675	979.6	978	981	557.2	0.31	2.308	2.478	93.1	5.74
1676	826.6	825.5	827.8	482.5	0.28	2.391	2.478	96.5	5.48
1677	947.8	945.2	948.5	545.6	0.35	2.346	2.478	94.7	5.59
1678	1175.3	1174	1176.4	680.4	0.20	2.367	2.492	95.0	5.5
1679	842.7	841.2	843.7	481.4	0.30	2.322	2.492	93.2	5.08
1680	1048.8	1046.9	1049.4	607.2	0.24	2.367	2.492	95.0	5.07
1681	979.4	978.1	980.2	570.9	0.21	2.390	2.492	95.9	5.39
1682	1232.7	1225.5	1233.6	705.7	0.66	2.321			5.32
1683	1017.1	1012.8	1017.6	590.1	0.47	2.369			4.53
1684	908.8	905.2	910.3	513.7	0.56	2.282			5.98
1685	966.6	965.2	967.5	573.9	0.24	2.452			5.22
1701	1060.2	1058.7	1061.1	614.8	0.23	2.372	2.496	95.0	5.21
1702	1275.2	1272.4	1276.2	746.6	0.30	2.403	2.498	96.2	5.6
1703	935.7	931.4	936.6	542.5	0.56	2.363	2.482	95.2	5.73
1704	687.7	689.7	688.5	392.7	-0.17	2.332	2.482	93.9	4.92
1705	1213.9	1213.2	1215	709.1	0.15	2.398	2.496	96.1	5.4
1706	1011.4	1010.7	1011.8	594.8	0.11	2.424	2.496	97.1	5
1707	1818.8	1817.7	1819.9	1072	0.12	2.430	2.496	97.4	5.8
1708	810.5	809.9	811.1	470.8	0.15	2.380	2.471	96.3	4.92
1709	1127.5	1126.8	1127.9	659.7	0.10	2.407	2.471	97.4	5.02
1710	843.7	843.2	844.7	483.6	0.18	2.335	2.492	93.7	4.99
1711	950	949.6	952.1	542.2	0.26	2.317	2.496	92.8	4.51
1712	1600.5	1595.4	1601.7	922.8	0.39	2.350	2.501	94.0	4.34
1713	1271	1270.7	1272.4	726	0.13	2.326	2.474	94.0	5.24
1714	887	886.6	889.1	509.1	0.28	2.333	2.471	94.4	5.11

Table A-2: Data from lab asphalt sample

Sample ID	Weight [g]	T [h]	Permittivity 1st [J]	2nd [J]	3rd [J]	Mean [J]	Sqrt [J]	GVC* [%]
	7219.2	Dry	4.3	4.6	4.1	4.3	2.1	-
#3 58-28B	7231.5	0	4.6	4.6	4.5	4.6	2.1	0.17
4%AV Opt L	7230.8	1	4.6	4.6	4.5	4.6	2.1	0.16
	7230.4	2	4.5	4.6	4.4	4.5	2.1	0.16
	7230.6	3	4.4	4.5	4.4	4.4	2.1	0.16
	7236.9	Dry	4.6	4.6	4.5	4.6	2.1	-
#12 58-28B	7243.1	0	4.8	4.7	4.7	4.7	2.2	0.09
4%AV Opt L	7242.3	1	4.7	4.5	4.6	4.6	2.1	0.07
	7242.6	2	4.6	4.5	4.5	4.5	2.1	0.08
	7242.0	3	4.6	4.5	4.6	4.6	2.1	0.07
	7257.2	Dry	3.9	3.6	3.8	3.8	1.9	-
#9 58-28A	7276.6	0	4.0	4.1	4.2	4.1	2.0	0.27
4%AV Opt L	7260.7	1	4.0	4.0	3.9	4.0	2.0	0.05
	7260.6	2	3.9	3.8	3.8	3.8	2.0	0.05
	7260.1	3	4.0	3.9	3.8	3.9	2.0	0.04
	7239.6	Dry	4.3	4.2	4.3	4.3	2.1	-
#4 58-28A	7287.1	0	4.3	4.5	4.5	4.4	2.1	0.66
7%AV Opt L	7284.0	1	4.4	4.4	4.5	4.4	2.1	0.61
	7283.5	2	4.3	4.2	4.4	4.3	2.1	0.61
	7282.2	3	4.3	4.4	4.4	4.4	2.1	0.59
	7164.4	Dry	3.9	3.6	3.8	3.8	1.9	-
#9 58-28A	7172.0	0	4.0	4.1	4.2	4.1	2.0	0.11
4%AV Opt G	7169.8	1	4.0	4.0	3.9	4.0	2.0	0.08
	7169.8	2	3.9	3.8	3.8	3.8	2.0	0.08
	7169.3	3	4.0	3.9	3.8	3.9	2.0	0.07
	7220.7	Dry	3.8	3.8	3.9	3.8	2.0	-
#10 58-28A	7229.4	0	4.1	4.2	4.3	4.2	2.0	0.12
7%AV Opt G	7227.2	1	4.0	4.2	4.3	4.2	2.0	0.09
	7226.8	2	3.8	3.9	3.8	3.8	2.0	0.08
	7226.6	3	3.8	3.9	3.8	3.8	2.0	0.08

*GVC = Gravimatric Water Content
AV = Air voids
Opt = optimum propotion propotion of asphalt binder
L/G = limestone/granite

Table A-3: Data from fine-grained soil : prismatic sample

Container ID	Permittivity						Conductivity					Water Content
	High [J]	Low [J]	Median [J]	Mean [J]	Sqrt [$\sqrt{J}$]	Cov [%]	High [S/cm]	Low [S/cm]	Median [S/cm]	Mean [S/cm]	Cov [%]	[%]
A_15_100	27.2	20.8	24.1	24.0	4.9	13.3	9	0	4	4.0	93.5	15.6
B_24_103	47.2	34.9	40.0	40.8	6.4	14.6	44	8	23	24.4	54.8	23.6
B_19.5_103	42.5	18.7	33.0	31.7	5.6	24.1	108	0	14	21.3	144.4	19.2
B_16_103	30.2	11.2	28.7	26.3	5.1	22.9	44	0	18	20.1	93	17.4
B_27_98	45.4	22.9	32.3	32.2	5.7	23.4	21	0	3	5.6	126.3	26.1
B_22_98	49.4	31.3	40.3	40.3	6.3	14.1	135	0	52	54.4	79.4	22.0
B_16_98	24.0	16.0	20.9	20.1	4.5	14.3	48	18	23	26.6	42.6	16.3
C_12_103	19.3	11.2	17.6	16.4	4.0	16.2	6.4	60	8	28.0	25.9	11.3
C_9.5_103	17.9	14.4	16.4	16.2	4.0	6.4	60	8	28	25.9	67.6	9.4
C_8_103	17.7	10.9	16.2	15.6	3.9	14.1	46	0	13	16.3	96.6	8.4
C_13_98	18.6	10.5	17.2	15.8	4.0	20.6	43	0	0	8.6	223.6	12.4
C_10_98	15.3	13.9	14.7	14.5	3.8	3.7	90	2	61	45.9	69.8	10.1
C_8_98	18.0	15.8	17.1	17.0	4.1	3.8	74	25	49	52.9	28.6	8.4
D_16_103	45.6	35.4	38.2	39.6	6.3	9.3	114	3	57	61.6	59.9	16.3
D_13_103	38.6	30.0	34.4	34.6	5.9	9.4	54	2	21	22.7	69.6	13.3
D_11_103	31.8	23.0	26.1	26.9	5.2	13.1	26	0	7	7.6	108.4	10.6
D_18_98	49.4	28.5	43.4	41.8	6.5	16.7	211	3	16	60.1	142.9	18.6
D_14_98	36.6	21.2	30.0	30.1	5.5	18.7	185	39	96	105.5	44.5	14.2
D_11_98	28.7	17.0	25.5	24.4	4.9	15.5	61	0	28	23.1	92.3	10.7

Table A-4: Data from fine-grained soil : cylinder sample

	Container ID	Permittivity						Conductivity					Water Content
		High [J]	Low [J]	Median [J]	Mean [J]	Sqrt [$\sqrt{J}$]	Cov [%]	High [S/cm]	Low [S/cm]	Median [S/cm]	Mean [S/cm]	Cov [%]	[%]
Spec #1	B_19.5_103	38.9	37.5	38.3	38.2	6.2	1.8	18	4	17	13.0	60.1	18.5
	B_16_103	39.0	37.9	38.3	38.4	6.2	1.4	13	4	5	7.3	67.3	16.5
	B_27_98	42.5	39.7	42.0	41.4	6.4	3.6	90	56	81	75.7	23.3	23.1
	B_22_98	38.0	37.0	37.2	37.4	6.1	1.4	90	56	81	75.7	23.3	21.2
	C_8_98	16.7	15.8	16.3	16.3	4.0	2.8	24	12	23	19.7	33.9	8.4
	D_16_103	34.8	24.1	34.1	31.0	5.6	19.3	26	10	21	19.0	43.1	15.6
	D_13_103	36.1	31.5	35.4	34.6	5.9	6.0	6	0	5	4.0	67.7	13.1
	D_11_103	30.9	29.7	30.1	30.2	5.5	2.0	1	0	1	0.7	86.6	10.5
	D_18_98	38.4	33.1	34.7	35.4	5.9	7.7	81	18	57	52.0	61.1	18.3
	D_14_98	36.4	36.0	36.1	36.2	6.0	0.6	40	11	30	27.0	54.6	14.3
	D_11_98	25.8	20.6	21.3	22.6	4.8	12.5	10	3	6	6.3	55.5	10.7
Spec #2	B_19.5_103	35.4	32.6	33.9	34.0	5.8	3.4	27	0	9	4.5	139.1	18.3
	B_16_103	36.6	35.2	36.2	36.0	6.0	2.0	20	18	19	19.0	5.3	16.4
	B_27_98	38.1	36.4	37.3	37.3	6.1	3.2	106	80	93	93.0	19.8	24.0
	B_22_98	44.0	43.4	43.9	43.8	6.6	0.7	46	36	39	36.0	14.7	21.5
	C_8_98	19.1	18.8	19.0	19.0	4.4	0.8	18	10	14	15.0	28.2	8.2
	D_16_103	31.4	30.1	31.0	30.8	5.5	2.2	10	7	8	8.0	18.3	15.6
	D_13_103	36.1	32.3	34.8	34.4	5.9	4.5	11	0	4	1.0	127.6	13.2
	D_11_103	30.9	30.2	30.7	30.6	5.5	1.2	3	1	2	1.0	69.3	10.6
	D_18_98	35.6	34.4	34.4	34.8	5.9	2.0	21	13	18	21.0	25.2	18.4
	D_14_98	33.3	31.7	32.4	32.5	5.7	2.5	21	13	18	21.0	25.2	13.6
	D_11_98	25.3	24.4	25.0	24.9	5.0	1.8	5	0	3	3.0	94.4	10.7

Table A-5: Data from coarse-grained soil

Test #	Sample		Percometer Results		GWC		VWC
	Density	ID	Dielectric	Conductivity	Target	Measured from Oven	Measured from Oven
	kg/m^3		J	uS/cm			
1	2.158	E	6.75	0.00	2.5	2.55	5.50
2		E	7.15	0.00	2.5	3.35	7.23
3		E	8.67	5.67	5	5.15	11.11
4		E	8.80	6.33	5	5.34	11.52
5		E	9.98	8.67	7.5	7.89	17.03
6		E	8.47	13.67	7.5	7.61	16.42
7	1.839	F	5.34	0.00	3	2.63	4.84
8		F	5.59	0.33	3	2.70	4.97
9		F	7.02	7.67	6	6.24	11.48
10		F	-	-	6	6.10	11.22
11		F	11.80	28.67	9	9.01	16.57
12		F	12.00	40.33	9	10.06	18.50
13	1.9	G	6.61	2.00	3.5	3.23	6.14
14		G	6.54	2.33	3.5	3.44	6.54
15		G	8.02	7.00	6	5.7	10.83
16		G	8.55	11.67	6	6.25	11.88
17		G	10.77	22.67	8.5	8.96	17.02
18		G	8.43	6.67	8.5	7.33	13.93
19	1.725	H	5.78	0.33	3	3.13	5.40
20		H	5.56	1.33	3	3.49	6.02
21		H	7.28	8.00	7	7.44	12.83
22		H	8.17	7.00	7	7.13	12.30
23		H	9.67	6.67	11	11.01	18.99
24		H	11.90	10.00	11	10.64	18.35
25	1.791	I	5.23	2.00	3.5	3.26	5.84
26		I	5.25	2.67	3.5	3.49	6.25
27		I	7.63	5.33	6	6.22	11.14
28		I	7.81	6.00	6	5.93	10.62
29		I	8.84	4.67	8.5	7.88	14.11
30		I	9.20	7.00	8.5	8.56	15.33
31	2.014	J	6.31	0.33	3	3.20	6.44
32		J	5.32	0.67	3	3.12	6.28
33		J	8.39	3.00	5.5	5.50	11.08
34		J	7.91	13.00	5.5	5.45	10.98
35		J	10.26	20.00	8	8.16	16.43
36		J	9.30	24.00	8	7.90	15.91

Appendix B
Electromagnetic Analysis in Layered System

To solve the electromagnetic field in layered structure, the Maxwell's equations for linear material are rewritten here

$$\begin{aligned} \nabla \cdot \mathbf{E} &= \frac{\varrho}{\varepsilon} & \nabla \cdot \mathbf{H} &= 0 \\ \nabla \times \mathbf{E} &= -\mu \frac{\partial \mathbf{H}}{\partial t} & \nabla \times \mathbf{H} &= \mathbf{J} + \varepsilon \frac{\partial \mathbf{E}}{\partial t} \end{aligned} \tag{B-1}$$

where $\mu = \mu_0$ is usually adopt for most non-magnetic materials. By means of time-harmonic representation, $\mathbf{E}(\mathbf{r}, t) = \mathbf{E}(\mathbf{r})e^{-i\omega t}$ and $\mathbf{H}(\mathbf{r}, t) = \mathbf{H}(\mathbf{r})e^{-i\omega t}$, where ω =circular frequency. Hence, the Maxwell's equations are replaced by

$$\begin{aligned} \nabla \cdot \mathbf{E} &= \frac{\varrho}{\varepsilon} & \nabla \cdot \mathbf{H} &= 0 \\ \nabla \times \mathbf{E} &= i\omega\mu\mathbf{H} & \nabla \times \mathbf{H} &= \mathbf{J} - i\omega\varepsilon\mathbf{E} \end{aligned} \tag{B-2}$$

where the time factor $e^{-i\omega t}$ is suppressed. To uncouple the $\mathbf{E}$ and $\mathbf{H}$ fields, upon taking the curl of the third equation in (B-2), and substituting with the fourth equation, one obtains that

$$\nabla \times \nabla \times \mathbf{E} = i\omega\mu(\mathbf{J} - i\omega\varepsilon\mathbf{E}) \tag{B-3}$$

By means of the identity $\nabla \times \nabla \times \mathbf{E} = \nabla(\nabla \cdot \mathbf{E}) - \nabla^2\mathbf{E}$ and the equation of continuity

$$\nabla \cdot \mathbf{J} + \frac{\partial \varrho}{\partial t} = 0, \tag{B-4}$$

Eq. (B-3) is rearranged as Helmholtz equation

$$(\nabla^2 + k^2)\mathbf{E} = -i\omega\mu \left(\bar{\bar{I}} + \frac{\nabla\nabla}{k^2} \right) \cdot \mathbf{J} \tag{B-5}$$

where $k^2 = \omega^2\mu\varepsilon$ is the wave number and $\bar{\bar{I}}$ is unit vector. In what follows, consider a Green's function satisfies

$$(\nabla^2 + k^2)g(\mathbf{r}, \mathbf{r}') = -\delta(\mathbf{r} - \mathbf{r}') \tag{B-6}$$

where the operator ∇ only works on $\mathbf{r}$. It can be shown that the solution of $\mathbf{E}$ takes the form via the Green's function like that

$$\mathbf{E}(\mathbf{r}) = i\omega\mu \int_{V'} g(\mathbf{r}, \mathbf{r}') \left(\bar{\bar{I}} + \frac{\nabla'\nabla'}{k^2} \right) \cdot \mathbf{J}(\mathbf{r}')d\mathbf{r}'. \tag{B-7}$$

It can be verified upon substituting (B-6) and (B-7) into (B-5) where operator ∇ can be put

into the integral like that

$$-i\omega\mu \int_{V'} \delta(\mathbf{r}-\mathbf{r}') \left(\bar{\bar{I}} + \frac{\nabla'\nabla'}{k^2} \right) \mathbf{J}(\mathbf{r}')d\mathbf{r}' = -i\omega\mu \left(\bar{\bar{I}} + \frac{\nabla\nabla}{k^2} \right) \mathbf{J}(\mathbf{r}). \tag{B-8}$$

In the following, by means of the identity $\nabla(gf) = f\nabla g + g\nabla f$ and $\nabla \cdot (g\mathbf{F}) = \nabla g \cdot \mathbf{F} + g\nabla \cdot \mathbf{F}$, one may show that

$$\begin{aligned} g\nabla'\nabla' \cdot \mathbf{J}(\mathbf{r}') &= \nabla' \Big(g\nabla \cdot \mathbf{J}(\mathbf{r}') \Big) - \nabla' g \nabla \cdot \mathbf{J}(\mathbf{r}') \\ &= \nabla' \Big(g\nabla \cdot \mathbf{J}(\mathbf{r}') \Big) - \nabla' \cdot \Big(\nabla' g \cdot \mathbf{J}(\mathbf{r}') \Big) + \mathbf{J}(\mathbf{r}') \cdot \nabla'\nabla' g. \end{aligned} \tag{B-9}$$

In addition, assume that there is neither charge inside the volume ($\varrho = 0$ in V') nor surface current ($J = 0$ on $\partial V'$), it is followed by that the volume integrals of the first two terms on the right in (B-9) are vanished.

$$\begin{aligned} \int_{V'} \nabla' \Big(g\nabla \cdot \mathbf{J}(\mathbf{r}') \Big) dr' &= -\int_{V'} \nabla' \Big(g \frac{\partial \varrho}{\partial t} \Big) d\mathbf{r}' = 0 \\ \int_{V'} \nabla' \cdot \Big(\nabla' g \cdot \mathbf{J}(\mathbf{r}') \Big) dr' &= \int_{\partial V'} \nabla' g \cdot \mathbf{J}(\mathbf{r}') \; d\Omega' = 0 \end{aligned} \tag{B-10}$$

As a result, with the aid of (B-9) and (B-10), Eq. (B-7) becomes to that

$$\mathbf{E}(\mathbf{r}) = i\omega\mu \int_{V'} \mathbf{J}(\mathbf{r}') \cdot \left(\bar{\bar{I}} + \frac{\nabla'\nabla'}{k^2} \right) g(\mathbf{r}, \mathbf{r}')d\mathbf{r}' \tag{B-11}$$

Denote $\bar{\bar{\mathbf{G}}}$ as the dyadic Green's function,

$$\bar{\bar{\mathbf{G}}} = \begin{bmatrix} g_{xx} & 0 & 0 \\ 0 & g_{yy} & 0 \\ g_{xz} & g_{yz} & g_{zz} \end{bmatrix} \tag{B-12}$$

where, for instance, g_{xz} represents the response in z-direction due to the x-direction excitation. The reason for the missing component of g_{xy} is due to the natural restriction from the interface. By substituting (B-12) back into (B-11) and denoting that

$$\mathbf{J}(\mathbf{r}) = I\Delta l \delta(\mathbf{r}-\mathbf{r}') \tag{B-13}$$

the electric field due to infinitesimal current source is readily obtained in terms of the dyadic Green's function via

$$\mathbf{E} = \frac{i\omega\mu I\Delta l}{k^2}\left(k^2 + \nabla\nabla\right)\bar{\bar{\mathbf{G}}}. \tag{B-14}$$

In this project, due to the difficulty in obtaining the information about the antenna source, the transmitter is presumed as a vertical line antenna, as well as the receiver. As a result, only the vertical source is considered, and the received electric field is in vertical direction only as well.

Vertical source

For a vertical source, viz, $g(\mathbf{r})\hat{e}_z = g_{zz}(\mathbf{r})\hat{e}_z \neq 0$, the electric field is determined by that,

$$\mathbf{E}(\mathbf{r}) = \frac{i\omega\mu I\Delta l}{k^2}\left(k^2 + \nabla\nabla\right)g(\mathbf{r})\hat{e}_z. \tag{B-15}$$

After some manipulation, the components of the electric field in (B-15) can be shown in cylindrical coordinate as

$$\begin{aligned} E_\rho(\rho, z) &= \frac{i\omega\mu I\Delta l}{k^2}\frac{\partial}{\partial\rho}\left(\frac{\partial}{\partial z}\, g(\rho, z)\right) \\ E_z(\rho, z) &= \frac{i\omega\mu I\Delta l}{k^2}\left(k^2 + \frac{\partial^2}{\partial z^2}\right)g(\rho, z) \end{aligned} \tag{B-16}$$

where $r^2 = \rho^2 + z^2$ and the E_θ does not exist due to symmetry.

Introduce the nth-order Hankel transform which is defined as a pair of integral transforms via

$$\begin{aligned} \tilde{f}_n(\xi, z) &= \int_0^\infty f(\rho, z)J_n(\xi\rho)\rho d\rho \\ f_n(\rho, z) &= \int_0^\infty \tilde{f}(\xi, z)J_n(\xi\rho)\xi d\xi \end{aligned} \tag{B-17}$$

where J_n is the nth-order Bessel function of the first kind. Upon applying the 1st-order and 0th-order Hankel transforms to E_ρ and E_z, respectively, the transformed field of (B-16) can

be shown as

$$\begin{aligned}\tilde{E}^1_\rho(\xi,z) &= \frac{i\omega\mu I\Delta l}{k^2}\frac{\partial}{\partial z}\int_0^\infty \frac{\partial}{\partial \rho}\, g(\rho,z)\,\rho J_1(\xi\rho)d\rho \\ \tilde{E}^0_z(\xi,z) &= \frac{i\omega\mu I\Delta l}{k^2}\left(k^2+\frac{\partial^2}{\partial z^2}\right)\int_0^\infty g(\rho,z)\,\rho J_1(\xi\rho)d\rho\end{aligned} \tag{B-18}$$

where the superscript indicates the order of Hankel transform. By means of the identities that

$$\frac{\partial}{\partial \rho}J_0(\xi\rho) = -\xi J_1(\xi\rho), \quad J_1(\xi\rho)+\rho\frac{\partial}{\partial \rho}J_1(\xi\rho) = \rho\xi J_0(\xi\rho) \tag{B-19}$$

it can be observed that

$$\int_0^\infty \frac{\partial}{\partial \rho}\, g(\rho,z)\,\rho J_1(\xi\rho)d\rho = -\xi\int_0^\infty g(\rho,z)\,\rho J_0(\xi\rho)d\rho = -\xi\,\tilde{g}^0(\xi,z). \tag{B-20}$$

In addition, the partial derivative with respect to z in the above is in fact a full derivative, i.e.,

$$\frac{\partial}{\partial z}\tilde{g}^0(\xi,z) = \frac{d}{dz}\tilde{g}^0(\xi,z) = \tilde{g}'(\xi,z) \tag{B-21}$$

where the superscript for the order of Hankel transform is suppressed.

In what follows, upon applying the 0th-order Hankel transform to Eq. (B-6), it is readily to show the following

$$\left(\frac{d^2}{dz^2}+k^2-\xi^2\right)\tilde{g} = 0 \tag{B-22}$$

in which the solution of $\tilde{g}$ is obtained via

$$\tilde{g}(\xi,z) = A(\xi)e^{\gamma z}+B(\xi)e^{-\gamma z} \tag{B-23}$$

where $\gamma^2 = \xi^2 - k^2$ and the depth-independent coefficients $A(\xi)$ and $B(\xi)$ are determined by the boundary conditions. Therefore, with the aid of (B-20) and (B-21), Eq. (B-18) becomes to that

$$\begin{aligned}\tilde{E}_\rho(\xi,z) &= \frac{-i\omega\mu I\Delta l}{k^2}\,\xi\,\tilde{g}'(\xi,z) \\ \tilde{E}_z(\xi,z) &= \frac{i\omega\mu I\Delta l}{k^2}\,\xi^2\,\tilde{g}(\xi,z)\end{aligned} \tag{B-24}$$

where the superscript for the order of Hankel transform is suppressed. Note that in (B-24) the $\tilde{g}$ is obtained via the 0th-order Hankel transform, as well as the $\tilde{E}_z$. The $\tilde{E}_\rho$, however, is obtained via the 1st-order Hankel transform.

Layered solution

Consider a n parallel layered system in between two half-spaces with a cylindrical coordinate system set at the bottom of the upper half-space (see Fig. B-1). All the layers are labeled from 0 (upper half space, air) to $n+1$ (lower half space). The jth layer denoted as domain $\mathcal{L}_j\,(j = 0, 1, \cdots, n+1)$ is characterized by its material parameters: dielectric constant ε_j, permeability μ_j, conductivity σ_j and layer thickness $h_j = z_j - z_{j-1}$ where z_j and z_{j-1} are the depths of its upper and lower interfaces.

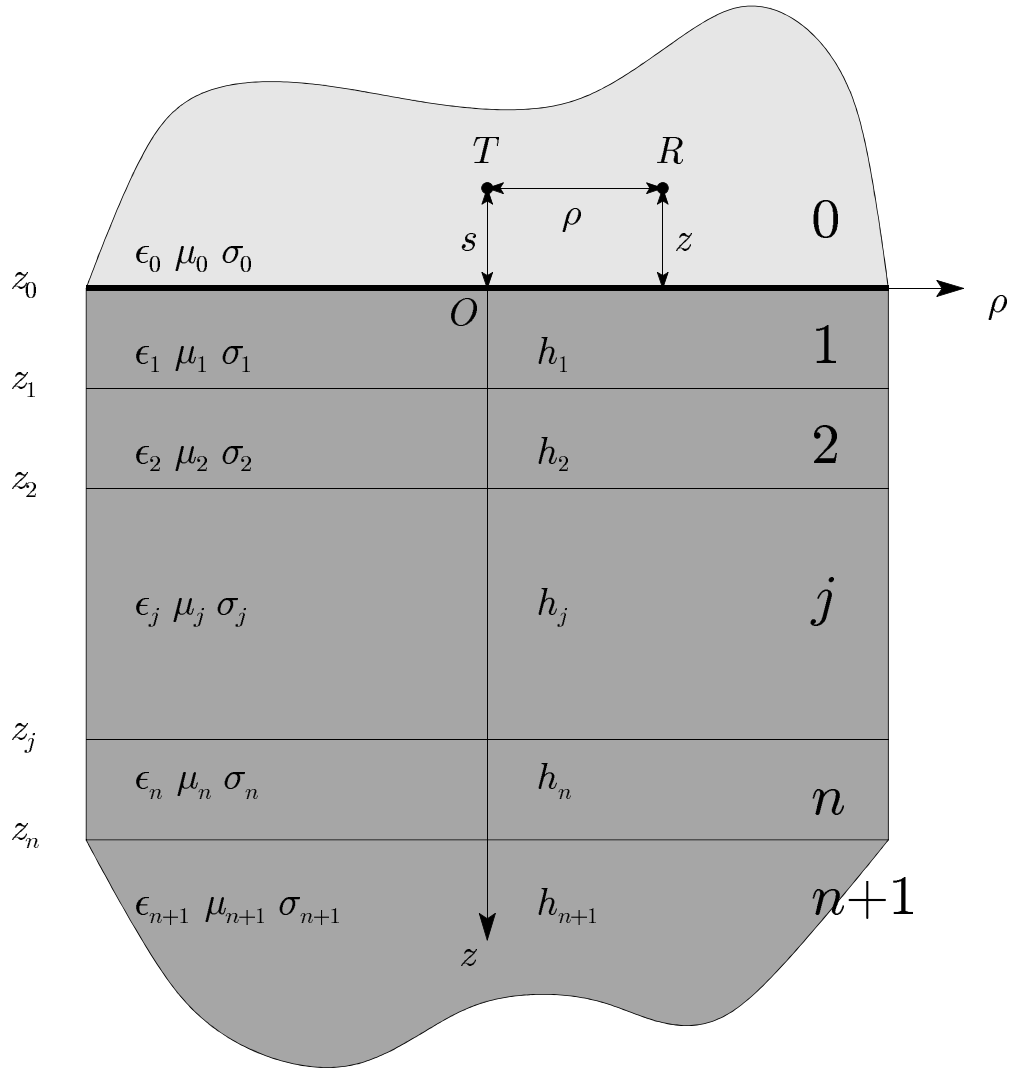

Figure B-1: Schematic of layered structure

When crossing the layer interface, the electric field can be described as that the component of **E** parallel to the interface is continuous, whereas the component of **E** perpendicular to the interface has a jump. Since the layers are horizontally placed in the setup, one can

obtain the following on the jth interface ($z = z_j$)

$$E_{\rho,j}(\rho, z_j) = E_{\rho,j+1}(\rho, z_j), \quad \varepsilon_j E_{z,j}(\rho, z_j) = \varepsilon_{j+1} E_{z,j+1}(\rho, z_j). \tag{B-25}$$

By means of Hankel transform in (B-17), Eq. (B-25) is transformed into that

$$\tilde{E}_{\rho,j}(\xi, z_j) = \tilde{E}_{\rho,j+1}(\xi, z_j), \quad \varepsilon_j \tilde{E}_{z,j}(\xi, z_j) = \varepsilon_{j+1} \tilde{E}_{z,j+1}(\xi, z_j) \tag{B-26}$$

or in terms of $\tilde{g}(\xi, z)$ via (B-24)

$$\begin{aligned} \frac{1}{\varepsilon_j} \tilde{g}'_j(\xi, z_j) &= \frac{1}{\varepsilon_{j+1}} \tilde{g}'_{j+1}(\xi, z_j) \\ \tilde{g}_j(\xi, z_j) &= \tilde{g}_{j+1}(\xi, z_j) \end{aligned} \tag{B-27}$$

With the aid of (B-23) and (B-24), the solutions for the layers without excitation source are readily obtained except those depth-independent coefficients $A_j(\xi)$ and $B_j(\xi)$. In the lth layer where $z_{l-1} < s < z_l$, it is convenient to decompose the solution into portions with and without the source. As a result, in domain $\mathcal{L}_l$, one may express the solution through depth-dependent coefficients in terms of the depth-independent coefficients $A(\xi)$ and $B(\xi)$

$$\begin{aligned} A_l(\xi, z) &= A_l(\xi) + H(s - z) A_{l,p}(\xi) \\ B_l(\xi, z) &= B_l(\xi) + H(z - s) B_{l,p}(\xi) \end{aligned} \tag{B-28}$$

where H denotes the Heaviside step function; $A_{l,p}(\xi)$ and $B_{l,p}(\xi)$ are coefficients for particular solutions due to the existing source.

Since the Green's function in homogeneous full-space is known as $e^{ikr}/4\pi r$, upon applying the 0th-order Hankel transform, one may obtain the transformed field via

$$\frac{e^{ikr}}{4\pi r} = \int_0^\infty \frac{e^{-\gamma|z|}}{4\pi\gamma} J_0(\xi\rho)\xi \, d\xi \tag{B-29}$$

where $r^2 = \rho^2 + z^2$ is in cylindrical coordinate. The above transform is also known as Sommerfeld identity. With the aid of (B-29), the particular solutions in domain $\mathcal{L}_l$ are readily obtained via

$$\begin{aligned} A_{l,p}(\xi) &= \frac{1}{4\pi\gamma_l}, \quad z_{l-1} < z < s \\ B_{l,p}(\xi) &= \frac{1}{4\pi\gamma_l}, \quad s < z < z_l. \end{aligned} \tag{B-30}$$

Propagator matrix

For analytical and numerical purpose, it is useful to introduce dimensionless parameters for all the domains

$$\begin{gathered}\bar{\rho} = k_0\rho, \quad \bar{z} = k_0 z, \quad \bar{h} = k_0 h, \quad \bar{z}_j = k_0 z_j, \quad \bar{s} = k_0 s \\ \bar{\xi} = \xi/k_0, \quad \bar{\varepsilon}_j = \varepsilon_j/\varepsilon_0, \quad \bar{\mu}_j = \mu_j/\mu_0, \quad \bar{k}_j = k_j/k_0\end{gathered} \tag{B-31}$$

where ε_0 and μ_0 are reference permittivity and permeability, respectively; $k_0 = \omega\sqrt{\varepsilon_0\mu_0}$ is reference wave number. In addition, the unknown coefficients A_j and B_j may be recast in dimensionless form as

$$\begin{aligned}\alpha_j(\bar{\xi},\bar{z}) &= a_j(\bar{\xi}) + \delta_{jl}H(\bar{s}-\bar{z})a_{l,p}(\bar{\xi}) = \frac{k_0}{\omega\mu_0 I\Delta l}A_j\, e^{\bar{\gamma}_j\bar{z}_j} \\ \beta_j(\bar{\xi},\bar{z}) &= b_j(\bar{\xi}) + \delta_{jl}H(\bar{z}-\bar{s})b_{l,p}(\bar{\xi}) = \frac{k_0}{\omega\mu_0 I\Delta l}B_j\, e^{-\bar{\gamma}_j\bar{z}_{j-1}}\end{aligned} \tag{B-32}$$

where δ_{jl} denotes Kronecker delta. By means of (B-23), (B-31) and (B-32), the dimensionless form of (B-24) is given by

$$\begin{aligned}\tilde{v}_{\rho,j}(\bar{\xi},\bar{z}) &= \frac{-i\bar{\mu}_j}{\bar{k}_j^2}\,\bar{\xi}\,g' = \frac{i}{\bar{\varepsilon}_j}\,\bar{\xi}\,\bar{\gamma}_j\left[-\alpha_j(\bar{\xi},\bar{z})e^{\bar{\gamma}_j(\bar{z}-\bar{z}_j)} + \beta_j(\bar{\xi},\bar{z})e^{-\bar{\gamma}_j(\bar{z}-\bar{z}_{j-1})}\right] \\ \tilde{v}_{z,j}(\bar{\xi},\bar{z}) &= \frac{i\bar{\mu}_j}{\bar{k}_j^2}\,\bar{\xi}^2\,g = \frac{i}{\bar{\varepsilon}_j}\,\bar{\xi}^2\left[\alpha_j(\bar{\xi},\bar{z})e^{\bar{\gamma}_j(\bar{z}-\bar{z}_j)} + \beta_j(\bar{\xi},\bar{z})e^{-\bar{\gamma}_j(\bar{z}-\bar{z}_{j-1})}\right],\end{aligned} \tag{B-33}$$

or in matrix form via

$$\begin{bmatrix}\tilde{v}_{\rho,j}(\bar{\xi},\bar{z}) \\ \\ \tilde{v}_{z,j}(\bar{\xi},\bar{z})\end{bmatrix} = \begin{bmatrix}\dfrac{i}{\bar{\varepsilon}_j}\bar{\xi}^2 & \dfrac{i}{\bar{\varepsilon}_j}\bar{\xi}^2 \\ \\ \dfrac{-i}{\bar{\varepsilon}_j}\bar{\xi}\bar{\gamma}_j & \dfrac{i}{\bar{\varepsilon}_j}\bar{\xi}\bar{\gamma}_j\end{bmatrix}\begin{bmatrix}\alpha_j(\bar{\xi},\bar{z})e^{\bar{\gamma}_j(\bar{z}-\bar{z}_j)} \\ \\ \beta_j(\bar{\xi},\bar{z})e^{-\bar{\gamma}_j(\bar{z}-\bar{z}_{j-1})}\end{bmatrix} \tag{B-34}$$

whereas the dimensionless interfacial conditions on the jth interface is that

$$\begin{aligned}\tilde{v}_{\rho,j}(\bar{\xi},\bar{z}_j) &= \tilde{v}_{\rho,j+1}(\bar{\xi},\bar{z}_j) \\ \bar{\varepsilon}_j\tilde{v}_{z,j}(\bar{\xi},\bar{z}_j) &= \bar{\varepsilon}_{j+1}\tilde{v}_{\bar{\xi},z,j+1}(\bar{\xi},\bar{z}_j).\end{aligned} \tag{B-35}$$

From (B-34), one may observe that the coefficient α_j is associated with wave propagating upward because of $e^{\bar{\gamma}_j\bar{z}}$. Vice versa, the coefficient β_j is associated with wave propagating downward. In addition, for the electric field due to a vertical dipole source, there are 2 unknowns (α and β) in each layer. As a result, for the general $n+2$ layered system, $2(n+2)$

unknowns in total are required to be determined. With the aid of interfacial conditions in (B-35), it is possible to establish a relationship between the dimensionless coefficients in the jth layer and the adjacent layer. However, there are only $n+1$ interfaces which provide $2(n+1)$ relationships, leaving the last two relationships come from the regularity condition of the two half spaces, i.e.,

$$\begin{aligned} \lim_{\bar{z}\to\pm\infty} \tilde{v}_\rho(\bar{\xi},\bar{z}) &= 0 \\ \lim_{\bar{z}\to\pm\infty} \tilde{v}_z(\bar{\xi},\bar{z}) &= 0. \end{aligned} \tag{B-36}$$

Prompted by the presence of $e^{\bar{\gamma}_j\bar{z}_j}$ and $e^{-\bar{\gamma}_j\bar{z}_j}$ in (B-33), the regularity conditions in (B-36) turns out to be that

$$\alpha_{n+1}(\bar{\xi},\bar{z}) = 0, \quad \beta_0(\bar{\xi},\bar{z}) = 0. \tag{B-37}$$

In the following, upon applying the interfacial conditions (B-35) to the matrix form representation (B-34) and after some manipulation, the so-called propagator matrix is obtained via

$$\begin{bmatrix} \alpha_j(\bar{\xi},\bar{z}_j) \\ \\ \beta_{j+1}(\bar{\xi},\bar{z}_j) \end{bmatrix} = \begin{bmatrix} T_j^u(\bar{\xi}) & R_j^d(\bar{\xi}) \\ \\ R_j^u(\bar{\xi}) & T_j^d(\bar{\xi}) \end{bmatrix} \begin{bmatrix} \mathcal{E}_{j+1} & 0 \\ \\ 0 & \mathcal{E}_j \end{bmatrix} \begin{bmatrix} \alpha_{j+1}(\bar{\xi},\bar{z}_j) \\ \\ \beta_j(\bar{\xi},\bar{z}_j) \end{bmatrix} \tag{B-38}$$

where $\mathcal{E}_j = e^{-\bar{\gamma}_j\bar{h}_j}$ and denoting $\bar{\chi}_j = \bar{\gamma}_j/\bar{\varepsilon}_j$

$$\begin{bmatrix} T_j^u(\bar{\xi}) & R_j^d(\bar{\xi}) \\ \\ R_j^u(\bar{\xi}) & T_j^d(\bar{\xi}) \end{bmatrix} = \frac{1}{\bar{\chi}_j + \bar{\chi}_{j+1}} \begin{bmatrix} 2\bar{\chi}_{j+1} & \bar{\chi}_j - \bar{\chi}_{j+1} \\ \\ \bar{\chi}_{j+1} - \bar{\chi}_j & 2\bar{\chi}_j \end{bmatrix} \tag{B-39}$$

In the above, T_j and R_j are denoted as transmission and reflection coefficients of the jth interface, respectively; the superscripts "d"(downward) and "u"(upward) denote the directions of wave propagation. For example, the upward propagation wave in the jth layer is the addition of two terms, viz, the upward propagation wave in the lower layer ($j+1$th) after transmitted through the jth interface and the downward propagation wave in the same layer (jth) after reflected from the jth interface, as shown in Fig. B-2.

With the aid of the regularity condition in (B-37) that $\beta_0(\bar{\xi},\bar{z}) = 0$, (B-38) can be expressed in the layer $j = 1$ as

$$\begin{aligned} \beta_1(\bar{\xi},\bar{z}_0) &= R_0^u\mathcal{E}_1\alpha_1(\bar{\xi},\bar{z}_0), \quad \text{at } \bar{z} = \bar{z}_0 \\ \alpha_1(\bar{\xi},\bar{z}_1) &= T_1^u\mathcal{E}_2\alpha_2(\bar{\xi},\bar{z}_1) + R_1^d\mathcal{E}_1\beta_1(\bar{\xi},\bar{z}_1), \quad \text{at } \bar{z} = \bar{z}_1 \end{aligned} \tag{B-40}$$

Prompted by (B-32) and the fact that layer 1 contains no excitation source, one may observe that

$$\alpha_1(\bar{\xi},\bar{z}_0) = \alpha_1(\bar{\xi},\bar{z}_1) = \alpha_1, \quad \beta_1(\bar{\xi},\bar{z}_0) = \beta_1(\bar{\xi},\bar{z}_1) = \beta_1 \tag{B-41}$$

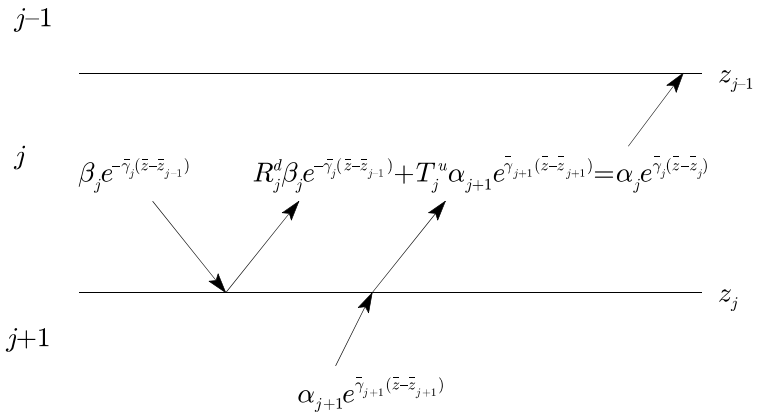

Figure B-2: Reflection and transmission coefficients

Therefore, (B-40) can be reformulated in a compact forms via

$$\begin{aligned} \beta_1 &= \widehat{R}_0^u \mathcal{E}_1 \alpha_1 \\ \alpha_1 &= \left(1 - R_1^d \widehat{R}_0^u \mathcal{E}_1^2\right)^{-1} T_1^u \mathcal{E}_2 \alpha_2 = \widehat{T}_1^u \mathcal{E}_2 \alpha_2 \end{aligned} \tag{B-42}$$

Similarly, in the layer $j = 2$, the coefficients can be formulated as

$$\begin{aligned} \beta_2 &= R_1^u \mathcal{E}_2 \alpha_2 + T_1^d \mathcal{E}_1 \beta_1 \\ \alpha_2 &= T_2^u \mathcal{E}_3 \alpha_3 + R_2^d \mathcal{E}_2 \beta_2 \end{aligned} \tag{B-43}$$

and the compact forms after manipulation are given via

$$\begin{aligned} \beta_2 &= \left(R_1^u + T_1^d \widehat{R}_0^u \widehat{T}_1^u \mathcal{E}_1^2\right) \mathcal{E}_2 \alpha_2 = \widehat{R}_1^u \mathcal{E}_2 \alpha_2 \\ \alpha_2 &= \left(1 - R_2^d \widehat{R}_1^u \mathcal{E}_2^2\right)^{-1} T_2^u \mathcal{E}_3 \alpha_3 = \widehat{T}_2^u \mathcal{E}_3 \alpha_3 \end{aligned} \tag{B-44}$$

In the above, $\widehat{T}_j$ and $\widehat{R}_j$ are called generalized transmission and reflection coefficients which take account of the multiple transmissions and reflections above or under the jth layer. In fact, they can be obtained recursively via

$$\begin{aligned} \widehat{T}_j^u &= \left(1 - R_j^d \widehat{R}_{j-1}^u \mathcal{E}_j^2\right)^{-1} T_j^u \\ \widehat{R}_j^u &= R_j^u + T_j^d \widehat{R}_{j-1}^u \widehat{T}_j^u \mathcal{E}_j^2 \\ \widehat{R}_{-1}^u &= 0 \end{aligned} \tag{B-45}$$

and the equation at $\bar{z} = \bar{z}_{l-1}$

$$\beta_l(\bar{\xi}, \bar{z}_{l-1}) = \widehat{R}^u_{l-1}\mathcal{E}_l\alpha_l(\bar{\xi}, \bar{z}_{l-1}) \tag{B-46}$$

for all layers above the source ($0 \leqslant j \leqslant l-1$), as well as

$$\begin{aligned} \widehat{T}^d_j &= \left(1 - R^u_j\widehat{R}^d_{j+1}\mathcal{E}^2_j\right)^{-1} T^d_j \\ \widehat{R}^d_j &= R^d_j + T^u_j\widehat{R}^d_{j+1}\widehat{T}^d_j\mathcal{E}^2_j \\ \widehat{R}^d_{n+1} &= 0 \end{aligned} \tag{B-47}$$

and the equation at $\bar{z} = \bar{z}_l$

$$\alpha_l(\bar{\xi}, \bar{z}_l) = \widehat{R}^d_l\mathcal{E}_l\beta_l(\bar{\xi}, \bar{z}_l) \tag{B-48}$$

for all layers below the source ($l+1 \leqslant j \leqslant n+1$).

For layer $j = l$ which contains the excitation source, upon substituting (B-32) into (B-46) and (B-48) and solving for the unknowns a_l and b_l, one may obtain the explicit expression as

$$\begin{aligned} a_l(\bar{\xi}) &= \left(1 - \widehat{R}^d_l\widehat{R}^u_{l-1}\mathcal{E}^2_l\right)^{-1}\left(\widehat{R}^d_l\mathcal{E}_l b_{l,p}(\bar{\xi}) + \widehat{R}^d_l\widehat{R}^u_{l-1}\mathcal{E}^2_l a_{l,p}(\bar{\xi})\right) \\ b_l(\bar{\xi}) &= \left(1 - \widehat{R}^d_l\widehat{R}^u_{l-1}\mathcal{E}^2_l\right)^{-1}\left(\widehat{R}^u_{l-1}\mathcal{E}_l a_{l,p}(\bar{\xi}) + \widehat{R}^u_{l-1}\widehat{R}^d_l\mathcal{E}^2_l b_{l,p}(\bar{\xi})\right) \end{aligned} \tag{B-49}$$

where

$$a_{l,p}(\bar{\xi}) = b_{l,p}(\bar{\xi}) = \frac{1}{4\pi\bar{\gamma}_l} \tag{B-50}$$

Therefore, the total coefficients for the source layer are given by

$$\begin{aligned} \alpha_l(\bar{\xi}, \bar{z}) &= \left(1 - \widehat{R}^d_l\widehat{R}^u_{l-1}\mathcal{E}^2_l\right)^{-1}\left(\widehat{R}^d_l\mathcal{E}_l b_{l,p} + \widehat{R}^d_l\widehat{R}^u_{l-1}\mathcal{E}^2_l a_{l,p}\right) + H(\bar{s} - \bar{z})a_{l,p} \\ \beta_l(\bar{\xi}, \bar{z}) &= \left(1 - \widehat{R}^d_l\widehat{R}^u_{l-1}\mathcal{E}^2_l\right)^{-1}\left(\widehat{R}^u_{l-1}\mathcal{E}_l a_{l,p} + \widehat{R}^u_{l-1}\widehat{R}^d_l\mathcal{E}^2_l b_{l,p}\right) + H(\bar{z} - \bar{s})b_{l,p} \end{aligned} \tag{B-51}$$

To this point, based on equations (B-38)∼(B-51), one may extend the derivation for the coefficients α_l and β_l in the source layer to other coefficients α_j and β_j for the layers above and below the source layer.

Without losing any generality, one may assume that the source is located in the upper half of the source layer, i.e., $\bar{z}_{l-1} < \bar{s} < (\bar{z}_{l-1} + \bar{z}_l)/2$. For $\bar{z} > \bar{s}$, the lth layer coefficients

become to that

$$\begin{aligned}\bar{g}_l(\bar{\xi},\bar{z}) &= \alpha_l(\bar{\xi},\bar{z})e^{\bar{\gamma}_l(\bar{z}-\bar{z}_l)} + \beta_l(\bar{\xi},\bar{z})e^{-\bar{\gamma}_l(\bar{z}-\bar{z}_{l-1})} \\ &= \frac{1}{4\pi\bar{\gamma}_l}\left(1-\widehat{R}_l^d\widehat{R}_{l-1}^u\mathcal{E}_l^2\right)^{-1}... \\ &\quad\times\left(\widehat{R}_l^d e^{-\bar{\gamma}_l(2\bar{z}_l-\bar{z}-\bar{s})} + \widehat{R}_{l-1}^u e^{-\bar{\gamma}_l(\bar{s}+\bar{z}-2\bar{z}_{l-1})} + e^{-\bar{\gamma}_l(\bar{z}-\bar{s})}\ ...\right. \\ &\quad\left.+\ \widehat{R}_{l-1}^u\widehat{R}_l^d\mathcal{E}_l^2 e^{-\bar{\gamma}_l(\bar{s}-\bar{z})}\right)\end{aligned} \tag{B-52}$$

In what follows,

$$e^{-\bar{\gamma}_l(2\bar{z}_l-\bar{z}-\bar{s})} \sim o(e^{-\bar{\xi}_l\bar{h}_l/2}), \quad e^{-\bar{\gamma}_l\bar{h}_l} \sim o(e^{-\bar{\xi}\bar{h}_l}), \tag{B-53}$$

when $\bar{\xi}\to\infty$, which results in the approximation of (B-52) by the following

$$\bar{g}_l(\bar{\xi},\bar{z}) \sim \frac{1}{4\pi\bar{\gamma}_l}\left(e^{-\bar{\gamma}_l(\bar{z}-\bar{s})} + \widehat{R}_{l-1}^u e^{-\bar{\gamma}_l(\bar{z}+\bar{s}-2\bar{z}_{l-1})}\right). \tag{B-54}$$

Furthermore, based on (B-39) and (B-45), it can be shown that

$$\widehat{R}_j^u = R_j^u + \frac{T_j^d\widehat{R}_{j-1}^u T_j^u\mathcal{E}_j^2}{1-R_j^d R_{j-1}^u\mathcal{E}_j^2} \sim R_j^u \tag{B-55}$$

when $\bar{\xi}\to\infty$, i.e.,

$$\widehat{R}_j^u \sim \frac{\bar{\chi}_{j+1}-\bar{\chi}_j}{\bar{\chi}_{j+1}+\bar{\chi}_j} \tag{B-56}$$

where $\bar{\chi}_j = \bar{\gamma}_j/\bar{\varepsilon}_j$. Upon substituting (B-56) into (B-54), one may define the asymptotic term of the total kernel as

$$\bar{g}_l^a(\bar{\xi},\bar{z}) = \frac{1}{4\pi\bar{\xi}}\left(e^{-\bar{\gamma}_l(\bar{z}-\bar{s})} + \frac{\bar{\chi}_{j+1}-\bar{\chi}_j}{\bar{\chi}_{j+1}+\bar{\chi}_j}e^{-\bar{\gamma}_l(\bar{z}+\bar{s}-2\bar{z}_{l-1})}\right) \tag{B-57}$$

in which the superscript "a" denotes asymptotic. To simplify the formula, one may define the relative dimensionless depths as the local variables with respect to the interface at depth $\bar{z}_{l-1}$ as

$$\bar{z}' = \bar{z}-\bar{z}_{l-1}, \quad \bar{s}' = \bar{s}-\bar{z}_{l-1} \tag{B-58}$$

and the dimensionless distance variable as

$$\bar{d}_1 = |\bar{z}'-\bar{s}'|, \quad \bar{d}_2 = \bar{z}'+\bar{s}'. \tag{B-59}$$

As a result of (B-33), the asymptotic term of the total kernel for $\bar{z}>\bar{s}$ in domain $\mathcal{L}_l$ may

be written as

$$\begin{aligned}\tilde{v}^a_{\rho,l}(\bar{\xi},\bar{z}) &= \frac{i\bar{\xi}}{4\pi\bar{\varepsilon}_l}\left(-e^{-\bar{\gamma}_l\bar{d}_1}+\frac{\bar{\chi}_{l+1}-\bar{\chi}_l}{\bar{\chi}_{l+1}+\bar{\chi}_l}e^{-\bar{\gamma}_l\bar{d}_2}\right)\\ \tilde{v}^a_{z,l}(\bar{\xi},\bar{z}) &= \frac{i\bar{\xi}^2}{4\pi\bar{\varepsilon}_l\bar{\gamma}_l}\left(e^{-\bar{\gamma}_l\bar{d}_1}+\frac{\bar{\chi}_{l+1}-\bar{\chi}_l}{\bar{\chi}_{l+1}+\bar{\chi}_l}e^{-\bar{\gamma}_l\bar{d}_2}\right)\end{aligned} \tag{B-60}$$

In the same manner, one may derive the asymptotic term for $\bar{z}<\bar{s}$ in domain $\mathcal{L}_l$ as

$$\begin{aligned}\tilde{v}^a_{\rho,l}(\bar{\xi},\bar{z}) &= \frac{i\bar{\xi}}{4\pi\bar{\varepsilon}_l}\left(e^{-\bar{\gamma}_l\bar{d}_1}+\frac{\bar{\chi}_{l+1}-\bar{\chi}_l}{\bar{\chi}_{l+1}+\bar{\chi}_l}e^{-\bar{\gamma}_l\bar{d}_2}\right)\\ \tilde{v}^a_{z,l}(\bar{\xi},\bar{z}) &= \frac{i\bar{\xi}^2}{4\pi\bar{\varepsilon}_l\bar{\gamma}_l}\left(e^{-\bar{\gamma}_l\bar{d}_1}+\frac{\bar{\chi}_{l+1}-\bar{\chi}_l}{\bar{\chi}_{l+1}+\bar{\chi}_l}e^{-\bar{\gamma}_l\bar{d}_2}\right)\end{aligned} \tag{B-61}$$

In the above, since the source is located in the upper half of the lth layer, the $l-1$th interface is the closest one to the source, which in turn has the largest impact on the electromagnetic field over the other interfaces. As a result, one may consider a local system that includes the interface at depth $\bar{z}_{l-1}$, the $l-1$th and lth layers. The majority of the wave energy is enclosed within this local system, whereas at a further distance outside the wave is exponentially vanished. In other words, the asymptotic term capture the singularity of the total kernel.

One can also show that when source is located in the lower half of the source layer, i.e., $(\bar{z}_{l-1}+\bar{z}_l)/2<\bar{s}<\bar{z}_l$, the local variables are defined with respect to the interface at depth $\bar{z}_l$ which is, nevertheless, the closest one to the source. In addition, instead of the $l-1$th layer, the $l+1$th layer should be included in the local system as well as the lth layer and the interface at depth $\bar{z}_l$.

In order to obtain the electric field in the original form, one should apply the Hankel transform in (B-17) to the transformed fields in (B-60) and (B-61). However, due to the rapid oscillation of the Bessel function when its variable is at ∞, the success of a fast integration may be limited for a conventional numerical integration scheme.

To expedite the integration, first of all, the Eq. (B-60) and (B-61) in which the integrand may be considered as a function of $\bar{\xi}$ only shall be rephrased here

$$\begin{aligned}\tilde{v}^a_{\rho,1}(\bar{\xi}) &= \frac{i\bar{\xi}}{4\pi\bar{\varepsilon}_1}\left(\pm e^{-\bar{\gamma}_1\bar{d}_1}+\frac{\bar{\chi}_2-\bar{\chi}_1}{\bar{\chi}_2+\bar{\chi}_1}e^{-\bar{\gamma}_1\bar{d}_2}\right)\\ \tilde{v}^a_{z,1}(\bar{\xi}) &= \frac{i\xi^2}{4\pi\bar{\varepsilon}_1\bar{\gamma}_1}\left(e^{-\bar{\gamma}_1\bar{d}_1}+\frac{\bar{\chi}_2-\bar{\chi}_1}{\bar{\chi}_2+\bar{\chi}_1}e^{-\bar{\gamma}_1\bar{d}_2}\right).\end{aligned} \tag{B-62}$$

where the domain contains the source is labeled as "1" and the other adjacent layer as "2"; all the layer properties are labeled with respect to the layer they belong to.

The first terms inside the parenthesis may be considered separately, whose integrations,

denoted as $\mathcal{J}_1^\gamma(\bar{z})$ and $\mathcal{J}_0^\gamma(\bar{z})$, can be obtained in closed-form via

$$\begin{aligned}\mathcal{J}_1^\gamma(\bar{z}) = \int_0^\infty e^{-\bar{\gamma}\bar{z}}\bar{\xi}^2\, J_1(\bar{\xi}\bar{\rho})\, d\bar{\xi} &= \left(-\frac{\bar{z}\bar{\rho}\bar{k}^2}{\bar{r}^3} - \frac{3i\bar{z}\bar{\rho}\bar{k}}{\bar{r}^4} + \frac{3\bar{z}\bar{\rho}}{\bar{r}^5}\right) e^{i\bar{k}\bar{r}} \\ \mathcal{J}_0^\gamma(\bar{z}) = \int_0^\infty e^{-\bar{\gamma}\bar{z}}\frac{\bar{\xi}^3}{\bar{\gamma}}\, J_0(\bar{\xi}\bar{\rho})\, d\bar{\xi} &= \left(\frac{\bar{k}^2\bar{\rho}^2}{\bar{r}^3} - \frac{i\bar{k}(2\bar{z}^2-\bar{\rho}^2)}{\bar{r}^4} + \frac{\bar{z}^2-\bar{\rho}^2}{\bar{r}^5}\right) e^{i\bar{k}\bar{r}}\end{aligned} \tag{B-63}$$

where $\bar{r}^2 = \bar{z}^2 + \bar{\rho}^2$ and $\bar{k}^2 = \bar{\gamma}^2 - \bar{\xi}^2$, which leaves the computation to the evaluation of the second terms inside the parenthesis.

To the second terms, the closed-form integrations are not available, but available to the asymptote of the integrand as will be illustrated below. In what follows, due to the fact that Bessel function is bounded around zero,

$$\lim_{x\to 0} J_0(x) \to 1, \quad \lim_{x\to 0} J_1(x) \to 0 \tag{B-64}$$

the integrands are bounded around zero as well. When $\bar{\xi} \to \infty$, the integrands of the second terms can be expanded as the following

$$\begin{aligned}\frac{\bar{\varepsilon}_2\bar{\gamma}_1 - \bar{\varepsilon}_1\bar{\gamma}_2}{\bar{\varepsilon}_2\bar{\gamma}_1 + \bar{\varepsilon}_1\bar{\gamma}_2}\,\bar{\xi}^2 e^{-\bar{\gamma}_1\bar{z}} &\sim \left[c_{\rho,2}(\bar{z})\,\bar{\xi}^2 + c_{\rho,1}(\bar{z})\,\bar{\xi} + c_{\rho,0}(\bar{z}) + o(\bar{\xi}^{-1})\right] e^{-\bar{\xi}\bar{z}} \\ \frac{\bar{\varepsilon}_2\bar{\gamma}_1 - \bar{\varepsilon}_1\bar{\gamma}_2}{\bar{\varepsilon}_2\bar{\gamma}_1 + \bar{\varepsilon}_1\bar{\gamma}_2}\,\frac{\bar{\xi}^3}{\bar{\gamma}_2} e^{-\bar{\gamma}_1\bar{z}} &\sim \left[c_{z,2}(\bar{z})\,\bar{\xi}^2 + c_{z,1}(\bar{z})\,\bar{\xi} + c_{z,0}(\bar{z}) + o(\bar{\xi}^{-1})\right] e^{-\bar{\xi}\bar{z}}\end{aligned} \tag{B-65}$$

where

$$\begin{aligned} c_{\rho,2}(\bar{z}) &= c_{z,2}(\bar{z}) = \frac{\bar{\varepsilon}_1 - \bar{\varepsilon}_2}{\bar{\varepsilon}_1 + \bar{\varepsilon}_2} \\ c_{\rho,1}(\bar{z}) &= c_{z,1}(\bar{z}) = \frac{\bar{\varepsilon}_1(\bar{\varepsilon}_1 - \bar{\varepsilon}_2)}{2(\bar{\varepsilon}_1 + \bar{\varepsilon}_2)}\,\bar{z} \\ c_{\rho,0}(\bar{z}) &= \frac{\bar{\varepsilon}_1^2(\bar{\varepsilon}_1^2 - \bar{\varepsilon}_2^2)\bar{z}^2 + 8\bar{\varepsilon}_1\bar{\varepsilon}_2(\bar{\varepsilon}_1 - \bar{\varepsilon}_2)}{8(\bar{\varepsilon}_1 + \bar{\varepsilon}_2)^2} \\ c_{z,0}(\bar{z}) &= \frac{\bar{\varepsilon}_1^2(\bar{\varepsilon}_1^2 - \bar{\varepsilon}_2^2)\bar{z}^2 + 4\bar{\varepsilon}_1(\bar{\varepsilon}_1 - \bar{\varepsilon}_2)(\bar{\varepsilon}_1 + 3\bar{\varepsilon}_2)}{8(\bar{\varepsilon}_1 + \bar{\varepsilon}_2)^2}\end{aligned} \tag{B-66}$$

It is useful to denote

$$\mathcal{J}_v(n,\bar{z}) = \int_0^\infty \bar{\xi}^n e^{-\bar{\xi}\bar{z}} J_v(\bar{\xi}\bar{\rho}) d\bar{\xi} \tag{B-67}$$

where $v = 0, 1$ and $n = 0, 1, 2$. The closed-form of the above is available in the table of

integral transform as shown below

$$\begin{aligned}
\mathcal{J}_1(2,\bar{z}) &= \frac{3\bar{z}\bar{\rho}}{\bar{r}^5} & \mathcal{J}_0(2,\bar{z}) &= \frac{2\bar{z}^2-\bar{\rho}^2}{\bar{r}^5} \\
\mathcal{J}_1(1,\bar{z}) &= \frac{\bar{\rho}}{\bar{r}^3} & \mathcal{J}_0(1,\bar{z}) &= \frac{\bar{z}}{\bar{r}^3} \\
\mathcal{J}_1(0,\bar{z}) &= \frac{\bar{\rho}}{\bar{r}(\bar{z}+\bar{r})} & \mathcal{J}_0(0,\bar{z}) &= \frac{1}{\bar{r}}.
\end{aligned} \tag{B-68}$$

To ensure the availability of the closed-form for the integration of the asymptotic terms, the previous derivations in (B-62) may be extended to a further step as

$$\begin{aligned}
\tilde{v}^a_{\rho,1}(\bar{\xi}) &= \frac{i}{4\pi\bar{\varepsilon}_1}\left[\pm\bar{\xi}e^{-\bar{\gamma}_1\bar{d}_1} + \left(c_{\rho,2}(\bar{z})\bar{\xi} + c_{\rho,1}(\bar{z}) + c_{\rho,0}(\bar{z})\bar{\xi}^{-1}\right)e^{-\bar{\xi}\bar{d}_2}\right] \\
\tilde{v}^a_{z,1}(\bar{\xi}) &= \frac{i}{4\pi\bar{\varepsilon}_1}\left[\frac{\xi^2}{\bar{\gamma}_1}e^{-\bar{\gamma}_1\bar{d}_1} + \left(c_{z,2}(\bar{z})\bar{\xi} + c_{z,1}(\bar{z}) + c_{z,0}(\bar{z})\bar{\xi}^{-1}\right)e^{-\bar{\xi}\bar{d}_2}\right]
\end{aligned} \tag{B-69}$$

and the residual terms are given as

$$\begin{aligned}
\tilde{v}^r_{\rho,1}(\bar{\xi}) &= \tilde{v}_{\rho,1}(\bar{\xi}) - \tilde{v}^a_{\rho,1}(\bar{\xi}) \\
\tilde{v}^r_{z,1}(\bar{\xi}) &= \tilde{v}_{z,1}(\bar{\xi}) - \tilde{v}^a_{z,1}(\bar{\xi}).
\end{aligned} \tag{B-70}$$

Due to the fast decay of the residual terms when $\bar{\xi} \to \infty$, it allows the fast evaluation of the integral of the residual terms by truncating along the integration path.

With the aid of (B-63), (B-67) and (B-68), the closed-form for the asymptotic terms can be obtained via

$$\begin{aligned}
v^a_{\rho,1}(\bar{\rho},\bar{z}) &= \int_0^\infty \tilde{v}^a_{\rho,1}(\bar{\xi})\bar{\xi}J_1(\bar{\xi}\bar{\rho})d\bar{\xi} \\
&= \frac{i}{4\pi\bar{\varepsilon}_1}\left(\pm\mathcal{J}_1^\gamma(\bar{z}) + \sum_{m=0}^{2} c_{\rho,m}(\bar{z})\mathcal{J}_1(m,\bar{z})\right) \\
v^a_{z,1}(\bar{\rho},\bar{z}) &= \int_0^\infty \tilde{v}^a_{z,1}(\bar{\xi})\bar{\xi}J_0(\bar{\xi}\bar{\rho})d\bar{\xi} \\
&= \frac{i}{4\pi\bar{\varepsilon}_1}\left(\mathcal{J}_0^\gamma(\bar{z}) + \sum_{m=0}^{2} c_{z,m}(\bar{z})\mathcal{J}_0(m,\bar{z})\right)
\end{aligned} \tag{B-71}$$

To this point, the dimensional electric fields in the source layer are obtained via

$$\begin{aligned} E_{\rho,1}(\rho,z) &= \frac{\omega\mu_0 I\Delta l}{k_0}\int_0^\infty \left(\tilde{v}^a_{\rho,1}+\tilde{v}^r_{\rho,1}\right)\bar{\xi}J_1(\bar{\rho})d\bar{\xi} = \frac{\omega\mu_0 I\Delta l}{k_0}\left((v_{\rho,1})^a+(v_{\rho,1})^r\right) \\ E_{z,1}(\rho,z) &= \frac{\omega\mu_0 I\Delta l}{k_0}\int_0^\infty \left(\tilde{v}^a_{z,1}+\tilde{v}^r_{z,1}\right)\bar{\xi}J_0(\bar{\rho})d\bar{\xi} = \frac{\omega\mu_0 I\Delta l}{k_0}\left((v_{z,1})^a+(v_{z,1})^r\right) \end{aligned} \tag{B-72}$$

where the closed-form are available to the asymptotic terms; the residual terms are evaluated in a truncated integration. Upon solving the coefficients in the layers other than the source layer through the recursive propagator matrixes, the dimensional electric fields in the other layer can be readily obtained.

Appendix C
Manual for GPR interpretation

To facilitate the implementation of this method, a graphic user interface is designed for convenient operation, called "GopherGPR" as shown in Fig. C-1.

Step 1: Input the scan number where the program will start to search for a matched scan and click the button "Step 1" to locate the "DZT" files for the metal calibration and the pavement survey.

Upon clicking the button "Step 1", the user is asked to browse for and locate the ".DZT" RADAN files for the metal calibration first, and then for the pavement survey. In this case, the metal calibration file is named "Metal1001.DZT". After selecting the files, the program will search for scans starts from the chosen scan number within the pavement survey "DZT" file. The program will stop searching after it finds the first scan which matches the metal plate calibration in terms of the effective height. The option to search all the scans will be available later. If there are no matched scans in the whole file, the program will be terminated, showing "Height Mismatch" in the text field below.

The value of "effective H" is shown as 25.9 inches, which in return means the nominal height of the GPR box is around 19 inches above the ground. The value of this effective height is associated with the metal calibration file "Metal1001.DZT", which is calculated according to the "Handbook for GPR Inspection of Road Structures" from Geophysical Survey Systems, Inc (GSSI). The value of "applied H" in the popup window is the one used in the model which corresponds to the effective height of the metal calibration scan. Note that the value of the "applied H" may be only applicable to the sample metal calibration provided in this project. For a new metal calibration whose effective height may be different than 25.9 inches, the model will need to be adjusted prior to the interpretation. Furthermore, it should be pointed out that each different calibration height is referred to a differently trained neural networks.

If a matched scan is found, the scans of the metal plate calibration and pavement survey are plotting in the top two windows on the panel, respectively. The program will also plot the metal plate calibration scan (in blue) and the pavement survey scan (in green) together from the effective time-zero in the window called "Pavement & Metal". The subtraction of the metal calibration from the pavement survey is also plotted in the window (in blue) called "Diff=Pavement-Metal", where the user can check whether the unwanted pulse from the feed point is removed. The red line is an illustration from the simulation data, which is also the subtraction of the metal plate simulation from a simulation of a typical pavement profile. A close "fit" or overlap of the red and blue lines indicates that the height of effective time-zero of the survey matches the height of the simulation. Just to the right of this window, a squared window shows the matched reflection pulse of the survey (in blue) and simulation (in red) (similar to Fig. 6.2).

Step 2: Adjust the source pattern of the assumed Mexican-hat pulse (optional).

Two slider bars are designed, One for the time shift, and the other one for the pulse parameter R which controls the width of the pulse. The user may move the slider bars to

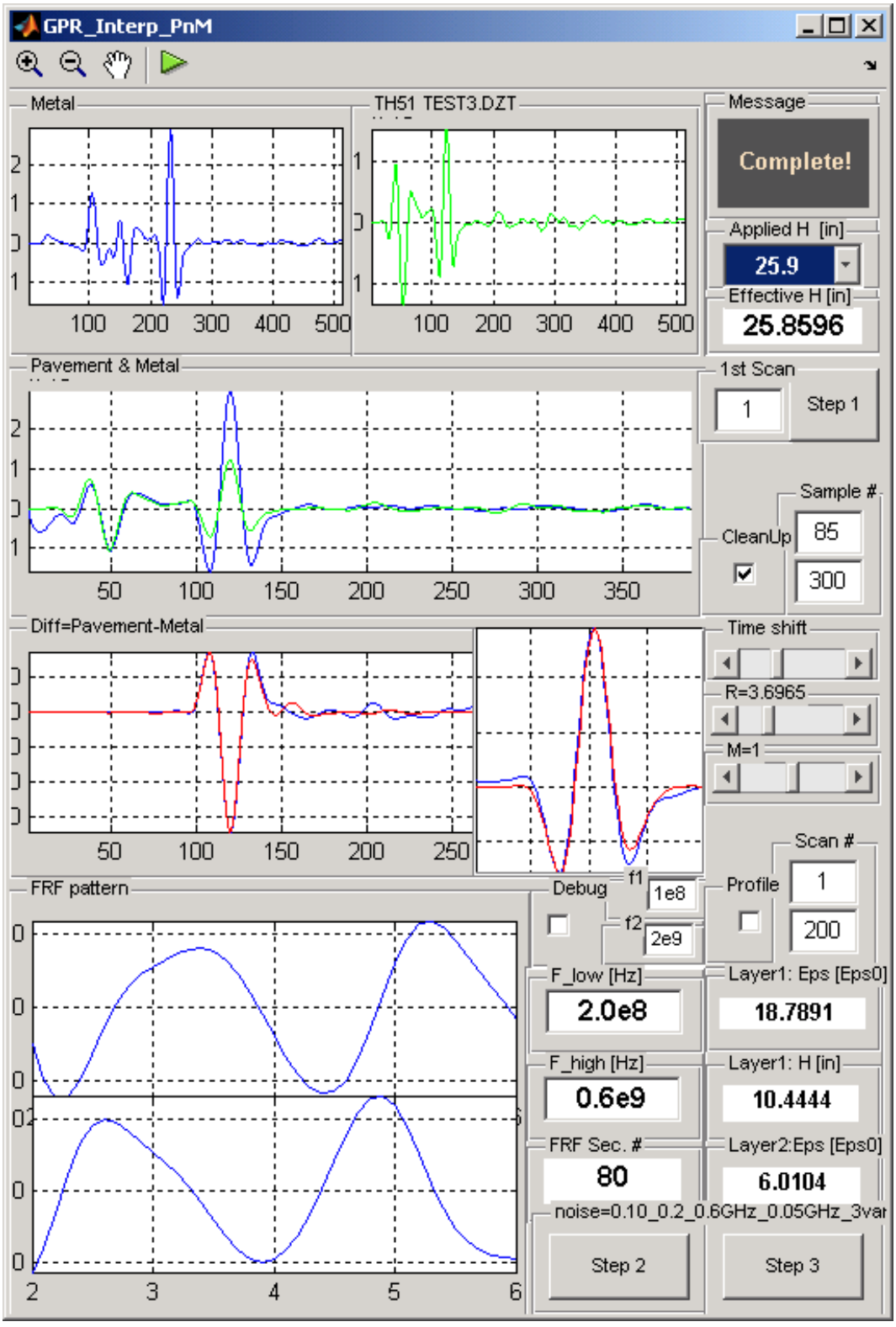

Figure C-1: GopherGPR panel

adjust the pattern of the source. In the end, the reflection of the simulated pulse (in red) should closely overlap with that of the survey pulse (in blue).

In addition, the program provides a cleanup scheme to reduce the extra noise at the beginning and ending of the scan. Under the panel "Sample #", the first sample number is the location before which the amplitudes are set to zero. Moreover, in order to suppress the noise at the end of the scan in certain occasions, the amplitudes after the location of the second sample number will be set to zero as well. Since the capability of the interpretation is limited to the system with asphalt less than 10 inches, the position of the second sample number may be also used to suppress the reflections from additional or deeper interfaces, and the ambient noise as well.

Step 3: Click the button "Step 2" which plots the FRF of the subtraction according to Eq. 6.3 in the window called "FRF pattern".

The upper one is the real portion, and the lower one is the imaginary portion. The range of the FRF (0.95GHz∼1.05GHz) and the number of FRF segments will be displayed in the text fields after clicking the button "Step 2".

Step 4: Click the button "Step 3" to interpret the pavement profile from the computed FRF pattern.

The outputs are shown in the text fields above the button "Step 3". From top to bottom, they are the dielectric constant of the asphalt layer, the thickness of the asphalt layer and the dielectric constant of base layer. If the "Profile" box is checked, the road profile will be obtained between the scan numbers input by user.